

**Surface studies of  
titania related nanostructures**

Anthoula Chrysa Papageorgiou



Thesis for the degree of Doctor of Philosophy  
University College London  
University of London

2007

UMI Number: U592314

All rights reserved

INFORMATION TO ALL USERS

The quality of this reproduction is dependent upon the quality of the copy submitted.

In the unlikely event that the author did not send a complete manuscript and there are missing pages, these will be noted. Also, if material had to be removed, a note will indicate the deletion.



UMI U592314

Published by ProQuest LLC 2013. Copyright in the Dissertation held by the Author.  
Microform Edition © ProQuest LLC.

All rights reserved. This work is protected against  
unauthorized copying under Title 17, United States Code.



ProQuest LLC  
789 East Eisenhower Parkway  
P.O. Box 1346  
Ann Arbor, MI 48106-1346

## **Declaration**

I, Anthoula Chrysa Papageorgiou, confirm that the work presented in this thesis is my own. Where information has been derived from other sources, I confirm that this has been indicated in the thesis.

## Abstract

In this thesis, surface sensitive techniques have been employed to investigate the surface chemistry of  $\text{TiO}_2$ .

A bottom-up approach was used to grow ultra-thin films of rutile  $\text{TiO}_2(110)$  on  $\text{Ni}(110)$ . The surface structure of this system was probed using scanning tunnelling microscopy (STM) and low energy electron diffraction (LEED), whereas the electronic structure was characterised with soft X-ray photoelectron spectroscopy (SXPS). SXPS was also used to investigate the reactivity of this system towards water.

While optimising the conditions for the growth of the desired titania phase, the growth of other structures commonly found in reduced native  $\text{TiO}_2$  crystals were apparent from STM and LEED observations. The formation of  $1\times 2$  reconstructed  $\text{TiO}_2(110)$  and crystallographic shear planes are reported. These phases are assigned by comparison with previous studies of analogous phases on the native rutile  $\text{TiO}_2(110)$  surface.

STM was also used to monitor chemical reactions on native  $\text{TiO}_2(110)$  surfaces. The reaction of surface bridging hydroxyl groups with molecular oxygen at room temperature was imaged directly. After exposure to  $\text{O}_2$ , nearly all bridging hydroxyl groups are consumed, and new, mobile adsorbates appear with a range of apparent heights. With the support of calculations performed by Hofer's group in the University of Liverpool and Fisher's group in UCL, the adsorbates left on the surface after the reaction are assigned to neutral and charged oxygen adatoms as well as terminal hydroxyls.

Finally, the surface local density of states of  $\text{TiO}_2(110)$  were measured using scanning tun-



nelling spectroscopy. Energetically localised states are found at sample biases of +0.2 V, -0.7 V and -1.9 V. Additionally, a surface state at -1.9 V is localised spatially at two adjacent titanium five-fold atoms near to the positions of surface oxygen vacancies.

## Acknowledgements

Firstly, many thanks are due to my supervisor, Prof Geoff Thornton, for giving me the opportunity of these studies and for his inspirational guidance throughout them.

I want also to thank all group members past and present. Particularly, I am indebted to: Dr Qiao Chen for spending so much time and effort in teaching me how to perform and think about surface science experiments; Dr Grégory Cabailh, who guided me in photoelectron spectroscopy experiments and analysis; David Humphrey for providing the best STM tips and working with me in LG38; and Dr Chi Pang, whose continuous scientific and linguistic support made this thesis possible. Your help in the data collection and interpretation presented here is invaluable and I cherish your friendship.

Through the course of my studies I was fortunate with collaborators, towards which I would like to express my sincere thanks. To Prof Gaetano Granozzi, Dr Stefano Agnoli, Dr Francesco Sedona, and the surface science group in the University of Padova, for the opportunity to build experience in characterisation of thin oxide films. To Andrea Resta, Dr Edvin Lundgren, and Prof Jesper Andresen, from University of Lund, for a smooth and pleasant synchrotron run. And to computational chemists: Nikos Beglitis from UCL, for fruitful TiO<sub>2</sub> discussions around coffee and Dr Gilberto Teobaldi from University of Liverpool for his insightful interpretations and clear explanations.

Thanks to my subsidiary supervisor, Dr Wendy Brown, for her encouraging feedback, and Dr Chris Muryn, for his help with the instruments in Manchester Laboratories.

Also, thanks to all the people in both Manchester and London laboratories, and to elec-

tronic & mechanical workshops for making my life easier.

Moreover, many thanks to my family and friends for their invaluable support throughout this process.

Last but not least, acknowledgment should be made to the EU for supplying the financial support through the sixth framework programme.

## List of publications

- A. C. Papageorgiou, C. L. Pang, Q. Chen and G. Thornton  
'Low-dimensional, reduced phases of TiO<sub>2</sub>'  
*ACS Nano* (in press)
- A. C. Papageorgiou, G. Cabailh, Q. Chen, A. Resta, E. Lundgren, J. N. Andersen,  
and G. Thornton  
'Growth and reactivity of titanium oxide ultrathin films on Ni(110)'  
*J. Phys. Chem. C* **111** 7704 (2007).
- C. L. Pang, O. Bikondoa, D. S. Humphrey, A. C. Papageorgiou, G. Cabailh, R. Ith-  
nin, Q. Chen, C. A. Muryn, H. Onishi, and G. Thornton  
'Tailored TiO<sub>2</sub>(110) surfaces and their reactivity'  
*Nanotechnology* **17** 5397 (2006).
- F. Sedona, G. A. Rizzi, S. Agnoli, F. X. Llabrés i Xamena, A. Papageorgiou, D. Os-  
termann, M. Sambì, P. Finetti, K. Schierbaum, and G. Granozzi  
'Ultrathin TiO<sub>x</sub> films on Pt(111): A LEED, XPS, and STM investigation'  
*J. Phys. Chem. B* **109** 24411 (2005).

# Contents

Declaration . . . . .	2
Abstract . . . . .	3
Acknowledgements . . . . .	5
List of publications . . . . .	7
Contents . . . . .	8
List of figures . . . . .	11
<b>1 Introduction</b>	<b>26</b>
References . . . . .	29
<b>2 Theoretical aspects</b>	<b>32</b>
2.1 Scanning tunnelling microscopy (STM) . . . . .	32
2.2 Low energy electron diffraction (LEED) . . . . .	39

2.3	X-ray photoelectron spectroscopy (XPS) . . . . .	40
2.4	Auger electron spectroscopy (AES) . . . . .	43
2.5	X-ray absorption near edge spectroscopy (XANES) . . . . .	44
	References . . . . .	44
<b>3</b>	<b>Instrumentation</b>	<b>47</b>
3.1	The UHV scanning tunnelling microscope systems . . . . .	48
3.1.1	Metal evaporator . . . . .	52
3.1.2	Tip fabrication . . . . .	53
3.2	Low Energy Electron Diffraction (LEED) . . . . .	54
3.3	Auger electron spectroscopy (AES) . . . . .	55
3.4	X-ray photoelectron spectroscopy (XPS) . . . . .	55
3.5	X-ray absorption near edge spectroscopy (XANES) . . . . .	57
	References . . . . .	57
<b>4</b>	<b>Growth and reactivity of titanium oxide ultrathin films on Ni(110)</b>	<b>59</b>
4.1	Introduction . . . . .	60
4.2	Experimental Section . . . . .	62

4.3	Results and Discussion . . . . .	64
4.3.1	The Phases Formed . . . . .	64
4.3.2	XANES . . . . .	70
4.3.3	SXPS . . . . .	71
4.3.4	Reactivity of the TiO <sub>2</sub> (110) Ultrathin Film . . . . .	78
4.4	Conclusions . . . . .	81
	References . . . . .	81
<b>5</b>	<b>Reduced phases of TiO<sub>2</sub>(110) supported on Ni(110)</b>	<b>87</b>
5.1	Introduction . . . . .	87
5.2	Experimental section . . . . .	91
5.3	Results and discussion . . . . .	92
5.3.1	The 1×2 reconstruction . . . . .	92
5.3.2	The crystallographic shear planes . . . . .	94
5.4	Conclusions . . . . .	102
	References . . . . .	102
<b>6</b>	<b>Tracking the reaction of O<sub>2</sub> and surface hydroxyl on TiO<sub>2</sub>(110) with STM</b>	<b>105</b>

6.1	Introduction . . . . .	106
6.2	Experimental section . . . . .	109
6.3	Results and discussion . . . . .	110
6.3.1	Exposure to >90 L O <sub>2</sub> . . . . .	110
6.3.2	Exposure to 0–2 L O <sub>2</sub> . . . . .	115
6.4	Conclusions . . . . .	118
	References . . . . .	118
<b>7</b>	<b>Atomically resolved scanning tunnelling spectroscopy of TiO<sub>2</sub>(110)</b>	<b>122</b>
7.1	Introduction . . . . .	123
7.2	Experimental section . . . . .	126
7.3	Results and discussion . . . . .	128
7.4	Conclusions . . . . .	134
	References . . . . .	135
<b>8</b>	<b>Summary and further work</b>	<b>138</b>



# List of Figures

1.1	Representation of photoexcitation of an electron-hole pair which travel to the surface where they are dexcitated leading to heterogeneous catalysis. . .	28
2.1	(a) Tip model by Tersoff-Haman approximation [3]. (b) Graph showing the calculations of Lang [4] for the change in the apparent height (in Bohr) versus lateral separation (in Bohr) for a tip with a Na atom at the apex scanning over Na, S and He atoms. (1 Bohr = 0.529Å) (c) Illustration of the reciprocity principle by Chen [6]. . . . .	38

2.2	Illustrations of the different processes. (a) XPS: An electron is excited by an incident photon and is given enough energy to overcome its binding energy ( $E_B$ ) and reach the vacuum level (0). (b) AES: The relaxation of an electron from an orbital of higher energy ( $E_{S1}$ ) to an orbital of lower energy ( $E_B$ ) is associated with radiation. This radiation can excite another electron ( $E_{S2}$ ) to overcome its binding energy and reach the vacuum level. (c) XAS: The absorption of a photon to excite a core level electron to a previously unoccupied valance band state. . . . .	41
2.3	Electron attenuation length as a function of energy as determined by experimental results for a range of materials [12]. . . . .	43
3.1	Schematic diagram of the LT-STM (top view; chambers presented in cross-sections). . . . .	49
3.2	Schematic diagram of the VT-STM (top view; chambers presented in cross-sections). . . . .	50
3.3	Schematic diagram of the metal evaporator. . . . .	52
3.4	Schematic illustration of the tip etching. . . . .	53
3.5	(a) Schematic representation of LEED optics. (b) Schematic diagram of the LEED optics working in RFA Auger mode. . . . .	54
3.6	Schematic layout of the I311 beamline at MAX-lab II [3]. . . . .	56

4.1 Models of the surfaces. (a) Model of the  $\text{TiO}_2$  quasi-hexagonal phase grown on  $\text{Ni}(110)$ , as proposed by Atrei *et al.* [2]. The unit cell is indicated. The axes display the orientation of the substrate. (b) Top and side view of a proposed model for the wetting layer phase grown on  $\text{Ni}(110)$ . The unit cell is indicated. The axes display the orientation of the substrate. (c) A model of the rutile  $\text{TiO}_2(110)$  surface as typically prepared in UHV, containing an OH group and an oxygen vacancy. The unit cell and the high symmetry axes of the rutile  $\text{TiO}_2(110)$  surface are displayed. The  $\text{TiO}_2 [1\bar{1}0]$  direction grows parallel to the Ni  $[001]$  direction. . . . . 61

4.2 (a) LEED pattern (128 eV) of the quasi-hexagonal phase (subMLE Ti annealed to 800 K for 30 min in  $10^{-7}$  mbar  $O_2$ ) compared with (b) a schematic representation of the diffraction pattern. (c) LEED pattern of the rutile  $TiO_2(110)$  overlayer (5 MLE Ti oxidised for 1 min in  $10^{-7}$  mbar  $O_2$  and annealed to 800 K) recorded on the beamline end station (123 eV) with (d) the corresponding schematic representation of the diffraction pattern. (e) LEED pattern of the rutile  $TiO_2(110)$  overlayer (2.5 MLE Ti annealed to 800 K for 30 min in  $10^{-7}$  mbar  $O_2$ ) obtained on LT-STM (58 eV) with (f) the corresponding schematic representation of the diffraction pattern. Circles mark the periodicity of Ni(110), crosses mark a  $(2\times 1)$  periodicity of the Ni substrate, ‘-’ mark the quasi-hexagonal structure, squares indicate the periodicity of the wetting layer and ‘^’ spots show its multiple diffraction spots and/or a coincidence cell between the wetting layer and the substrate. The  $TiO_2(110)$  contribution is evident along its [001] azimuth, along which it coincides with the wetting layer. No spots are observed in the  $TiO_2 [1\bar{1}0]$  azimuth due to the small width of the islands in that direction. . . . . 66

4.3	<p>Topographic STM images of the rutile TiO<sub>2</sub> film. The film consists of 2.5 MLE of Ti annealed to 800 K for 30 min in 10<sup>-7</sup> mbar of O<sub>2</sub>. (a) Overview (2000 × 1750 Å<sup>2</sup>; tunnelling conditions: 1.30 V sample bias, 0.10 nA tunnelling current). The symmetry of the Ni(110) substrate is indicated. (b) High resolution image showing a TiO<sub>2</sub>(110) island with the characteristic O vacancies and bridging OH groups. (65 × 65 Å<sup>2</sup>; tunnelling conditions: 1.15 V sample bias, 0.1 nA tunnelling current) (c) STM image of the wetting layer, showing the 40 Å periodicity along the [001] direction of the substrate (185 × 155 Å<sup>2</sup>; tunnelling conditions: 1.00 V sample bias, 1.00 nA tunnelling current) (d) Atomically resolved image of the wetting layer. A (1 × 1) unit cell and a coincidence cell between the wetting layer and the substrate, resulting in a Moiré pattern are indicated. (35 × 60 Å<sup>2</sup>; tunnelling conditions: 0.64 V sample bias, 0.23 nA tunnelling current). Images (a)-(b) recorded at 300 K, images (c)-(d) recorded at 78 K. . . . .</p>	67
4.4	<p>An illustration summarising the TiO<sub>2</sub> phases investigated in this paper, indicating their unit cells and their preparation conditions. . . . .</p>	69
4.5	<p>XANES over the Ti <i>L</i>-edge described in the text of (a) the thin film mainly of quasi-hexagonal phase, consisting of subMLE Ti annealed to 800 K for 30 min in 10<sup>-7</sup> mbar O<sub>2</sub>, and (b) the thin film with rutile phase formed, consisting of 5 MLE Ti oxidised for 1 min in 10<sup>-7</sup> mbar O<sub>2</sub> and annealed to 800 K. The spectra are offset for clarity. . . . .</p>	70

4.6 Left panel: Ni 2p<sub>3/2</sub> XPS spectra ( $h\nu = 1000$  eV) of Ni(110) (a) clean surface, (b) with the rutile film and (c) with the quasi-hexagonal film. Ni 2p<sub>3/2</sub> XPS spectra adapted from Norton *et al.* [37] of Ni(110) (d) clean surface, (e) with a  $\sim 0.44$  ML coverage of chemisorbed oxygen at 295 K and (f) with a  $\sim 1.00$  ML coverage of chemisorbed oxygen at 295 K. The spectra are peak-height normalised and offset for clarity. Top right panel: O 1s XPS spectra ( $h\nu = 650$  eV) (g) of the quasi-hexagonal film and (h) of the rutile film. Circles, dashed lines and solid lines denote the data points, the different components of the fit and the sum of the components respectively. The feature appearing at a shift of 1.13 eV from the bulk oxygen contribution is attributed to OH species. The full width at half maximum (FWHM) of the Gaussian contribution to the components is 1.1 eV and 1.45 eV for the main peak and the OH contribution respectively. All components have a Lorentzian contribution with FWHM of 0.14 eV. The background has been subtracted from the spectra. The spectra are offset for clarity. Bottom right panel: Ti 2p XPS spectra ( $h\nu = 680$  eV) (i) of the quasi-hexagonal film and (j) of the rutile film. The spectra are offset and normalised to the Ti 2p<sub>3/2</sub> for clarity. . . . . 73

4.7	Ti 2p XPS spectra ( $h\nu = 680$ eV). (a) The oxidation of the thin film: The oxygen exposure is noted over each spectrum. (b) The annealing of the thin film: The annealing temperature is noted over each spectrum. The spectra are offset for clarity. At the top, the bars display literature positions for Ti 2p <sub>3/2</sub> core level binding energies for different oxidation states of titanium [5, 39]. . . . .	76
4.8	O 1s core level spectra ( $h\nu = 650$ eV) of the rutile ultrathin film (a) After 160 L exposure of H <sub>2</sub> O recorded at 190 K. (b) After high pressure ( $2 \times 10^{-6}$ mbar) H <sub>2</sub> O exposure recorded at 190 K. Circles, dashed lines and the solid line denote the data points, the different components of the fit and the sum of the components respectively. The background has been subtracted from the spectrum. The contribution of the molecular water on the spectrum is highlighted in grey at a shift of 3 eV from the O 1s bulk contribution. The contribution of hydroxyls is highlighted by diagonal lines at a shift of (a) 1.13 eV, (b) 1.27 eV from the O 1s bulk contribution. The FWHM of the Gaussian contribution to the components is 1 eV for the bulk, (a) 1.54 eV, (b) 1.59 eV for the OH and (a) 1.55 eV, (b) 1.63 eV for the H <sub>2</sub> O contributions. All components have a Lorentzian contribution with FWHM of 0.14 eV. (c) Solid lines correspond to annealing after the high pressure H <sub>2</sub> O exposure. The respective annealing temperatures are noted on their right. The red-dots corresponds to the rutile film before exposure to H <sub>2</sub> O; it is displayed for comparison alongside the spectrum of the film annealed to 490 K. . . . .	80

- 5.1 Atomic models of  $\text{TiO}_2(110)$  surfaces. The high symmetry axes and the surface unit cells are indicated. Small blue spheres represent Ti atoms and larger red spheres O atoms. O atoms nearer to the surface are shaded lighter. (a) The unreconstructed  $\text{TiO}_2(110)$   $1\times 1$  surface. (b) The proposed added  $\text{Ti}_2\text{O}_3$ -row model for the  $\text{TiO}_2(110)$   $1\times 2$  reconstruction [5]. . . . . 88
- 5.2 Schematic representation of crystallographic shear planes intersecting the  $\text{TiO}_2(110)$  surface. Blue circles represent Ti atoms and rhombi are the cross sections of Ti atoms in pseudo-octahedral co-ordination. Cross sections represent a cut parallel to the (001) plane. CS planes of (132) orientation are indicated by dotted lines intersecting the (001) plane along the  $[310]$  direction and by solid lines intersecting the (110) plane along the  $[\bar{1}\bar{1}1]$  direction. One of these CS planes is highlighted with a red dashed perimeter. The rhombi which form the CS planes are shaded gray. The CS planes induce half-height steps at the  $\text{TiO}_2(110)$  surface resulting in (a) an “up-down” half-height step arrangement and (b) a “staircase” half-height step arrangement. The periodicity between the up-down pairs,  $d$ , is indicated. 90
- 5.3 STM images of  $\text{TiO}_2$  islands with a  $1\times 2$  termination. (a) Large scale ( $350\times 470 \text{ \AA}^2$ , 1.05 V, 3.44 nA) image. The axes mark the orientation of  $\text{TiO}_2(110)$ . (b) High resolution smoothed image ( $90\times 90 \text{ \AA}^2$ , 1.00 V, 1.00 nA). A single link (i), a cross-link (ii), and a rosette-link (iii) are indicated. (c) Line profile along the line drawn in (b). . . . . 93



- 5.4 (a) LEED pattern (32 eV; negative image) of the crystallographically sheared film. The orientation of  $\text{TiO}_2(110)$  is indicated. (b) Schematic diagram of (a) drawn to scale. Filled red circles depict the spots present in the LEED pattern. Open circles show the positions of the LEED beams from the  $\text{TiO}_2(110)$   $1 \times 1$  termination. The zero order spot is labelled. The lines indicate the principal directions of the streaking in the LEED pattern with respect to the  $\text{TiO}_2(110)$  surface unit cell. . . . . 95
- 5.5 STM images of the crystallographically sheared film. (a) ( $1700 \times 2100 \text{ \AA}^2$ , 0.30 V, 0.90 nA). (b) ( $1500 \times 1800 \text{ \AA}^2$ , 0.15 V, 0.80 nA). The arrows indicate both the principal azimuths of the  $\text{TiO}_2(110)$  surface and the directions of the CS plane intersections at the (110) surface. (c) Line profile along the line indicated in (a). (d) Line profile along the line indicated in (b). The image in (b) has a shadow effect applied and the line profile in (d) is taken from an image without the shadow applied. . . . . 97
- 5.6 (a) Differentiated STM image of the crystallographically sheared film. ( $3600 \times 3600 \text{ \AA}^2$ , 0.50 V, 4.82 nA). The arrows indicate the principal azimuths of the  $\text{TiO}_2(110)$  surface. Parts of four facets are highlighted by different colours. (b) Schematic representation of the facet arrangement in the lower part of the STM image, with the same colour coding as (a).  $F_1$ ,  $F_2$ ,  $F_3$  and  $F_4$  correspond to the  $(16 \ 17 \ \bar{1})$ ,  $(16 \ 17 \ 1)$ ,  $(17 \ 16 \ 1)$  and  $(17 \ 16 \ \bar{1})$  planes respectively. The arrows indicate intersections of the facets with each other and with the (110) plane. . . . . 98

5.7 (a) STM image of the crystallographically sheared film. ( $360 \times 180 \text{ \AA}^2$ , 0.15 V, 0.85 nA). The arrows indicate both the principal azimuths of the  $\text{TiO}_2(110)$  surface and the direction of the CS plane intersections. A dashed guideline shows that the  $\text{TiO}_2(110)$   $1 \times 1$  rows are in-phase across the half steps. Note that the image in this figure is taken from one of the minority islands with the  $\text{TiO}_2$  [001] azimuth oriented parallel to the Ni [001] direction. Similar images were observed on the majority islands where the  $\text{TiO}_2$  [ $1\bar{1}0$ ] azimuth lies parallel to Ni [001]. (b) Fast Fourier transform of the STM image presented in (a). Blue arrows pointing to the right indicate discrete spots arising due to the periodicity of the CS plane up-down pairs and red arrows pointing to the left indicate the (01) and ( $0\bar{1}$ ) spots of  $\text{TiO}_2(110)$ . An open yellow circle highlights the (00) spot. (c)-(d) Line profiles along the lines indicated in (a). . . . . 101

6.1 STM images (tunnelling voltage: 1.50 V; tunnelling current: 0.50 nA) of  $\text{TiO}_2(110)$ . (a) ( $400 \times 400 \text{ \AA}^2$ , inset  $50 \times 42 \text{ \AA}^2$ ) After dosing 30 L of  $\text{H}_2\text{O}$  which resulted in 11% ML  $\text{OH}_{\text{br}}$  as indicated in the inset. The blue square highlights an area scanned at 3 V to create a  $\text{OH}_{\text{br}}$ -free area. (b) ( $400 \times 400 \text{ \AA}^2$ , inset  $50 \times 42 \text{ \AA}^2$ ) and (c) ( $187 \times 187 \text{ \AA}^2$ ) the same area after exposure to 90 L of  $\text{O}_2$ , containing a new type of adsorbate as indicated in the inset of (b). The blue square marks the previously  $\text{OH}_{\text{br}}$ -free area in (b) and part of the blue square is marked in (c). . . . . 110

6.2	(a)-(c) Sequential STM images ( $120 \times 200 \text{ \AA}^2$ ; tunnelling voltage: 1.50 V; tunnelling current: 0.20 nA) of the hydroxylated $\text{TiO}_2(110)$ surface after dosing 90 L of $\text{O}_2$ . The images were recorded less than 1 min apart. The blue ellipses are drawn over the same area in each image to guide the eye. In each image, the number and the positions of the type C adsorbates clearly change dramatically within these ellipses. . . . .	112
6.3	STM topography images ( $260 \times 246 \text{ \AA}^2$ ; tunnelling voltage: 1.50 V; tunnelling current: 0.20 nA) of (a) a $\text{TiO}_2(110)$ surface containing $\text{O}_{\text{vac}}$ and $\text{OH}_{\text{br}}$ which formed from dissociation of $\text{H}_2\text{O}$ from the UHV residual gases and (b) the same area after exposure to 90 L of $\text{O}_2$ , containing mainly type C adsorbates as indicated. . . . .	113
6.4	(a) The apparent heights of type C and type $\text{C}_1$ adsorbates indicated in figure 6.3. (b) Simulated scanlines for $\text{O}_{(\text{ad})}^0$ , $\text{O}_{(\text{ad})}^-$ and $\text{O}_{(\text{ad})}^{2-}$ [25]. . . . .	115
6.5	STM images ( $176 \times 260 \text{ \AA}^2$ ; tunnelling voltage: 1.50 V; tunnelling current: 0.34–0.19 nA) of (a) a $\text{TiO}_2(110)$ surface after dosing 30 L of $\text{H}_2\text{O}$ and therefore containing $\text{OH}_{\text{br}}$ and (b) the same area as (a) after exposure to 0.5 L of $\text{O}_2$ . This surface contains adsorbates atop $\text{Ti}_{5\text{c}}$ with three different apparent heights, as indicated by circles. (c) The apparent heights of the three new features atop $\text{Ti}_{5\text{c}}$ resulting from the exposure to $\text{O}_2$ , as indicated in (b). (d) The coverage of these features as a function of $\text{O}_2$ exposure. The lines corresponding to the different types of adsorbates have the same colour coding in (b)–(d). . . . .	116

6.6	(a) The apparent heights of the three new features atop $\text{Ti}_{5c}$ resulting from the exposure to $\text{O}_2$ . (b) Simulated scanlines for $\text{O}_{(\text{ad})}^0$ , $\text{O}_{(\text{ad})}^-$ , $\text{O}_{(\text{ad})}^{2-}$ , $\text{OH}_t^0$ and $\text{OH}_t^-$ [25]. . . . .	117
7.1	Calculated density of states for the surface containing two adjacent $\text{OH}_{\text{br}}$ (top spectrum) and the surface containing an $\text{O}_{\text{vac}}$ (bottom spectrum). The states localised in the titanium atom under the vacancy (d) and hydroxyl pair (a) are highlighted in blue, whereas the states localised in a $\text{Ti}_{5c}$ titanium, first nearest $\text{Ti}_{5c}$ neighbour to the vacancy (c) and hydroxyl pair (b), are highlighted in red. (Figure reproduced from Di Valentin <i>et al.</i> [8]) . . .	125
7.2	(a) Ball model of the rutile $\text{TiO}_2(110)$ surface, containing a hydroxyl group and an oxygen vacancy, as expected from typical UHV preparation. The unit cell and the high symmetry axes are displayed. Typical STM topographic images of $\text{TiO}_2(110)$ . (b) Image recorded at 4.5 K ( $72 \times 59 \text{ \AA}^2$ ; 2.30 V tunnelling voltage; 0.05 nA tunnelling current) showing $\text{O}_{\text{vac}}$ and $\text{OH}_{\text{br}}$ as lower and higher defects between the bright $\text{Ti}_{5c}$ rows, respectively. (c) Image taken at 78.0 K ( $72 \times 59 \text{ \AA}^2$ ; 1.26 V tunnelling voltage; 0.02 nA tunnelling current). In (c) streaking is present along the fast scan direction over the $\text{Ti}_{5c}$ rows after a few hours. . . . .	126

- 7.3 (a) STM image recorded at 4.5 K ( $250 \times 250 \text{ \AA}^2$ ; 2.30 V tunnelling voltage; 0.05 nA tunnelling current) showing an overview of the surface topography before the collection of STS. A black square indicates the area from which the image is taken in (b). The vectors indicate the high symmetry axes. (b) Smoothed topographic STM image taken at 4.5 K ( $45 \times 45 \text{ \AA}^2$ ; 2.00 V tunnelling voltage; 0.03 nA tunnelling current) recorded simultaneously with the STS data. . . . . 129
- 7.4 Current maps at sample bias ranging from +2.00 to -2.00 V, recorded simultaneously with the topographic image displayed in figure 7.3b. The absolute value of current is plotted in grayscale with higher current corresponding to brighter areas. A light blue grid is superimposed on the current maps corresponding to +2.0, +1.6, +1.4, -0.1 and -1.9 V. The grid indicates  $\text{Ti}_{5c}$  rows. The positions of  $\text{O}_{vac}$ ,  $\text{OH}_{br}$  and  $\text{H}_2\text{O}$  are highlighted with orange, purple and blue crosses, respectively. Two sites with increased conductivity over  $\text{Ti}_{5c}$  atoms,  $\text{Ti}_{5c}(1)$ , are circled in green. . . . . 131

- 7.5 (a) Current map at 4.5 K with sample bias  $-2.00$  V. The intersections in the superimposed light blue grid correspond to the  $\text{Ti}_{5c}$  positions. Positions of  $\text{O}_{\text{vac}}$ ,  $\text{OH}_{\text{br}}$  and  $\text{H}_2\text{O}$  are highlighted with orange, purple and blue crosses, respectively. (b) The table shows the probability (as a percentage) of finding special, bright  $\text{Ti}_{5c}(1)$  sites in positions relative to the oxygen vacancy, which is indicated with an orange cross.  $8 \times 6$  unit cells centred around each  $\text{O}_{\text{vac}}$  were used to construct this table. Because the  $\text{TiO}_2(110)$  surface has 4-fold symmetry, the probabilities are only shown for one quadrant (i.e.  $4 \times 3$  unit cells) which is obtained by averaging the probabilities found for each quadrant. . . . . 132
- 7.6 (a) The differential conductivities versus the sample bias. Different curves correspond to spectra averaged over  $\text{O}_{\text{br}}$ ,  $\text{O}_{\text{vac}}$ ,  $\text{Ti}_{5c}$  and  $\text{OH}_{\text{br}}$  sites. The inset shows the corresponding STM topography and indicates the areas from which the averaged spectra are taken. (b) Local density of states corresponding to the same areas as in (a) versus sample bias. Dotted lines mark the position of the conduction band minimum. . . . . 133

# Chapter 1

## Introduction

The physics and chemistry of surfaces has long been regarded as a subject of great importance. For instance, it is thought that if the pathways of surface reactions can be unravelled it will be possible to control and tailor catalysts. Hence, the surfaces on which catalytic reactions take place have been studied extensively in Surface Science. As many heterogeneous catalysts consist of a transition metal dispersed on an oxide support, single crystal metal surfaces have been used as ‘model catalysts’ in many of these studies [1]. However, as the evidence that the oxide support is more than a ‘spectator’ increases, so does the need to include an oxide support in model catalysts [2]. The study of oxide surfaces is difficult because they are often insulating materials, and therefore unsuitable substrates for the majority of surface science characterisation techniques.

For titanium dioxide, two main approaches can be used to circumvent this conductivity problem. The first approach is to reduce the native crystal so that enough carriers are created to make the sample conduct [3]. The second approach is to grow ordered oxide

## Chapter 1

films on metallic substrates, with a thickness low enough to conduct [4].

Apart from their use as mimics for native surfaces, ultrathin films have also attracted wide interest because of the novel properties that their reduced dimensionality can confer. For example, electronic [5], magnetic [6] and catalytic [7] properties with no bulk counterpart have been reported. In recent years, the scientific community has invested considerable research effort in the domain of nanoscale structures which will be crucial in the further miniaturisation of electronics. Therefore, the literature is currently rich in investigations of nanostructures, particularly those grown by self-assembly where the production is not labour intensive.

Research into surfaces and nanostructures has been revolutionised by scanning probe microscopes and their ability to provide real space images with atomic resolution. These techniques are also increasingly employed as tools for the manipulation of atoms [8] and molecules [9], thus providing a novel approach in building structures or devices [10]. Current research efforts also seek to add forms of chemical specificity to the spatial resolution of scanning probe microscopes [11, 12].

Titanium dioxide is used as a substrate throughout this thesis. It is a versatile material which is exploited in a wide range of technological applications. The use of  $\text{TiO}_2$  in many of these applications, such as solar cells and self-cleaning windows, rely on its photocatalytic properties [13]. This is based on the creation of surface electron-hole pairs upon UV irradiation (figure 1.1). Recent experiments show that  $\text{TiO}_2$  converts formamide to nucleoside bases upon UV light irradiation  $< 4$  eV [14], leading to speculation that  $\text{TiO}_2$  may have played a role in the origin of life on earth.



## Chapter 1

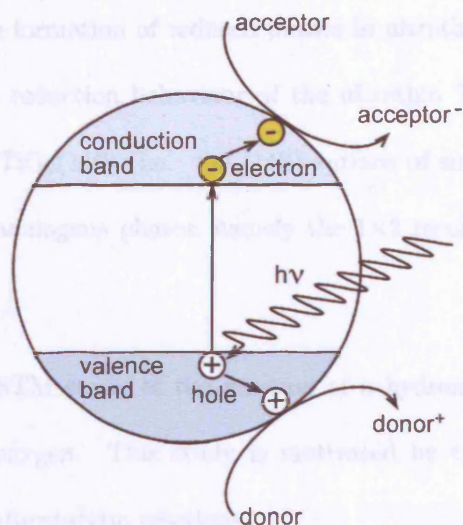


Figure 1.1: Representation of photoexcitation of an electron-hole pair which travel to the surface where they are recombined leading to heterogeneous catalysis.

In the remainder of this thesis, chapter 2 outlines the operation principles of the experimental techniques employed. These span the range of scanning tunnelling microscopy (STM), low energy electron diffraction (LEED), X-ray photoelectron spectroscopy (XPS), Auger electron spectroscopy (AES) and X-ray absorption near edge structure (XANES).

Chapter 3 describes the instrumentation required to implement these techniques in ultra-high vacuum (UHV). The three different UHV systems and their peripherals are described together with a short section concerning the use of synchrotron radiation light. The potential and limitations of the experimental techniques are also highlighted, where appropriate.

In chapter 4 there is a detailed description of fully oxidised phases of titanium grown on Ni(110). STM, LEED, XANES and XPS are used in combination, providing both structural and electronic characterisation of these phases. On this basis, models are proposed for these surface structures.

## Chapter 1

Chapter 5 reports on the formation of reduced phases in ultrathin titanium dioxide supported on Ni(110). The reduction behaviour of the ultrathin TiO<sub>2</sub> is shown to closely resemble that of native TiO<sub>2</sub>(110) (i.e. the (110) surface of single crystal rutile TiO<sub>2</sub>) with the observation of analogous phases, namely the 1×2 reconstruction and crystallographic shear planes.

Chapter 6 describes an STM study of the reaction of a hydroxylated native TiO<sub>2</sub>(110) surface with molecular oxygen. This study is motivated by the role of oxygen as an electron scavenger in photocatalytic reactions.

Closing the results section, chapter 7 reveals the surface density of states obtained by scanning tunnelling spectroscopy (STS). Energetically and spatially localised surface states are reported.

Finally, the results of this project are summarised in chapter 8 and placed in a wider perspective. Some suggestions for further research are also discussed.

# References

- [1] G. A. Somorjai, *Introduction to surface chemistry and catalysis* John Wiley & Sons, New York (1994).
- [2] V. E. Henrich and P. A. Cox, *The surface science of metal oxides* Cambridge University Press, Cambridge (1996).
- [3] G. S. Rohrer, V. E. Henrich, and D. A. Bonnell, *Science* **250**, 1239 (1990).
- [4] H.-J. Freund, *Angew. Chem.* **109**, 444 (1997).
- [5] K. Eberl, *Phys. World* **10**, 45 (1997).
- [6] K. Wildberger, V. S. Stepanyuk, P. Lang, R. Zeller, and P. H. Deherichs, *Phys. Rev. Lett.* **75**, 509 (1995).
- [7] M. Harute, *Catal. Today* **36**, 153 (1997).
- [8] D. M. Eigler and E. K. Schweizer, *Nature* **344**, 524 (1990).
- [9] S.-W. Hla, L. Bartels, G. Meyer, and K.-H. Rieder, *Phys. Rev. Lett.* **85**, 2777 (2000).
- [10] A. J. Heinrich, C. P. Lutz, J. A. Gupta, and D. M. Eigler, *Science* **298**, 1381 (2002).

- [11] Y. Sugimoto, P. Pou, M. Abe, P. Jelinek, R. Pérez, S. Morita, and Ó. Custance, *Nature* **446**, 64 (2007).
- [12] B. C. Stipe, M. A. Rezaei, and W. Ho, *Science* **280**, 1732 (1998).
- [13] A. L. Linsebigler, G. Lu, and J. T. Yates, Jr., *Chem. Rev.* **95**, 735 (1995).
- [14] S. D. Senanayake, and H. Idriss, *Proc. Natl. Acad. Sci. U.S.A.* **103**, 1194 (2006).

## Chapter 2

# Theoretical aspects

This chapter gives an account of the principles behind the characterisation techniques employed. These techniques include mainly scanning tunnelling microscopy (STM), low energy electron diffraction (LEED), Auger electron spectroscopy (AES), X-ray photoelectron spectroscopy (XPS) and X-ray absorption near edge spectroscopy (XANES). The potential and limitations of these methods are also discussed.

### 2.1 Scanning tunnelling microscopy (STM)

The invention of STM was a Nobel prize winning innovation in the early 1980s by Binnig and Rohrer [1]. Since then it has become a major tool in surface science, enabling measurement and manipulation of surfaces down to the atomic level.

STM is based on the phenomenon of quantum mechanical tunnelling. An atomically sharp, conducting tip is used to probe the surface of a sample. This is achieved by

applying a bias between the tip and sample, then placing the two in such proximity that quantum tunnelling of electrons between the tip and the surface is possible. In other words, their wavefunctions overlap, resulting in a flow of electrons. The tip is then scanned across the surface by a piezoelectric drive and can operate in two modes: constant current and constant height. In the constant current mode, the height of the tip is adjusted continuously so that the tunnelling current remains constant. A topographic image is formed by recording the movement of the tip. In the constant height mode, the height of the tip above the surface is constant and variations of the tunnelling current are recorded.

To illustrate the principle behind the STM let us consider the example of an electron of energy  $E$ , and mass  $m$ , tunnelling through a one dimensional potential barrier  $V_0$ , with width  $s$ . In quantum mechanics a particle is described by its wavefunction. The time independent Schrödinger equation (TISE) of the electron can be written as:

$$-\frac{\hbar^2}{2m} \frac{d^2\psi}{dx^2} + V\psi = E\psi , \quad (2.1)$$

where  $\hbar$  is Planck's constant divided by  $2\pi$ ,  $\psi$  is the wavefunction of the electron,  $x$  its position and  $V$  its potential. In this case  $V = V_0$  for  $0 \leq x \leq s$  and  $V = 0$  for  $x \leq 0$  and  $x \geq s$ .

The general solution of the TISE is given by:

$$\psi = \begin{cases} A_1 e^{ikx} + A_2 e^{-ikx} & \text{for } x \leq 0 \\ B_1 e^{\kappa x} + B_2 e^{-\kappa x} & \text{for } 0 \leq x \leq s \\ C_1 e^{ikx} + C_2 e^{-ikx} & \text{for } x \geq s, \end{cases} \quad (2.2)$$

where  $A_1$ ,  $A_2$ ,  $B_1$ ,  $B_2$ ,  $C_1$  and  $C_2$  are constants,  $k = \sqrt{\frac{2mE}{\hbar^2}}$  and  $\kappa = \sqrt{\frac{2m(V_0 - E)}{\hbar^2}}$ . Note that  $C_2$  goes to zero, since after the potential barrier only waves propagating out of it can exist. Given the boundary conditions for the continuity of the wavefunction, one can derive an expression for the transmission coefficient:

$$T = \left( 1 + \frac{(k^2 + \kappa^2)}{4k^2\kappa^2 \sinh^2(\kappa s)} \right)^{-1}. \quad (2.3)$$

In the limit of a large attenuating barrier, this can be approximated with:

$$T \approx \frac{16k^2\kappa^2}{(k^2 + \kappa^2)} e^{-2\kappa s}. \quad (2.4)$$

Hence, we can see that in the case of tunnelling, the transmission coefficient is exponentially dependent on the width  $s$  of the potential barrier. This exponential dependence is responsible for the high spatial resolution of STM.

In the same limit, for the time dependent treatment, Bardeen [2] used a perturbation approach, introducing the following approximate solutions of the exact Hamiltonian,  $\hat{H}$ :

$$\begin{cases} \psi_1 = ae^{-\kappa x} & \text{for } x \geq 0 \\ \psi_2 = be^{\kappa x} & \text{for } x \leq s , \end{cases} \quad (2.5)$$

where  $\psi_1$  has to be matched to the correct solution of the Schrödinger equation for  $x \geq 0$  and decay for  $x \leq s$ , and vice versa for  $\psi_2$ . Therefore, the transition rate of state  $\psi_1$  to state  $\psi_2$  can be computed. The time dependent Schrödinger equation (TDSE) gives:

$$\hat{H}\psi(t) = i\hbar \frac{d\psi(t)}{dt} , \quad (2.6)$$

with:

$$\hat{H} = (\hat{H}_1 + \hat{H}_2) + \hat{H}_T , \quad (2.7)$$

where  $\hat{H}$  is the total Hamiltonian,  $\hat{H}_1$  the Hamiltonian for  $x \leq 0$ ,  $\hat{H}_2$  the Hamiltonian for  $x \geq s$  and  $\hat{H}_T$  the transfer Hamiltonian that describes the electron tunnelling through the barrier. By substituting:

$$\psi(t) = c(t) \psi_1 \exp\left(-\frac{iE_1 t}{\hbar}\right) + d(t) \psi_2 \exp\left(-\frac{iE_2 t}{\hbar}\right) \quad (2.8)$$

into equation 2.6, the effective tunnelling matrix element,  $M_{12}$ , becomes apparent:

$$M_{12} = \int \psi_2^* (\hat{H} - E_1) \psi_1 = \int \psi_2^* \hat{H}_T \psi_1 . \quad (2.9)$$



In the limit of a strong attenuation barrier, Fermi's "golden rule" of first order time dependent perturbation theory estimates the transmitted current as:

$$j_T = \frac{2\pi}{\hbar} |M_{12}|^2 \frac{dN}{dE_2} , \quad (2.10)$$

where  $N$  is the number of electrons with energy  $E_2$ . Hence, the last term is the density of states (DOS) in the final state. In this case, the time independent method gives the same result as the time dependent method but the latter is more generic and is not restricted to one dimension.

Within this formalism, given constant current, the tunnelling current between a tip and a surface separated by a barrier of vacuum is given by:

$$I = \frac{2\pi e}{\hbar} \sum_{\mu,\nu} \{f(E_\mu)[1 - f(E_\nu - eU)] - f(E_\nu - eU)[1 - f(E_\mu)]\} \cdot |M_{\mu\nu}| \delta(E_\nu - E_\mu) , \quad (2.11)$$

where  $f(E)$  is the Fermi distribution,  $U$  is the applied sample bias,  $M_{\mu\nu}$  is the tunnelling matrix element between the states  $\psi_\mu$  of the tip and the states  $\psi_\nu$  of the surface and  $E_\mu$  and  $E_\nu$  are the eigenvalues of  $\psi_\mu$  and  $\psi_\nu$ , respectively. The delta function gives the conservation of energy in elastic tunnelling. The problem is then reduced to evaluating the matrix element, which according to [2] is given by:

$$M_{\mu\nu} = \frac{-\hbar^2}{2m} \int (\psi_\mu^* \nabla \psi_\nu - \psi_\nu \nabla \psi_\mu^*) \cdot d\mathbf{S} , \quad (2.12)$$

where  $\mathbf{S}$  is the surface of the area lying in vacuum. For small voltage and low temperature,

equation 2.11 can be approximated with:

$$I = \frac{2\pi e^2}{\hbar} U \sum_{\mu,\nu} |M_{\mu\nu}|^2 \delta(E_\nu - E_F) \cdot \delta(E_\mu - E_F) . \quad (2.13)$$

Tersoff and Hamann [3] approximated the tip with a locally spherical potential well and evaluated the matrix element for an s-type tip wavefunction, as illustrated schematically in figure 2.1a. Hence the tunnelling current can be expressed as:

$$I \propto U n_t(E_F) \cdot e^{2\kappa' R} \cdot \sum_{\nu} |\psi_{\nu}(\mathbf{r}_0)|^2 \delta(E_\nu - E_F) , \quad (2.14)$$

where  $\kappa' = \frac{2m\phi}{\hbar}$ ,  $\phi$  is the effective local potential barrier height,  $n_t(E_F)$  the DOS of the tip at the Fermi level,  $R$  the effective tip radius and  $\mathbf{r}_0$  the centre of curvature of the tip. The sum in equation (2.14) can be identified as the surface local DOS at the Fermi level at the centre of curvature of the effective tip. Therefore, in the Tersoff-Hamann approximation, the STM images are interpreted as contour maps of constant surface local DOS at  $E_F$ ,  $r_0$ . It should be noted that the wavefunctions decay exponentially with tip-surface separation  $s$ , as does the tunnelling current  $I$ .

Lang [4] used *ab initio* calculations within the above formalism to demonstrate that STM indeed images the local DOS at  $E_F$  and does not correspond to the true topography of the surface. A Na atom was scanned over a He atom at constant current, as shown in figure 2.1b. This resulted in the observation of a depression, which indicates that a negative tip displacement is required in order to keep the current constant, whereas the He atom clearly has a positive height in the true topography.

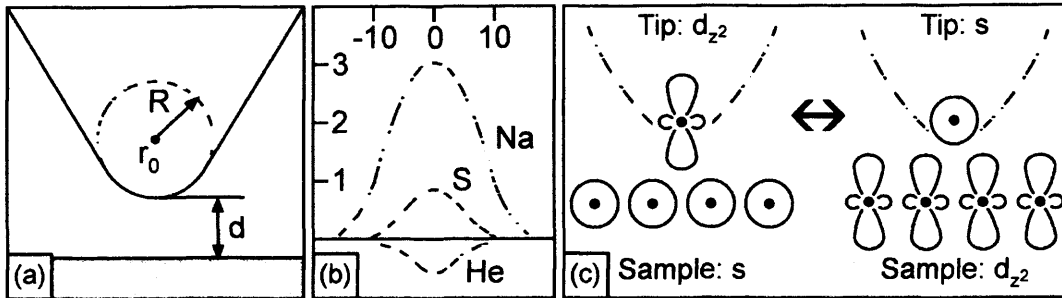


Figure 2.1: (a) Tip model by Tersoff-Haman approximation [3]. (b) Graph showing the calculations of Lang [4] for the change in the apparent height (in Bohr) versus lateral separation (in Bohr) for a tip with a Na atom at the apex scanning over Na, S and He atoms. (1 Bohr = 0.529Å) (c) Illustration of the reciprocity principle by Chen [6].

The evaluated spatial resolution limit of STM [3–5], based on the approximations above, is inconsistent with the experimental evidence which shows that STM can give atomically resolved images. By introducing the reciprocity principle, illustrated schematically in figure 2.1c, Chen [6] showed that this discrepancy arises from the assumption of an s-wave tip. The reciprocity principle states that if the tip and sample states were interchanged, the resulting STM image would remain the same. Considering that commonly used tip materials have d band electrons, he simulated atomically resolved corrugation by scanning an s-wave tip over a  $d_{z^2}$ -wave surface. This result accounts for the atomic resolution observed in experimental images. Chen also noted the importance of knowing the nature of the tip apex atom, when estimating the maximum corrugation of an STM image.

Drakova [7] reviews theoretical approaches to describing the STM. Three-dimensional scattering theory of STM and STS can be used to avoid the transfer-Hamiltonian approach, which requires a strong attenuation barrier. It allows the evaluation of the exact tunnelling current for a given model of tip and sample. The most recent approach is the dynamic theory. It explains atomic resolution of STM as the corrugation of the charge density in an

electronically excited system, which results from the tunnelling process, i.e. the injection of additional tunnelling charges in a localised region of the sample surface. It should be noted though, that the corrugation of STM images is still not fully elucidated.

The case of STM of oxide surfaces is considered in a review by Bonnell [8]. Oxides are usually materials exhibiting a band gap within which the Fermi level is located. An additional consideration should be made, since the bias between the tip and the surface is dropped across the sample in a space charge region directly below the tip. This region can be evaluated at 0 V bias to be given by:

$$d = \sqrt{\frac{2\epsilon kT}{q^2 N}} , \quad (2.15)$$

where  $q$  is the charge of an electron,  $\epsilon$  is the sample permittivity,  $N$  is the density of charge carriers,  $k$  is the Boltzmann constant and  $T$  is the temperature. Hence the spatial resolution might be limited due to the radius of the space charge region.

## 2.2 Low energy electron diffraction (LEED)

In 1927, Davisson and Germer showed that for a beam of monoenergetic electrons, which is directed at a single crystal, the elastically scattered electrons emerge in preferred directions. The directions could be explained by the crystal lattice providing a periodic grid for diffraction. This phenomenon forms the basis of LEED.

An excellent overview of the technique can be found in [9]. Essentially, the diffraction

pattern observed is the projection of the examined surface in reciprocal space, whose magnification depends upon the energy of the incident electron beam. Although both the positions and the intensity of the diffracted spots are physically meaningful, in the studies described here only the spot positions are considered.

The technique has high surface sensitivity (it samples only the first atomic layers, about 10 Å) and can provide information about the surface structure.

### 2.3 X-ray photoelectron spectroscopy (XPS)

XPS is based on the photoelectric effect. A sample is irradiated by monochromatic photons, which provide energy towards the excitation of electrons from the occupied states into the vacuum, where they are detected by an electron energy analyser. These emitted electrons possess kinetic energy  $E_K$  which is related to the binding energy of the electron ( $E_b$ ) as follows:

$$E_K = h\nu - E_b , \quad (2.16)$$

where  $h\nu$  is the energy of the incident photon. This process is illustrated in figure 2.2a. The binding energy ( $E_b$ ) of photoemitted electrons is characteristic of the examined atomic species and its chemical state.

In this thesis, core levels of titanium oxide and nickel have been probed by means of soft XPS (SXPS). “Soft” X-rays indicate an energy range of the incident light beam between

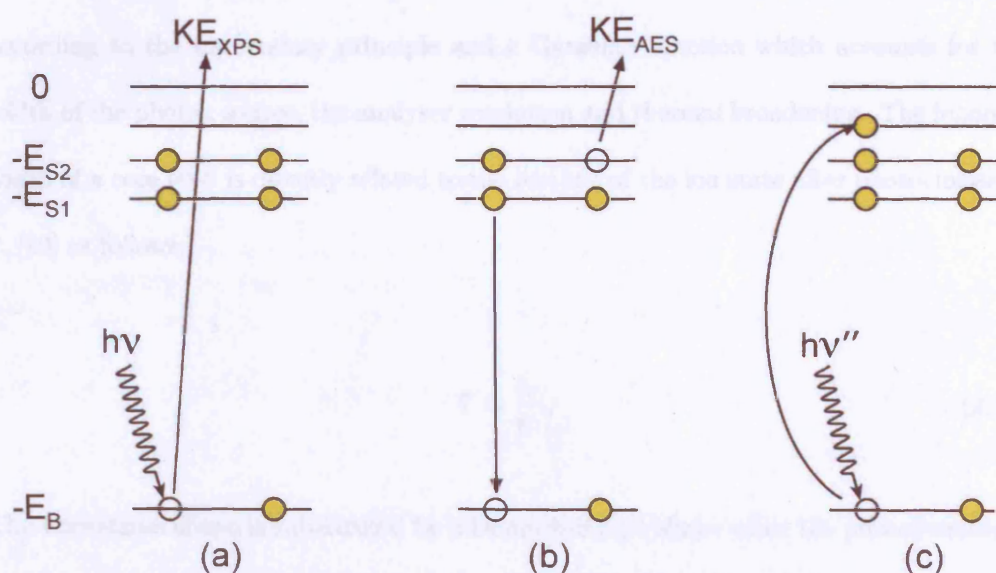


Figure 2.2: Illustrations of the different processes. (a) XPS: An electron is excited by an incident photon and is given enough energy to overcome its binding energy ( $E_B$ ) and reach the vacuum level (0). (b) AES: The relaxation of an electron from an orbital of higher energy ( $E_{S1}$ ) to an orbital of lower energy ( $E_B$ ) is associated with radiation. This radiation can excite another electron ( $E_{S2}$ ) to overcome its binding energy and reach the vacuum level. (c) XAS: The absorption of a photon to excite a core level electron to a previously unoccupied valence band state.

50–1500 eV, in contrast to “hard” X-rays, which correspond to light energy between 1500–15000 eV and ultraviolet (UV) light, which has an energy range up to about 50 eV. Core levels contain information regarding the electronic structure of the investigated material.

Core levels with spin-orbit coupling appear as doublets. The shape of a core level peak is a convolution of a Lorentzian function which accounts for the inherent width of the peak according to the uncertainty principle and a Gaussian function which accounts for the width of the photon source, the analyser resolution and thermal broadening. The inherent width of a core level is directly related to the lifetime of the ion state after photoemission,  $\tau$ , [10] as follows:

$$\Gamma \sim \frac{\hbar}{\tau} . \quad (2.17)$$

The Lorentzian shape is substituted by a Doniach-Šunjić shape when the probed material is metallic [11]. A Doniach-Šunjić function is a Lorentzian function with an asymmetric tail. This tail is evident towards the low  $E_K$  and arises from a distribution of unfilled one-electron levels above the Fermi energy.

The electrons reaching the analyser are sampled from the top 10–20 Å of a sample as described by the characteristic attenuation depth of the emitted electron in figure 2.3. If the attenuation length of the emitted electrons through a given material is known, one can calculate the thickness of an overlayer.

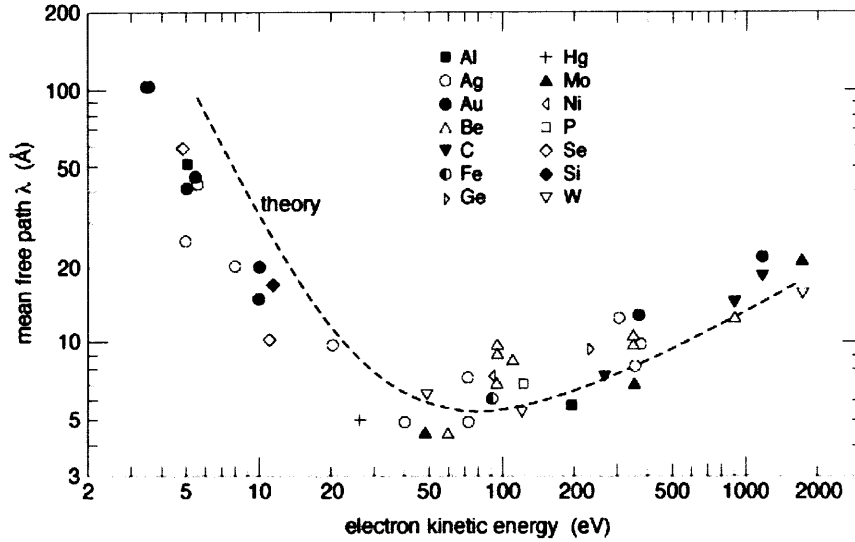


Figure 2.3: Electron attenuation length as a function of energy as determined by experimental results for a range of materials [12].

## 2.4 Auger electron spectroscopy (AES)

AES utilises the Auger effect in order to provide information on the chemical composition of a surface and also some estimation of stoichiometry. The Auger effect was independently discovered by Lise Meitner in 1923 and two years later by Pierre Victor Auger and it is named after the latter. The Auger process is initiated by provision of energy which is usually in the form of X-rays or electrons. The 3 step process involves secondary electron emission after the production of a core hole, as illustrated in figure 2.2b. The  $E_K$  of the Auger electron can be described as follows:

$$E_K = E_A - E_B - E_C , \quad (2.18)$$

where  $E_A$  is the energy level of the core hole,  $E_B$  is the initial energy level of the decaying



electron and  $E_C$  is the initial state of the emitted electron. The  $E_K$  of the emitted electron depends on the interplay between different atomic energy levels, and hence provides an elemental fingerprint.

## 2.5 X-ray absorption near edge spectroscopy (XANES)

XANES is a characterisation technique which provides both structural and chemical information. X-ray absorption spectroscopy (XAS) is the process whereby a core level electron is excited by X-rays to an initially empty valence orbital, as shown in figure 2.2c. In this technique, the photon energy of synchrotron radiation is scanned and a signal proportional to the number of photons absorbed is recorded.

The XANES part of XAS is defined as the absorption edge up to about 50 eV. A detailed overview of the technique is given by Stöhr [13]. The coordination geometry of the adsorbing atom gives rise to particular spectral features. The chemical shift in the position of the edge arises due to the variation of shielding of the core electrons from the nucleus, associated with the number of electrons in the valence band.

# References

- [1] G. Binnig, H. Rohrer, Ch. Gerber, and E. Weibel, *Phys. Rev. Lett.* **49**, 57 (1982).
- [2] J. Bardeen, *Phys. Rev. Lett.* **6**, 57 (1961).
- [3] J. Tersoff and D. R. Hamann, *Phys. Rev. B* **31**, 805 (1985).
- [4] N. D. Lang, *Phys. Rev. Lett.* **56**, 1164 (1986).
- [5] N. D. Lang, *Phys. Rev. Lett.* **55**, 230 (1985).
- [6] C. J. Chen, *Phys. Rev. Lett.* **65**, 448 (1990).
- [7] D. Drakova, *Rep. Prog. Phys.* **64**, 205 (2001).
- [8] D. A. Bonnell, *Prog. Surf. Sci.* **57**, 187 (1998).
- [9] L. J. Clarke, *Surface crystallography: An introduction to Low Energy Electron Diffraction* John Wiley & Sons, Chichester (1985).
- [10] D. Briggs and M. P. Seah, *Practical surface analysis: Volume 1, Auger and X-ray Photoelectron spectroscopy*, 2nd ed., John Wiley & Sons, Chichester (1990).
- [11] S. Doniach and M. Šunjić, *J. Phys. C* **3**, 285 (1970).

- [12] A. Zangwill, *Physics at surfaces*, Cambridge University Press, Cambridge (1998).
- [13] J. Stöhr, *NEXAFS Spectroscopy* Springer-Verlag, Berlin (1992).

## Chapter 3

# Instrumentation

This chapter briefly describes the instrumentation used. The STM experiments were performed in instruments which were initially set up at the Department of Chemistry, University of Manchester and subsequently transferred to University College London laboratories. The synchrotron radiation studies were performed using beamline I311 at MAX-lab II.

All experiments were carried out in ultra high vacuum (UHV) in order to minimise the interaction of the surface with molecules in the environment. By considering the kinetics of a gas at room temperature and assuming that each particle colliding with the surface adheres, it can be calculated that the surface would be completely covered with a layer after a few hours in a pressure of  $1 \times 10^{-10}$  mbar [1]. Moreover, for some techniques, such as those using electron energy analysers, vacuum is necessary for the measurements.

### 3.1 The UHV scanning tunnelling microscope systems

Two commercial STM instruments were employed, both manufactured by *Omicron NanoTechnology GmbH*. They are described as low temperature (LT) and variable temperature (VT) microscopes, depending on their range of operation. The LT operates at temperatures between 4 K and room temperature, whereas the VT has a range between 20 and 1500 K. Schematic diagrams of the chambers are depicted in figures 3.1 and 3.2, respectively. The STM stages are suspended by a spring mechanism and positioned in the centre of eddy-current damping systems to suppress vibrations. The chambers are supported on viton stacks, further reducing any vibrations.

Although both STM instruments can record data at temperatures between 20 K and room temperature, LT-STM is preferred for measurements below room temperature. This is because the LT is cooled by cryostats which surround the STM stage. As a result, the temperature of the entire LT-STM stage (including sample and tip) reaches thermal equilibrium after a few hours.

In contrast, the VT-STM is cooled by clamping a cooling block to the sample, with the clamp itself cooled via a ribbon connected to a flow cryostat. There are two disadvantages with such a cooling mechanism. First, the tip is only cooled by thermal exchange with the sample. Consequently, thermal drift arises from the temperature gradient between sample and tip. This can be compensated to an extent by fast scanning. The second disadvantage of the VT cooling system is the appearance of noise, caused by boiling in the cryostat or in the vacuum line between this and the cryogenics dewar or rotary pump.

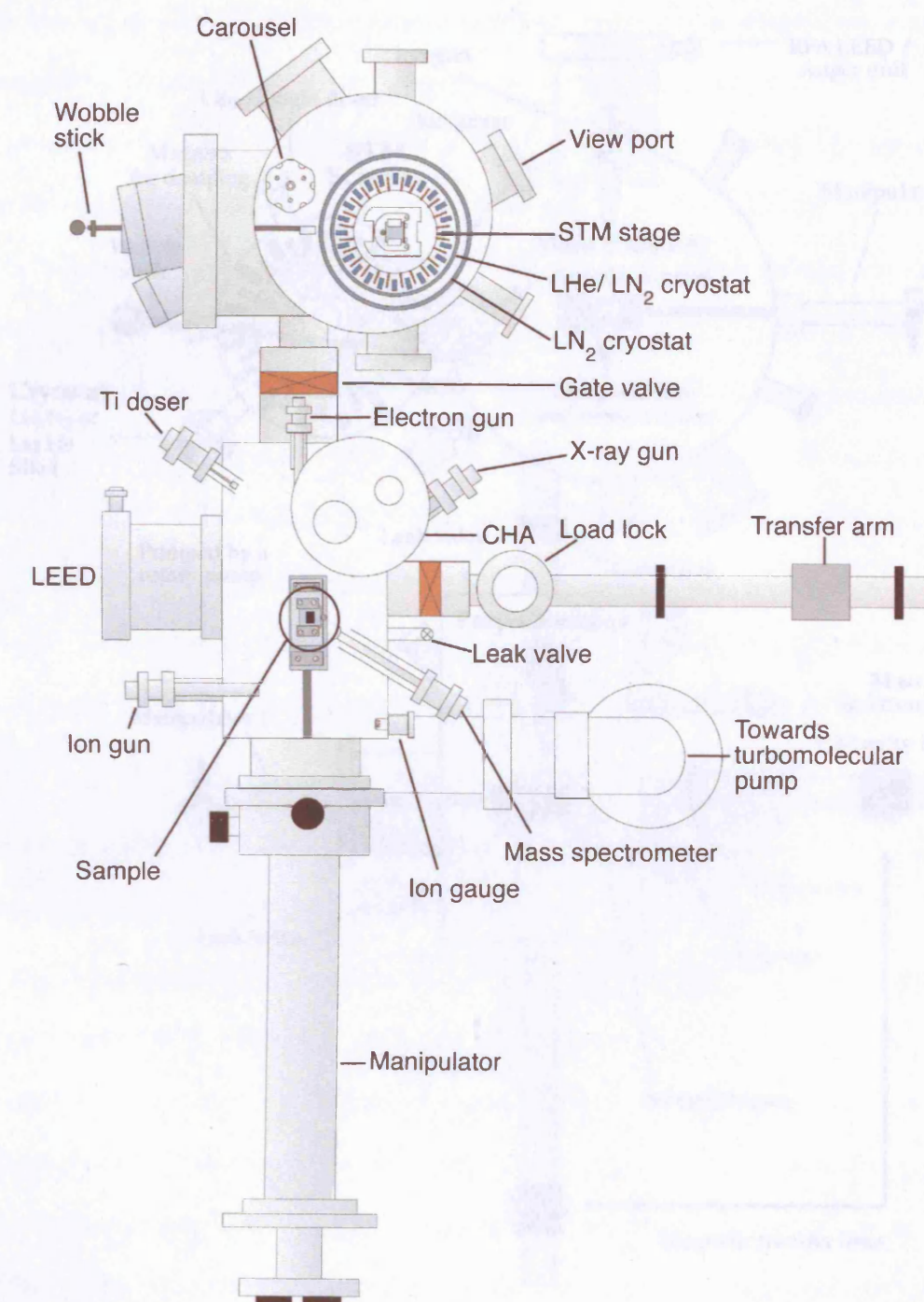


Figure 3.1: Schematic diagram of the LT-STM (top view; chambers presented in cross-sections).

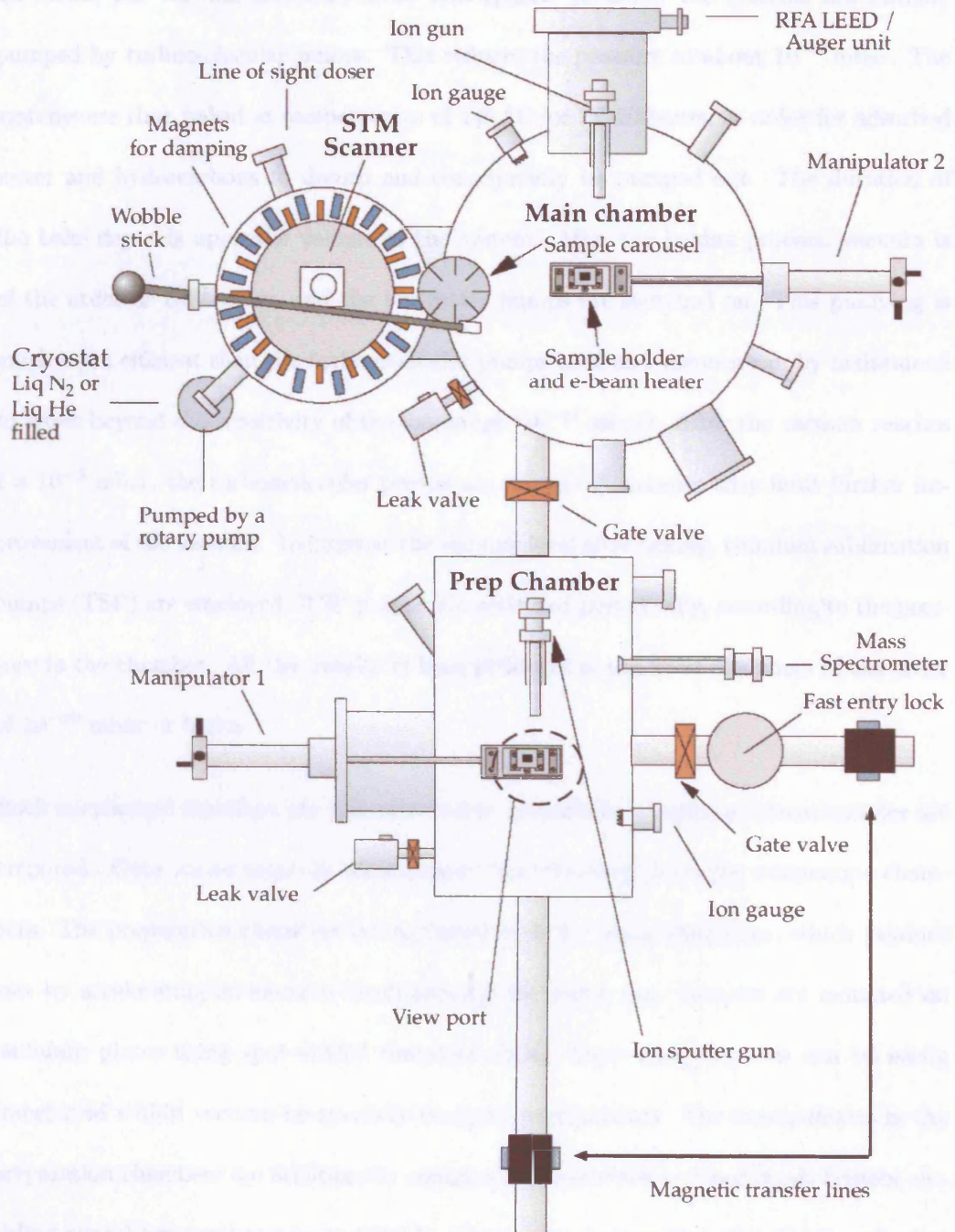


Figure 3.2: Schematic diagram of the VT-STM (top view; chambers presented in cross-sections).

To create the vacuum necessary from atmospheric pressure, the systems are initially pumped by turbomolecular pumps. This reduces the pressure to about  $10^{-5}$  mbar. The systems are then baked at temperatures of 145 °C for 12-20 hours, in order for adsorbed water and hydrocarbons to desorb and consequently be pumped out. The duration of the bake depends upon the volume of the system. After the baking process, vacuum is of the order of  $10^{-7}$  mbar, and the ion getter pumps are switched on. This pumping is much more efficient than the turbomolecular pumps used and vacuum can be maintained to levels beyond the sensitivity of the ion gauge ( $10^{-11}$  mbar). After the vacuum reaches  $1 \times 10^{-9}$  mbar, the turbomolecular pumps are valved off, because they limit further improvement of the vacuum. To improve the vacuum level after baking, titanium sublimation pumps (TSP) are employed. TSP pumps are activated periodically, according to the pressure in the chamber. All this results in base pressures in the STM chambers of the order of  $10^{-10}$  mbar or better.

Both microscope chambers are also attached to preparation chambers, where samples are prepared. Gate valves separate these preparation chambers from the microscope chambers. The preparation chambers are equipped with  $\text{Ar}^+$  sputtering guns, which produce ions by accelerating an electron beam through the argon gas. Samples are mounted on tantalum plates using spot-welded tantalum clips. These sample plates can be easily transferred within vacuum by specially designed manipulators. The manipulators in the preparation chambers are additionally equipped with electron bombardment heaters, enabling anneal temperatures up to 2000 K. The sample temperature was monitored using a pyrometer. This is achieved by passing a current through a tungsten filament located behind the sample plate. Electrons are emitted from the filament and accelerated towards



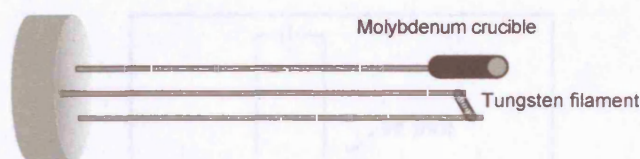


Figure 3.3: Schematic diagram of the metal evaporator.

the sample plate by a bias (0.5–2 kV) applied between the sample plate and the filament. Quadrupole mass spectrometers are attached to either or both of the preparation chambers and microscope chambers for monitoring the partial pressures of residual gases.

In addition to STM, the microscope chambers are equipped with surface characterisation techniques such as LEED and AES. XPS and UPS (ultra-violet photoelectron spectroscopy) are also available in the LT-STM.

### 3.1.1 Metal evaporator

An electron bombardment titanium doser was attached to the preparation chambers, for the film preparation. The evaporator consists of a titanium source placed in a molybdenum crucible opposite a tungsten filament, as shown in figure 3.3. By passing a current through the filament, electrons are emitted. These electrons are accelerated towards the crucible by applying a high bias between the crucible and filament (typically  $\sim 1000$  V). Heating the crucible in this way results in sublimation of the metal source. The emission current from the evaporator (typically on the order of 10 mA) gives an estimation of the quantity of metal sublimed which can be related to the coverage at the sample surface.

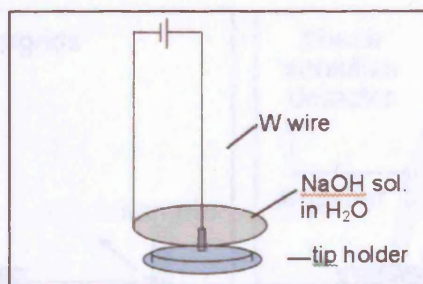


Figure 3.4: Schematic illustration of the tip etching.

### 3.1.2 Tip fabrication

Ideally, tunnelling in STM should be performed by a tip terminated with a single, known atom. Practically, there is no technique which can characterise an STM tip to such an extent. Empirically, macroscopically sharp, symmetric tips (as judged from an optical microscope) are known to be suitable for STM imaging. Tungsten is widely used for tips due to its hardness, and has been employed in these studies as well.

Electrochemical etching, as illustrated in figure 3.4, was used to prepare the W tips used in this work. By means of surface tension, a solution of NaOH in distilled water is held within a stainless steel ring and acts as the cathode. The W wire (*Goodfellows 99.9%, 0.3 mm diameter*) is placed through the centre of the ring and forms the anode. The W wire is therefore etched at the air-electrolyte interface. As the wire is etched, the pull of gravity elongates the neck formation, resulting in a sharp tip. Once the tip drops off, it is thoroughly rinsed with distilled water. Further cleaning of the tip is performed in UHV by annealing the tip to  $\sim 100$  °C.



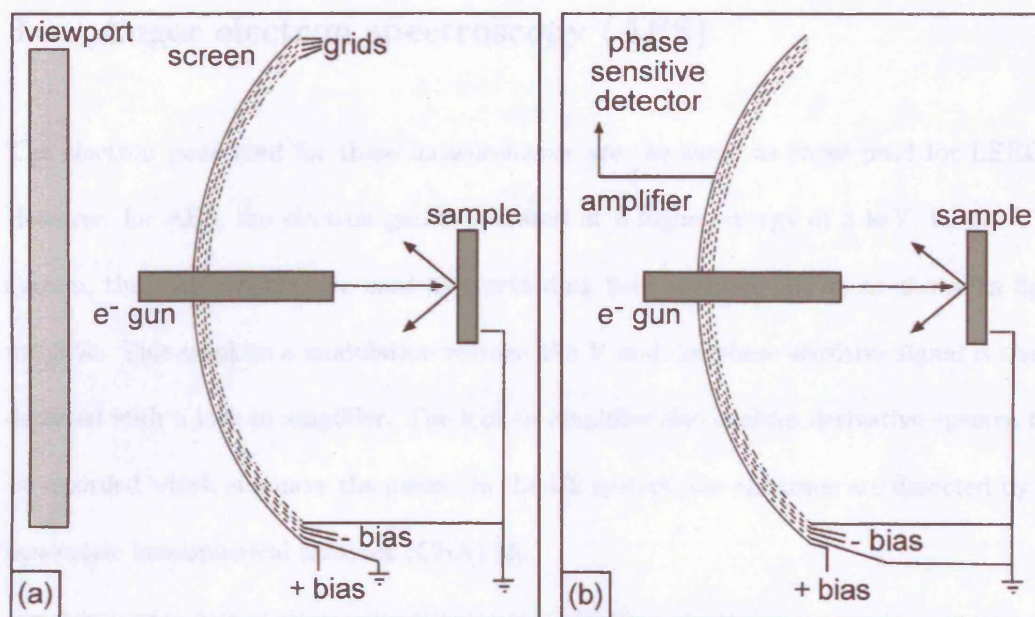


Figure 3.5: (a) Schematic representation of LEED optics. (b) Schematic diagram of the LEED optics working in RFA Auger mode.

### 3.2 Low Energy Electron Diffraction (LEED)

The LEED employs an electron gun to direct electrons (with typical energies of 20–200 eV) at the sample surface. The energy spread of the beam is of the order of 0.5 eV resulting in finite dimensions of the resulting spots. The reverse view optics utilise four concentric grids, before illuminating the diffracted electrons on a phosphorescent screen (see figure 3.5a). The first and last grids are earthed, as is the sample. The sandwiched grids are held at about the potential of the electron source filament, so that any inelastically scattered electrons are retarded. The elastically scattered electrons are then accelerated towards the screen, which is positively biased.

### 3.3 Auger electron spectroscopy (AES)

The electron guns used for these measurements are the same as those used for LEED. However, for AES, the electron gun is operated at a higher energy of 3 keV. In the VT system, the LEED optics are used as a retarding field analyser (RFA) as shown in figure 3.5b. This employs a modulation voltage of 5 V and the phase sensitive signal is then detected with a lock-in amplifier. The lock-in amplifier also enables derivative spectra to be recorded which enhances the peaks. In the LT system, the electrons are detected by a concentric hemispherical analyser (CHA) [2].

### 3.4 X-ray photoelectron spectroscopy (XPS)

For this technique, an X-ray source and an electron energy analyser are required. In the present work, XPS was performed in the LT-STM UHV system and in synchrotron radiation facilities. In the LT-STM UHV system, X-rays are produced by bombarding a solid target (Mg or Al) with high energy electrons (typically with 12–13 keV and 15 mA). The emission from the target is composed of the characteristic line emissions. The X-ray gun used for this set of experiments uses an Al target which emits  $K_{\alpha}$  X-rays at 1253.6 eV; a choice based on the resulting X-ray and Auger peak positions of a Ni-Ti-O system. The electron energy analyser attached to the STM system is a CHA.

Synchrotron radiation light has the additional advantage of providing photons of high and tunable energy. The high resolution photoemission experiments reported here employed beamline I311 at MAX-lab II [3] based in Lund University, Sweden. The beamline is

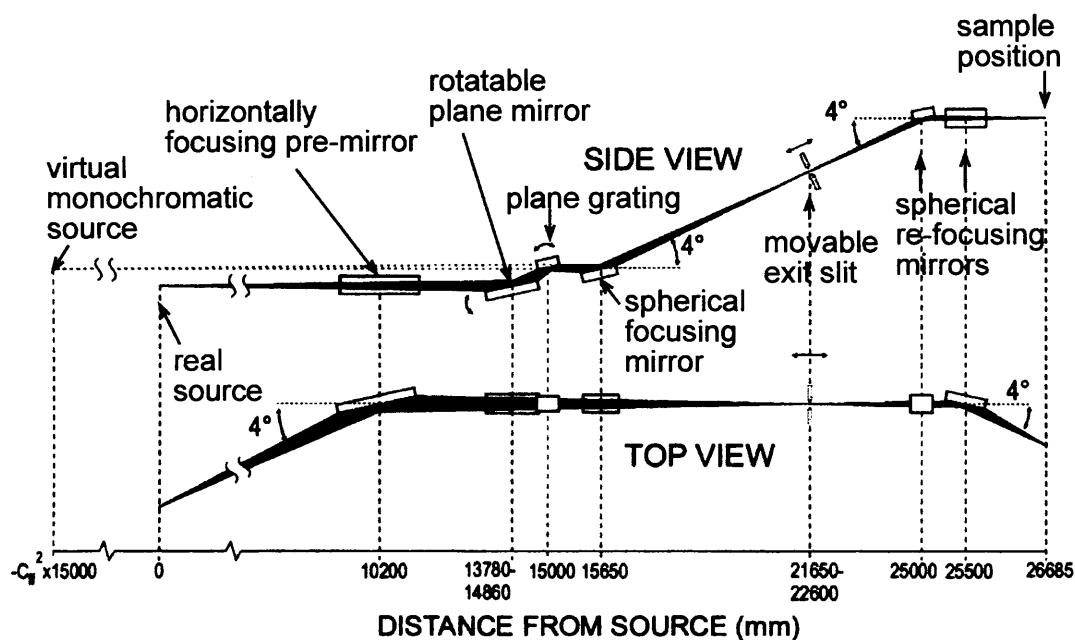


Figure 3.6: Schematic layout of the I311 beamline at MAX-lab II [3].

depicted schematically in figure 3.6. This beamline uses undulator radiation in the energy range of 30–1500 eV. The energy resolution of the monochromator output is  $E/\Delta E = 5 \times 10^3 - 2 \times 10^4$ . The photon current is reported to be  $(5 - 10) \times 10^{10} \text{ ph}\cdot\text{s}^{-1}$  into the area of the focused photon beam,  $0.3 \times 1.0 \text{ mm}^2$  [4]. The monochromator is a modified SX-700 with  $1220 \text{ l}\cdot\text{mm}^{-1}$  grating, a spherical focusing mirror and a movable exit slit. The synchrotron radiation light was  $p$  polarised, resulting in a polarisation parallel to the  $[1\bar{1}0]$  symmetry axis of the nickel substrate, and had an incidence angle of  $45^\circ$ .

Photoelectrons were collected at normal emission using a hemispherical SCIENTA-SES200 electron energy analyser. The angle between the incoming photon beam and the analyzer is  $55^\circ$ . The end station was operated at a base pressure of  $< 10^{-10} \text{ mbar}$  and was equipped with a LEED system, the electron beam Ti doser described above and typical facilities

for crystal preparation as well as molecule dosing. A differential pumping system between the refocusing mirrors and the end-station enables recording of XPS spectra during an adsorption process at a pressure up to  $10^{-5}$  mbar [3].

### 3.5 X-ray absorption near edge spectroscopy (XANES)

XANES measurements were taken on beamline I311 at MAX-lab [3] described above, using the SCIENTA-SES200 analyser. The XANES spectra presented here were obtained by measuring the partial electron yield as a function of photon energy scanned through the Ti  $L_{2,3}$  edge. All XANES experiments were performed at room temperature. The kinetic energy range was calibrated by referring to the positions of the first and second order excitations of the Ni 3p core levels.

# References

- [1] G. Attard and C. Barnes, *Surfaces*, Oxford Chemistry Primers, Oxford University Press, Oxford (1998).
- [2] D. Briggs and M. P. Seah, *Practical Surface Analysis by Auger and X-Ray Photoelectron Spectroscopy*, John Wiley & Sons, New York (1984).
- [3] R. Nyholm, J. N. Andersen, U. Johansson, B. N. Jensen, and I. Lindau, *Nucl. Instrum. Methods Phys. Res., Sect. A* **467**, 520 (2001).
- [4] J. Weissenrieder, A. Mikkelsen, J. N. Andersen, P. J. Feibelman, and G. Held, *Phys. Rev. Lett.* **93**, 196102 (2004).

## Chapter 4

# Growth and reactivity of titanium oxide ultrathin films on Ni(110)

Soft X-ray photoelectron spectroscopy (SXPS) and X-ray adsorption near edge spectroscopy (XANES) have been combined with LEED to examine the growth of titanium dioxide thin films on Ni(110). Depending on the initial titanium coverage, the formation of two different films is observed, a quasi-hexagonal phase and a film with rutile (110) rods. The spectroscopy indicates that all films consist of fully oxidised titanium. Furthermore, the reactivity of the higher coverage phase, consisting partly of rutile TiO<sub>2</sub>(110), was investigated after exposure to molecular water at 190 K. The formation of molecular water and hydroxyls was observed for low-pressure exposure (less than 10<sup>-7</sup> mbar). High-pressure exposure (of the order of 10<sup>-6</sup> mbar) resulted in hydroxylation of the thin film, which was found to be reversible upon annealing.



## 4.1 Introduction

Thin oxide films have been the subject of numerous studies in the past few decades [1]. In particular, intense efforts have been made to elucidate, on the atomic scale, the interface between metals and oxides. This interest is fuelled by the quest to find nanostructures which can be exploited in electronic devices, by the importance of thin oxide films as corrosion-inhibitors [2], and by the use of thin oxide films as models for the catalyst supports [3-5]. Moreover, thin oxide films can act as mimics of the native surfaces, with the advantage that the metallic substrate provides the necessary conductivity required for some characterisation techniques. For most systems attention has focused on the characterisation of the coverage/oxidation surface phase diagram, with more recent studies probing their reactivity [6].

Titanium dioxide, and in particular its most stable surface, the rutile (110) plane (figure 4.1c), is considered the ‘prototypical’ oxide [7] and has been extensively investigated in surface science. Our work was inspired by an early study of the growth of titania on  $\text{Ni}_{94}\text{Ti}_6(110)$  alloy, which demonstrated, by X-ray photoelectron diffraction (XPD) measurements, the presence of rutile  $\text{TiO}_2(110)$  [2]. Previous work confirms that similar thin titanium oxide films can be formed without using NiTi alloys by instead depositing Ti onto pure Ni(110) surfaces [8-10]. In the present study, we employed synchrotron radiation SXPS and XANES combined with LEED to characterise the growth of ultrathin films of  $\text{TiO}_x$ .

In addition to the structural characterisation, we have investigated the reactivity of the rutile thin film using  $\text{H}_2\text{O}$  as a probe and compared this behaviour with that of the (110)

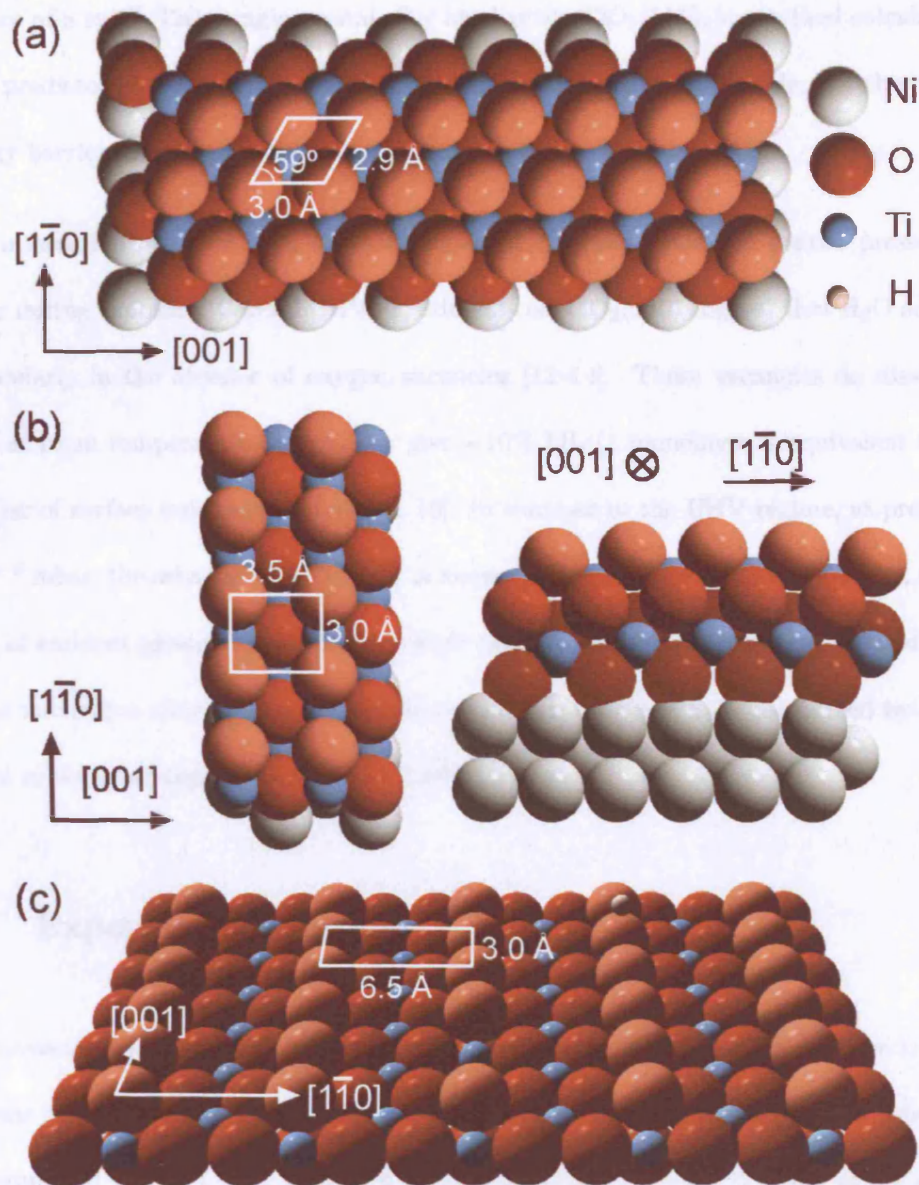


Figure 4.1: Models of the surfaces. (a) Model of the TiO<sub>2</sub> quasi-hexagonal phase grown on Ni(110), as proposed by Atrei *et al.* [2]. The unit cell is indicated. The axes display the orientation of the substrate. (b) Top and side view of a proposed model for the wetting layer phase grown on Ni(110). The unit cell is indicated. The axes display the orientation of the substrate. (c) A model of the rutile TiO<sub>2</sub>(110) surface as typically prepared in UHV, containing an OH group and an oxygen vacancy. The unit cell and the high symmetry axes of the rutile TiO<sub>2</sub>(110) surface are displayed. The TiO<sub>2</sub> [110] direction grows parallel to the Ni [001] direction.

surface of a rutile  $\text{TiO}_2$  single crystal. For ideal rutile  $\text{TiO}_2(110)$ , theoretical calculations have predicted that dissociation of  $\text{H}_2\text{O}$  is thermodynamically favourable, but there is an energy barrier associated with the mobility of  $\text{H}_2\text{O}$  on the surface [11].

The interaction of water with an oxide depends critically upon the partial pressure of water during exposure. Several UHV experiments on  $\text{TiO}_2(110)$  suggest that  $\text{H}_2\text{O}$  adsorbs molecularly in the absence of oxygen vacancies [12–14]. These vacancies do dissociate  $\text{H}_2\text{O}$  at room temperature to typically give  $\sim 10\%$  ML (1 monolayer is equivalent to the number of surface unit cells) of OH [12, 15]. In contrast to the UHV regime, at pressures  $> 10^{-6}$  mbar, the selvedge of  $\text{TiO}_2(110)$  is known to hydroxylate [16, 17]. However, recent work at ambient pressure (up to 2.6 bar)  $\text{H}_2\text{O}$  exposure suggests that the surface hydroxyls act as nucleation sites for water adsorption and their coverage does not exceed twice the initial coverage of oxygen vacancy sites [18].

## 4.2 Experimental Section

The measurements reported here employed beamline I311 at MAX-lab II [19], described in sections 3.4 and 3.5. The end station was operated at a base pressure of  $< 10^{-10}$  mbar and was equipped with a LEED system, a home made electron beam Ti doser and standard facilities for crystal preparation and molecule dosing.

The Ni(110) surface was prepared by cycles of argon sputtering and annealing to 1070 K until a sharp  $(1\times 1)$  LEED pattern was obtained and no contamination was detected by SXPS. All LEED patterns were recorded at room temperature. Ultrathin films of  $\text{TiO}_x$

were grown *in situ* as follows. Ti was deposited on the substrate held at room temperature in vacuum, subsequently oxidised in a flow of  $1 \times 10^{-7}$  mbar of O<sub>2</sub> and annealed at 800 K. Water was double distilled, and purified by freeze-pump-thaw cycles. The water was dosed at a sample temperature of 190 K using two different pressure regimes,  $10^{-8}$  and  $10^{-6}$  mbar.

Regarding the SXPS spectra, the binding energy scale was calibrated with respect to the Fermi energy of the nickel crystal, since the films were thin enough to allow the detection of nickel in the valence band spectra. The Ni 2p, O 1s and Ti 2p core levels were excited with photon energies of 1000, 650, and 680 eV, respectively. SXPS spectra were recorded at room temperature unless otherwise stated. The raw core level spectra were fitted using a sum of Voigt-type functions. The width of the Lorentzian or Doniach-Šunjić (used where appropriate [20]) contribution to the peaks was kept constant. The width of the Gaussian contribution was allowed to vary, accounting for temperature effects. A Shirley-plus-polynomial fit was used to model the background [21], using a least-squares method to optimise the fits.

The possibility of photon beam modification of adsorbed H<sub>2</sub>O has recently been studied by Weissenrieder *et al.* for Ru{0001} [22] using beamline I311 at MAX-lab II. This is the same beamline as employed in the present work. They report a photon current of  $(5 - 10) \times 10^{10}$  ph·s<sup>-1</sup> into the area of the focused photon beam,  $0.3 \times 1.0$  mm<sup>2</sup>. This is smaller by a factor of 3.3 than the flux reported in earlier work on H<sub>2</sub>O on TiO<sub>2</sub>(110) [14], where no photon-induced dissociation was observed after exposure to the photon beam for about an hour. On this basis, we can assume that there is no beam induced dissociation

in the present experiments.

Additional structural characterisation was performed using the *Omicron* LT-STM system, described in detail in section 3.1. The Ni crystal and the films were prepared following the same procedure as described above. This UHV system operated at a base pressure of  $5 \times 10^{-11}$  mbar.

## 4.3 Results and Discussion

### 4.3.1 The Phases Formed

#### 4.3.1.1 The Quasi-Hexagonal Phase

A quasi-hexagonal phase described by the matrix  $\begin{bmatrix} 1 & -3/7 \\ 0 & 6/7 \end{bmatrix}$  is obtained upon saturated oxidation of less than a monolayer equivalent (MLE, with 1 MLE corresponding to a coverage of 1 Ti atom per substrate surface unit cell) of Ti on Ni(110) [10] and was initially observed by Atrei *et al.* on Ni<sub>94</sub>Ti<sub>6</sub>(110) [2]. The current model for this phase is a layer of titanium sandwiched between oxygen layers (figure 4.1a). For the thin film formed on Ni(110) at MAX-lab, the LEED pattern (figure 4.2a) is described by the matrix  $\begin{bmatrix} 2 & -6/7 \\ 0 & 12/7 \end{bmatrix}$  (marked by ‘-’ in figure 4.2b), which is a (2×2) reconstruction of the Atrei *et al.* quasi-hexagonal phase [2]. Additionally, the extra spots on the half order of the Ni  $[1\bar{1}0]$  direction are most probably caused by a (2×1) oxygen reconstruction of the Ni substrate [23], as the titanium coverage is too low to cover the entire surface. The LEED

pattern obtained in this work is of higher quality than those in previous studies, indicating that the quasi-hexagonal structure proposed by Atrei *et al.* might not be the primary unit cell. Our unit cell is also twice that reported in our earlier STM investigation [10]. This discrepancy could arise from a  $z$ -direction relaxation of substrate atoms or thin film atoms not visible in the STM images.

#### 4.3.1.2 The Rutile $\text{TiO}_2$ Islands on the Wetting Layer of $\text{TiO}_2$

For higher Ti coverage (in the range of about 1–6 MLE [24]), under the same preparation conditions, it has been shown that three-dimensional rods of rutile  $\text{TiO}_2(110)$  grow on a wetting layer on top of  $\text{Ni}(110)$  [9]. Figure 4.3 shows the STM topography of such a film. The film consists of 2.5 MLE Ti annealed to 800 K for 30 min in  $10^{-7}$  mbar  $\text{O}_2$ . The coverage was estimated by calibration of the doser using Auger electron spectroscopy. The LEED pattern of this phase was described in ref. [2] as showing a  $5\times$  periodicity with respect to the substrate in the  $[1\bar{1}0]$  direction, where not all five spots are evident on the LEED photograph, and with streaking along the  $[001]$  direction.

Careful inspection of the LEED patterns (figure 4.2c,e) and the corresponding STM image (figure 4.3d) allows us to determine the epitaxy matrix which describes the unit cell of this wetting phase layer with respect to the Ni substrate as  $\begin{bmatrix} 6/5 & 0 \\ 0 & 1 \end{bmatrix}$ . This results in a unit cell of  $3.0\times 3.5 \text{ \AA}^2$ . In light of the STM evidence, these additional spots can be attributed either to the unit cell of the wetting layer and its multiple diffraction spots, or to a coincidence cell between the wetting layer and the substrate. The LEED pattern of the same phase (figure 4.2e–f), recorded on a different UHV system (LT-STM) at lower



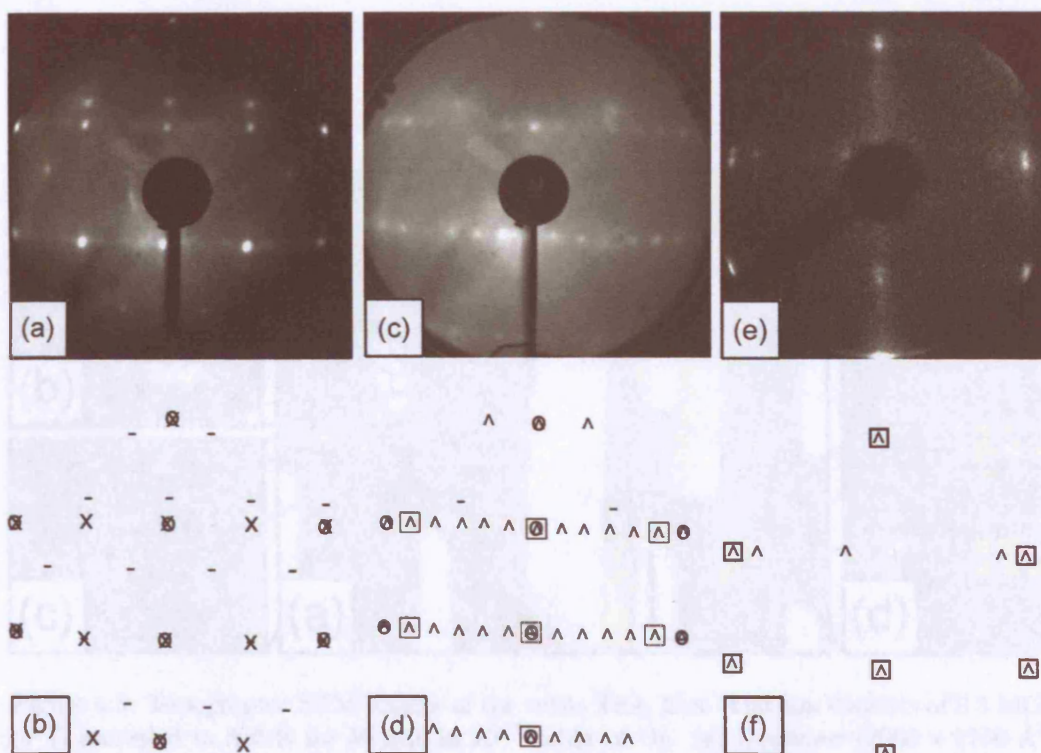


Figure 4.2: (a) LEED pattern (128 eV) of the quasi-hexagonal phase (subMLE Ti annealed to 800 K for 30 min in  $10^{-7}$  mbar  $O_2$ ) compared with (b) a schematic representation of the diffraction pattern. (c) LEED pattern of the rutile  $TiO_2(110)$  overlayer (5 MLE Ti oxidised for 1 min in  $10^{-7}$  mbar  $O_2$  and annealed to 800 K) recorded on the beamline end station (123 eV) with (d) the corresponding schematic representation of the diffraction pattern. (e) LEED pattern of the rutile  $TiO_2(110)$  overlayer (2.5 MLE Ti annealed to 800 K for 30 min in  $10^{-7}$  mbar  $O_2$ ) obtained on LT-STM (58 eV) with (f) the corresponding schematic representation of the diffraction pattern. Circles mark the periodicity of Ni(110), crosses mark a  $(2 \times 1)$  periodicity of the Ni substrate, ‘-’ mark the quasi-hexagonal structure, squares indicate the periodicity of the wetting layer and ‘^’ spots show its multiple diffraction spots and/or a coincidence cell between the wetting layer and the substrate. The  $TiO_2(110)$  contribution is evident along its [001] azimuth, along which it coincides with the wetting layer. No spots are observed in the  $TiO_2$   $[1\bar{1}0]$  azimuth due to the small width of the islands in that direction.

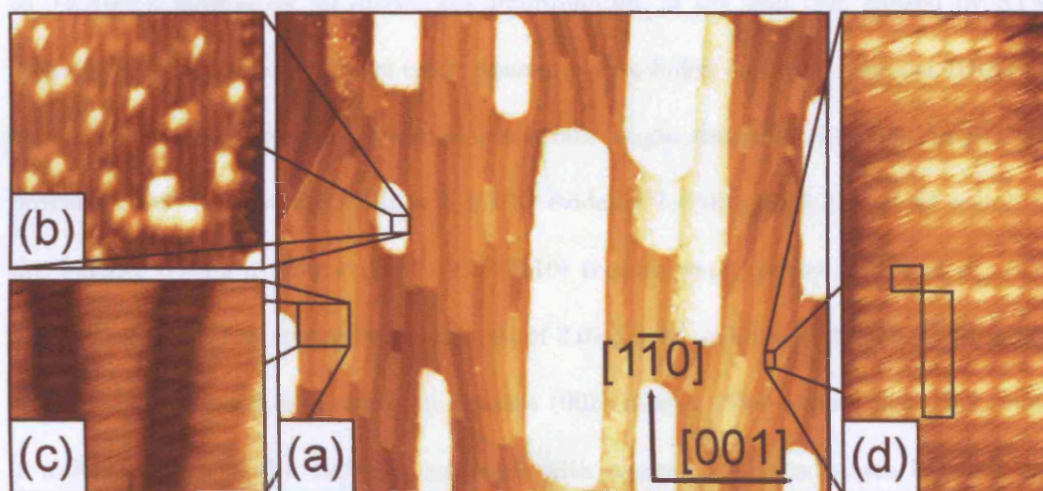


Figure 4.3: Topographic STM images of the rutile  $\text{TiO}_2$  film. The film consists of 2.5 MLE of Ti annealed to 800 K for 30 min in  $10^{-7}$  mbar of  $\text{O}_2$ . (a) Overview ( $2000 \times 1750 \text{ \AA}^2$ ; tunnelling conditions: 1.30 V sample bias, 0.10 nA tunnelling current). The symmetry of the Ni(110) substrate is indicated. (b) High resolution image showing a  $\text{TiO}_2(110)$  island with the characteristic O vacancies and bridging OH groups. ( $65 \times 65 \text{ \AA}^2$ ; tunnelling conditions: 1.15 V sample bias, 0.1 nA tunnelling current) (c) STM image of the wetting layer, showing the 40 Å periodicity along the [001] direction of the substrate ( $185 \times 155 \text{ \AA}^2$ ; tunnelling conditions: 1.00 V sample bias, 1.00 nA tunnelling current) (d) Atomically resolved image of the wetting layer. A  $(1 \times 1)$  unit cell and a coincidence cell between the wetting layer and the substrate, resulting in a Moiré pattern are indicated. ( $35 \times 60 \text{ \AA}^2$ ; tunnelling conditions: 0.64 V sample bias, 0.23 nA tunnelling current). Images (a)-(b) recorded at 300 K, images (c)-(d) recorded at 78 K.



energy, reveals a splitting of the wetting layer unit cell spots. This splitting is consistent with a  $40 \pm 5 \text{ \AA}$  periodicity of the wetting layer in the substrate [001] direction, which is also visible in the corresponding STM image (figure 4.3c). Hence, our wetting layer has a supercell of  $15 \times 40 \text{ \AA}^2$ . This phase had been assigned in previous work [9, 10] to  $\text{TiO}(001)$ , because of an inaccurate determination of the unit cell, caused by STM drifting. The formation of nickel oxide phases was excluded based on the past HREELS measurements [8]. Given the additional accurate length determination that LEED can provide, we notice that the STM and LEED evidence for this phase is a close match to the wetting titania overlayer on  $(1 \times 2)\text{-Pt}(110)$  recently reported by Orzali *et al.* [25]. The latter, which has an overlayer unit cell of  $3.0 \times 3.9 \text{ \AA}^2$ , exhibits a  $39 \times 16 \text{ \AA}^2$  supercell and can be described as a distorted anatase (001) bilayer. One should note that there is a  $90^\circ$  rotation of the overlayer supercell with respect to the substrate between our phase and the one reported for  $(1 \times 2)\text{-Pt}(110)$ . These differences probably arise due to the heteroepitaxial growth determined by the different substrate surfaces. On the basis of the above observations, figure 4.1b illustrates a proposed atomic model for this wetting layer phase. The streaking of the LEED pattern along the substrate [001] direction is consistent with the width of the rutile rods being too small to reveal the periodicity along the  $\text{TiO}_2(110)$ -overlayer  $[1\bar{1}0]$  direction. The  $\text{TiO}_2(110)$  unit cell length along its  $[1\bar{1}0]$  direction is  $6.5 \text{ \AA}$  compared with  $3.5 \text{ \AA}$  for the wetting layer. Along the  $\text{TiO}_2(110)$  [001] direction, this phase is commensurate with the wetting layer. The LEED pattern of the film grown on beamline I311 is shown in figure 4.2c, and it reveals additional diffuse spots of the quasi-hexagonal film (marked as ‘-’ in figure 4.2d), suggesting that this phase also forms on patches of the surface when the  $\text{TiO}_2(110)$  rods are present. This film was

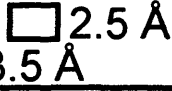
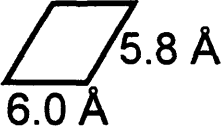
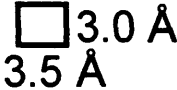
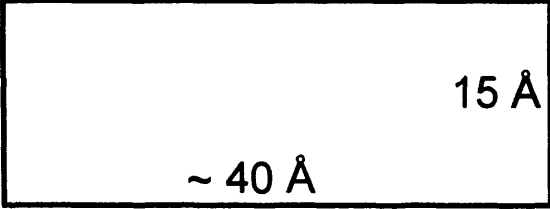
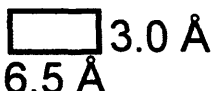
		Substrate: Ni(110) Unit cell 
Ti coverage (MLE) Oxidised to saturation by $10^{-7}$ mbar $O_2$ Annealed to 900 K	< 1 MLE	TiO <sub>2</sub> quasi hexagonal overlayer Unit cell 
	~ 1 MLE	TiO <sub>2</sub> wetting overlayer Unit cell  Supercell 
	> 1 MLE	TiO <sub>2</sub> (110) overlayer on wetting layer Unit cell 

Figure 4.4: An illustration summarising the TiO<sub>2</sub> phases investigated in this paper, indicating their unit cells and their preparation conditions.

prepared by deposition of  $\sim 5$  MLE of Ti (as estimated by looking at the attenuation of the Ni  $2p_{3/2}$  core levels after Ti deposition and assuming a close-packed structure of Ti) oxidised for 1 min in  $10^{-7}$  mbar of  $O_2$  and annealed to 800 K. Figure 4.4 summarises the different phases discussed in this section, alongside their corresponding unit cells and preparation conditions.

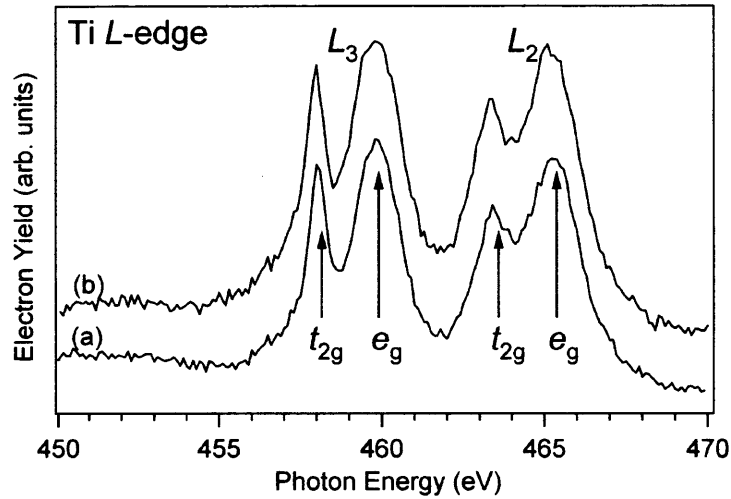


Figure 4.5: XANES over the Ti  $L$ -edge described in the text of (a) the thin film mainly of quasi-hexagonal phase, consisting of subMLE Ti annealed to 800 K for 30 min in  $10^{-7}$  mbar  $O_2$ , and (b) the thin film with rutile phase formed, consisting of 5 MLE Ti oxidised for 1 min in  $10^{-7}$  mbar  $O_2$  and annealed to 800 K. The spectra are offset for clarity.

#### 4.3.2 XANES

XANES was employed to provide insight into the structure of the films. The results for the two films described above are shown in figure 4.5. We notice that there are no obvious differences between the two spectra. X-ray absorption spectra over the Ti  $L$ -edge are reported for Ti metal [26], TiO [27],  $Ti_2O_3$  [28],  $NiTiO_3$  [29], and anatase and rutile  $TiO_2$  [30] crystals and can be used as fingerprints in order to identify the phases of the film. Our spectra do not match any of the fingerprints closely enough for a definitive assignment.

The main conclusion that can be drawn from the XANES investigation is that the thin films are fully oxidised and that titanium is in the  $Ti^{4+}$  state. This is evident from the position of the  $L_3$ -edge, which is located at 458 eV [31]. This excludes the presence of  $Ti_2O_3$  or other reduced phases. Also we notice the characteristic splitting of the  $L_2$ - and

the  $L_3$ -edge.

It has been shown by Okada and Kotani [32] that the  $L_2$ - and the  $L_3$ -edges in  $\text{TiO}_2$  split into  $e_g$  and  $t_{2g}$  peaks separated by an energy of about 1.7 eV, assuming an octahedral symmetry. The first-neighbour O atoms are separated by the central Ti atom by 1.946 Å in the  $(1\bar{1}0)$  plane and by 1.984 Å in the  $(110)$  plane; therefore, the resulting structure is a slightly distorted octahedron. The corresponding value for the  $\text{TiO}_2$  films presented here is  $1.8 \pm 0.2$  eV. Therefore, we deduce that titanium atoms are located in the centre of distorted octahedra defined by O atoms at their corners.

In the XANES spectra of the Ti  $L$ -edge, there is a further splitting of the  $e_g$  component, which is usually resolved for the rutile and anatase phases of  $\text{TiO}_2$ . Kecheyev *et al.* [33] have recently reviewed the nature of this splitting. They argue that the most plausible mechanism proposed is associated with long-range order, although this is not fully elucidated. This would imply that interactions of Ti atoms with the second-neighbour shell are important, which will not be present for the quasi-hexagonal phase (figure 4.5b). For the second film, where we have a mixture of rutile, wetting layer, and quasi-hexagonal phases, the absence of a splitting probably results from the surface heterogeneity.

### 4.3.3 SXPS

In an effort to establish the nature of the interaction between the substrate and the two ultrathin films, we looked at the evolution of the Ni  $2p_{3/2}$  core level spectra. The spectrum of the clean metal is characterised by a main peak at  $852.4 \pm 0.1$  eV and a satellite shifted  $5.3 \pm 0.1$  eV toward higher binding energy from the main peak (figure 4.6a). This satellite

arises from final state effects that influence the core level spectra of Ni and its compounds [34]. These final states for the  $2p_{3/2}$  core level are the core level hole,  $2p_{3/2}^5 3d^{10}$ , and the hole generated within the valance band, localised on the photoion,  $2p_{3/2}^5 3d^9$  [35]. The Ni  $2p_{3/2}$  spectrum of NiO is somewhat more complicated, with the appearance of nonlocal screening effects, which are described in detail in ref. [36].

Spectra (b) and (c) in figure 4.6 show the Ni  $2p_{3/2}$  spectra of the substrate after growing the rutile and the quasi-hexagonal film, respectively. Careful examination of the spectra recorded from our films shows subtle changes with respect to the clean surface signal, which indicate that the nickel substrate does not remain inert upon the formation of the thin films. For comparison, the effect of the chemisorption of  $O_2$  on Ni(110) on the peak shape of the Ni  $2p_{3/2}$  core level as a function of  $O_2$  coverage is shown in figure 4.6d–f [37]. The effect of the oxygen chemisorption is manifested by the reduction of the satellite intensity and the additional appearance of new core level states between the main Ni  $2p_{3/2}$  peak and its satellite. These changes differ from those observed on the formation of bulk-like NiO [37]. The changes observed upon oxygen chemisorption of up to  $\sim 1$  ML on Ni(110) are comparable to the changes observed in our Ni spectra after the deposition of the ultrathin films, suggesting that they are caused by oxygen at the interface. Since these changes are observed for both films, it seems unlikely that they arise solely from  $O_2$ -induced reconstruction of Ni(110), which is evidenced only in the LEED pattern of the surface containing the quasi-hexagonal film. The film containing  $TiO_2(110)$  rods does not expose the Ni(110) substrate.

The attenuation of the intensity of the Ni  $2p_{3/2}$  core level under the films was used in order

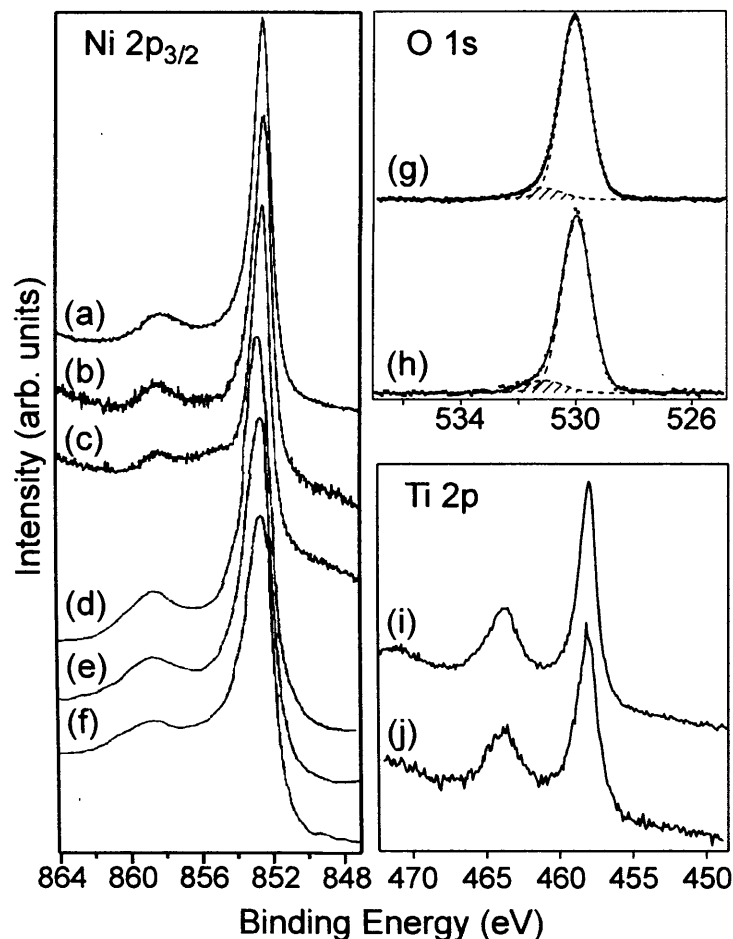


Figure 4.6: Left panel: Ni  $2p_{3/2}$  XPS spectra ( $h\nu = 1000$  eV) of Ni(110) (a) clean surface, (b) with the rutile film and (c) with the quasi-hexagonal film. Ni  $2p_{3/2}$  XPS spectra adapted from Norton *et al.* [37] of Ni(110) (d) clean surface, (e) with a  $\sim 0.44$  ML coverage of chemisorbed oxygen at 295 K and (f) with a  $\sim 1.00$  ML coverage of chemisorbed oxygen at 295 K. The spectra are peak-height normalised and offset for clarity. Top right panel: O  $1s$  XPS spectra ( $h\nu = 650$  eV) (g) of the quasi-hexagonal film and (h) of the rutile film. Circles, dashed lines and solid lines denote the data points, the different components of the fit and the sum of the components respectively. The feature appearing at a shift of 1.13 eV from the bulk oxygen contribution is attributed to OH species. The full width at half maximum (FWHM) of the Gaussian contribution to the components is 1.1 eV and 1.45 eV for the main peak and the OH contribution respectively. All components have a Lorentzian contribution with FWHM of 0.14 eV. The background has been subtracted from the spectra. The spectra are offset for clarity. Bottom right panel: Ti  $2p$  XPS spectra ( $h\nu = 680$  eV) (i) of the quasi-hexagonal film and (j) of the rutile film. The spectra are offset and normalised to the Ti  $2p_{3/2}$  for clarity.

to provide an estimate of the film thickness. This method has an estimated accuracy of  $\pm 50\%$ . At normal emission, these are related by

$$d = -\lambda(E) \ln \frac{I_i}{I_0}$$

where  $d$  is the thickness of the film,  $\lambda(E)$  is the electron attenuation length of electrons at kinetic energy  $E$ ,  $I_i$  is the intensity of the substrate after the deposition of film  $i$ , and  $I_0$  is the intensity of the clean substrate. For  $h\nu = 1000$  eV, Ni 2p<sub>3/2</sub> photoelectrons have kinetic energies of approximately 150 eV and electron attenuation lengths of about 7–8 Å [38]. Hence, we find that the rutile film has an effective thickness of 6.5–10.0 Å.

The oxygen O 1s peak for the ultrathin films is located at  $530.00 \pm 0.15$  eV. This coincides with the reported value for bulk titanium dioxide [39]. A satellite at a higher binding energy of 1.18–1.33 eV appears for the (110) rutile surface [16, 17]. It has been shown that this satellite increases at grazing emission angles and it has been attributed to the surface, twofold, bridging oxygen atoms [16, 17]. The satellite appears for both of our films, with slightly different intensity (see figure 4.6g–h), 9% of the main peak for the quasi-hexagonal film and 10% of the main peak for the film with rutile phase. As we do not expect bridging oxygen atoms in the case of the quasi-hexagonal phase, we suggest instead that it may originate from OH species, resulting from the interaction of the film with the residual H<sub>2</sub>O in the UHV system. This assignment is discussed below in relation to the reactivity of the ultrathin rutile film.

Ti 2p core levels of the ultrathin films are shown in figure 4.6i–j. The final oxidation state of titanium is very similar for both phases. Our films reach the highest oxidation state

when the Ti  $2p_{3/2}$  core level peak has shifted to 458 eV. This value is at the lower limit of the reported values for  $Ti^{4+}$  [5, 39]. The spin-orbit splitting of the Ti 2p core levels is 5.81 eV, which is within the published values for  $TiO_2$  [39]. The shape of the Ti 2p peak of the rutile thin film also matches that reported from the bulk crystal [40]. The full-width at half-maximum of this peak is measured to be  $1.60 \pm 0.04$  eV for the quasi-hexagonal phase and  $1.70 \pm 0.04$  eV for the film with rutile present. It should be noted that there is still some quasi-hexagonal phase on the latter surface, which might explain this broadening. The reported satellites of the Ti 2p peak for rutile  $TiO_2(110)$  at about 3 and 13 eV [41] are present on both films.

The Ti 2p XPS spectrum of the thin film does not have a contribution due to TiO. This is evident by looking in the band of the reported binding energies for  $Ti^{2+}$  (454.6–456.1 eV) (figure 4.7b). Additionally, the electronic structure of fcc TiO was shown by Bartkowski *et al.* [43] to be consistent with the Doniach-Šunjić shape, as would be expected from its metallic character. This is not evident in the Ti 2p spectrum of the rutile ultrathin film. These observations further support the reassignment of the pseudosquare cell [9, 24, 42] wetting layer to anatase-like  $TiO_2(001)$ .

The oxidation of the rutile film was further investigated using SXPS measurements of the Ti 2p core level during exposure of the Ti overlayer to oxygen. The preparation procedure was separated into oxidation and annealing stages, that is, instead of annealing in an  $O_2$  environment, the deposited titanium was initially oxidised and subsequently annealed. The two different procedures produced the same LEED pattern. We notice that after the deposition of titanium, carbon and oxygen contamination is present, evidenced by



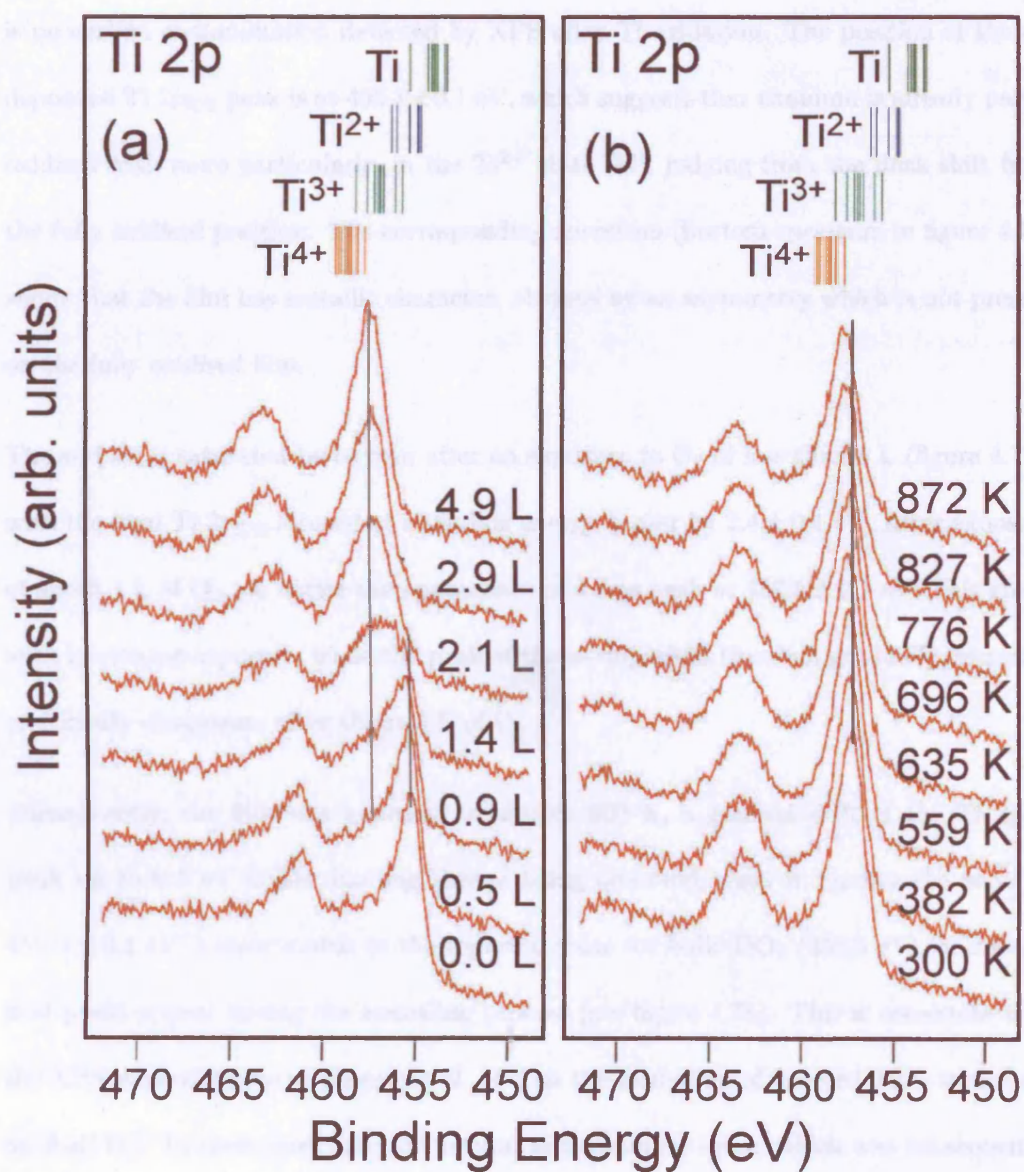


Figure 4.7: Ti 2p XPS spectra ( $h\nu = 680$  eV). (a) The oxidation of the thin film: The oxygen exposure is noted over each spectrum. (b) The annealing of the thin film: The annealing temperature is noted over each spectrum. The spectra are offset for clarity. At the top, the bars display literature positions for Ti 2p<sub>3/2</sub> core level binding energies for different oxidation states of titanium [5, 39].

the appearance of C 1s and O 1s core level peaks. It should also be noted that there is no carbon contamination detected by XPS after Ti oxidation. The position of the as-deposited Ti 2p<sub>3/2</sub> peak is at  $455.1 \pm 0.1$  eV, which suggests that titanium is already partly oxidised and, more particularly, in the Ti<sup>2+</sup> state [44], judging from the peak shift from the fully oxidised position. The corresponding spectrum (bottom spectrum in figure 4.7a) shows that the film has metallic character, obvious by an asymmetry which is not present on the fully oxidised film.

The surface is saturated by oxygen after an exposure to O<sub>2</sub> of less than 5 L (figure 4.7a), with the final Ti 2p<sub>3/2</sub> located at a binding energy higher by  $2.4 \pm 0.1$  eV. After exposure of about 1 L of O<sub>2</sub>, we notice the appearance of a new peak at  $457.5 \pm 0.1$  eV. This grows with increasing exposure, while the peak of the as-deposited titanium gradually decreases and finally disappears after about 3 L of O<sub>2</sub>.

Subsequently, the film was annealed in situ to 900 K, a gradual shift of the Ti 2p<sub>3/2</sub> peak up to 0.5 eV higher binding energy being observed, until it reaches the value of  $458.0 \pm 0.1$  eV, a close match to the reported value for bulk TiO<sub>2</sub> (458.5 eV) [5, 39]. No new peaks appear during the annealing process (see figure 4.7b). This is consistent with the XPS measurements of Biener *et al.* [45] on the formation of ordered TiO<sub>2</sub> structures on Au(111). In their case, after deposition of a titanium layer, which was subsequently oxidised, the Ti 2p core level shifted 1.3 eV toward higher binding energy upon annealing. This phenomenon seems to be characteristic of the oxidation of titanium under these conditions.

#### 4.3.4 Reactivity of the TiO<sub>2</sub>(110) Ultrathin Film

Water was dosed at about 190 K on the thin film with the rutile phase present. According to Henderson [13], a water multilayer does not form on TiO<sub>2</sub>(110) at temperatures above 180 K. The initial exposure was carried out at a pressure of  $4 \times 10^{-8}$  mbar. After an exposure to about 160 L H<sub>2</sub>O two new features appear in the O 1s spectrum, at  $1.13 \pm 0.10$  eV and  $3.00 \pm 0.10$  eV toward higher binding energy (figure 4.8a). There is ambiguity in the literature concerning the identification of the O 1s core level spectrum of OH and molecular H<sub>2</sub>O resulting from exposure of TiO<sub>2</sub>(110) to H<sub>2</sub>O [12, 14, 16–18, 46, 47]. The current consensus on the peak assignment is that the O 1s peak due to hydroxyls appears at lower binding energy than that for water. Considering other oxides, such as  $\alpha$ -Al<sub>2</sub>O<sub>3</sub>(0001),  $\alpha$ -Fe<sub>2</sub>O<sub>3</sub>(0001), Fe<sub>3</sub>O<sub>4</sub>(111) and MgO(100), the feature appearing at 1.2–2.5 eV higher with respect to bulk O 1s is assigned to OH. The feature at 2.5–3.5 eV higher binding energy is assigned to H<sub>2</sub>O [48, 49]. Wang *et al.* [47], who recorded the O 1s core level of TiO<sub>2</sub> after both liquid and vapour exposure to water at room temperature, assigned a feature at 1.6 eV higher binding energy to OH species. More recently, Allegretti *et al.* [14] used photoelectron diffraction combined with SXPS to show that molecularly adsorbed water on TiO<sub>2</sub>(110) appears at 3.2–3.6 eV higher binding energy with respect to the bulk O 1s peak. Also according to Allegretti *et al.*, only molecularly adsorbed water should be stable on single crystal TiO<sub>2</sub>(110) at 190 K [14]. The exposure of TiO<sub>2</sub>(110) to ambient pressures of H<sub>2</sub>O gives rise two new peaks at 1.1–1.6 eV and 2.4–3.5 eV higher binding energies with respect to the bulk O 1s peak, assigned to hydroxyl groups at bridging oxygen rows and molecular water, respectively [18]. Taking the above into consideration,

it is reasonable to interpret the two adsorbate induced O 1s peaks in our spectra to the co-existence of surface hydroxyl and water molecules with an intensity ratio of about 4:1 respectively. It is possible that the hydroxyl component arises from reaction of H<sub>2</sub>O with the exposed wetting layer. It is worth noting that *ab initio* calculations predict the dissociation of H<sub>2</sub>O on anatase TiO<sub>2</sub>(001) for a H<sub>2</sub>O coverage less than 0.5 per Ti site and the co-existence of molecular and dissociated H<sub>2</sub>O with a 1:1 ratio for higher H<sub>2</sub>O coverage [50].

By increasing the H<sub>2</sub>O pressure to  $2 \times 10^{-6}$  mbar, we observe the hydroxylation of the thin film. A similar effect was observed for the single crystal TiO<sub>2</sub> surface by Bullock *et al.* [17]. Figure 4.8b depicts the O 1s spectrum after this high water pressure exposure. We notice a dramatic increase in the hydroxyl peak, along with the corresponding increase in the molecular water contribution. By looking into the attenuation of the O 1s peak due to the TiO<sub>2</sub> film, we estimate that the mixed water/hydroxyl overlayer has an average thickness of 0.6–3.5 Å. The intensity ratio of the OH to H<sub>2</sub>O components remains 4:1. Assuming that the the OH has a bond length of about 1 Å and that H<sub>2</sub>O has a height of about 1.5 Å, this gives an estimation of the coverage of the mixed overlayer being 0.5–3.2 ML. The greater width of the Gaussian contribution of the OH and H<sub>2</sub>O peaks can be attributed to the formation of a H-bonded structure. Alternatively, it could be due to occupation of additional adsorption sites, such as the step edges and the sides of the three-dimensional rutile rods. The presence of the O 1s contribution due to the TiO<sub>2</sub> film indicates that hydroxylation is not complete throughout the ultrathin film.

Finally, we annealed the hydroxylated film while monitoring the O 1s spectrum. We

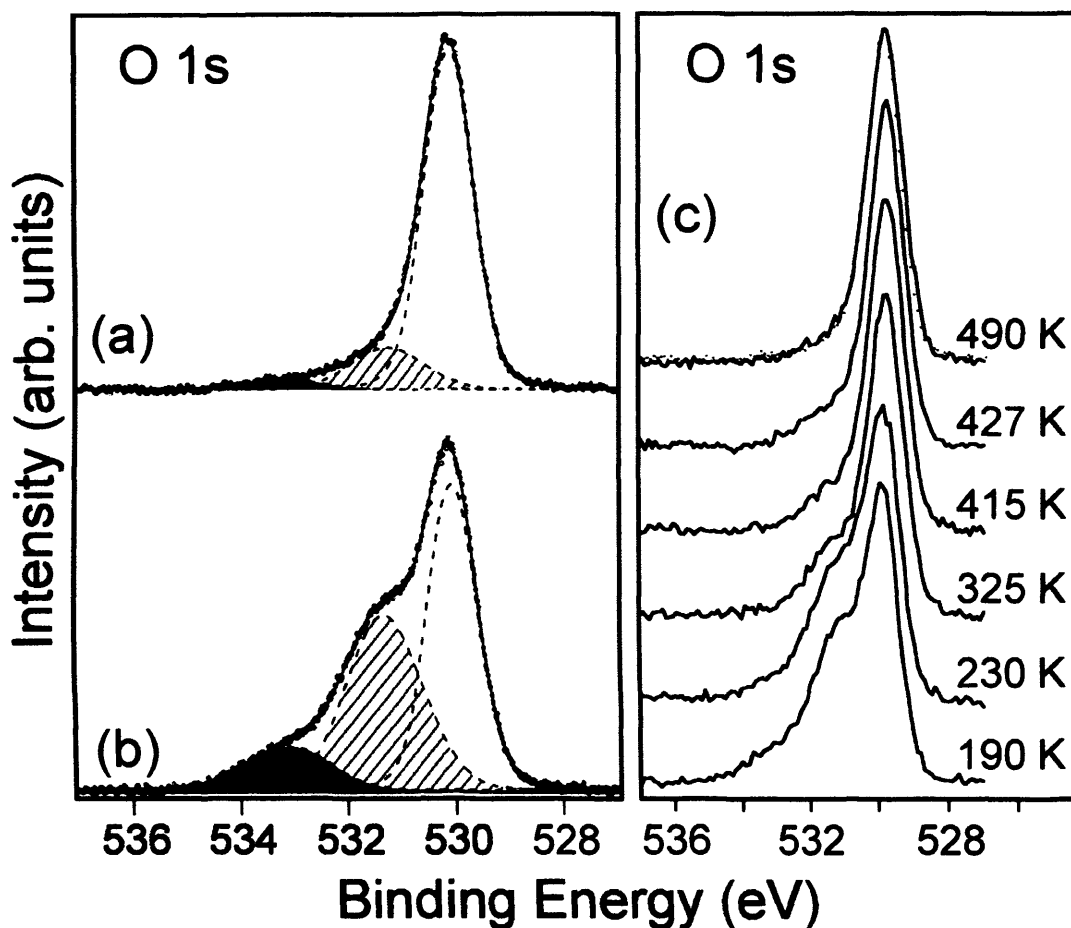


Figure 4.8: O 1s core level spectra ( $h\nu = 650$  eV) of the rutile ultrathin film (a) After 160 L exposure of  $\text{H}_2\text{O}$  recorded at 190 K. (b) After high pressure ( $2 \times 10^{-6}$  mbar)  $\text{H}_2\text{O}$  exposure recorded at 190 K. Circles, dashed lines and the solid line denote the data points, the different components of the fit and the sum of the components respectively. The background has been subtracted from the spectrum. The contribution of the molecular water on the spectrum is highlighted in grey at a shift of 3 eV from the O 1s bulk contribution. The contribution of hydroxyls is highlighted by diagonal lines at a shift of (a) 1.13 eV, (b) 1.27 eV from the O 1s bulk contribution. The FWHM of the Gaussian contribution to the components is 1 eV for the bulk, (a) 1.54 eV, (b) 1.59 eV for the OH and (a) 1.55 eV, (b) 1.63 eV for the  $\text{H}_2\text{O}$  contributions. All components have a Lorentzian contribution with FWHM of 0.14 eV. (c) Solid lines correspond to annealing after the high pressure  $\text{H}_2\text{O}$  exposure. The respective annealing temperatures are noted on their right. The red-dots correspond to the rutile film before exposure to  $\text{H}_2\text{O}$ ; it is displayed for comparison alongside the spectrum of the film annealed to 490 K.

observed that the adsorbate induced features gradually decrease until they are completely removed by annealing at  $490 \pm 15$  K (figure 4.8c). Hence we deduce that the hydroxylation process is reversible. The film was further annealed to 525 K, and subsequently cooled down to 190 K to confirm that there were no additional changes to the O 1s spectrum.

## 4.4 Conclusions

The growth of fully oxidised titanium films on the Ni(110) surface has been examined using core level SXPS and XANES. LEED was used to identify the films and link them to previous studies of this system. We confirm that these consist of a rutile  $\text{TiO}_2(110)$  film, as described by Ashworth *et al.* [9] and a quasi-hexagonal overlayer phase described in matrix notation by  $\begin{bmatrix} 2 & -6/7 \\ 0 & 12/7 \end{bmatrix}$ . We suggest that oxygen lies at the interface between the oxide and the metal based on the Ni  $2p_{3/2}$  core level spectra. We have also used XPS and XANES to follow the oxidation procedure and deduce that our films consist of fully oxidised titanium. By dosing water on to the rutile and wetting layer film at  $10^{-8}$  mbar, we observe the coadsorption of both molecular water and hydroxyl groups, with the appearance of two new features in the O 1s core level spectrum. Hydroxylation of the thin film is observed following exposure to  $10^{-6}$  mbar of  $\text{H}_2\text{O}$ . Finally, we show that the process of hydroxylation is reversible after annealing to 490 K.

# References

- [1] H.-J. Freund, H. Kuhlenbeck, and V. Staemmler, *Rep. Prog. Phys.* **59**, 283 (1996).
- [2] A. Atrei, U. Bardi, and G. Rovida, *Surf. Sci.* **391**, 216 (1997).
- [3] O. Dulub, W. Hebenstreit, and U. Diebold, *Phys. Rev. Lett.* **84**, 3646 (2000).
- [4] R. A. Bennett, C. L. Pang, N. Perkins, R. D. Smith, P. Morrall, R. I. Kvon, and M. Bowker, *J. Phys. Chem. B* **106**, 4688 (2002).
- [5] F. Sedona, G. A. Rizzi, S. Agnoli, F. X. Llabrés i Xamena, A. Papageorgiou, D. Ostermann, M. Sambì, P. Finetti, K. Schierbaum, and G. Granozzi, *J. Phys. Chem. B* **109**, 24411 (2005).
- [6] J. Schoiswohl, G. Tzvetkov, F. Pfuner, M. G. Ramsey, S. Surnev, and F. P. Netzer, *Phys. Chem. Chem. Phys.* **8**, 1614 (2006).
- [7] U. Diebold, *Surf. Sci. Rep.* **48**, 53 (2003).
- [8] Z. Chang and G. Thornton, *Surf. Sci.* **462**, 68 (2000).
- [9] T. V. Ashworth and G. Thornton, *Thin Solid Films* **400**, 43 (2001).

- [10] T. V. Ashworth, C. A. Muryn, and G. Thornton, *Nanotechnology* **16**, 3041 (2005).
- [11] P. J. D. Lindan and C. Zhang, *Phys. Rev. B* **72**, 75439 (2005).
- [12] M. A. Henderson, *Surf. Sci. Rep.* **46**, 1 (2002).
- [13] M. A. Henderson, *Surf. Sci.* **355**, 151 (1996).
- [14] F. Allegretti, S. O'Brien, M. Polcik, D. I. Sayago, and D. P. Woodruff, *Phys. Rev. Lett.* **95**, 226104 (2005).
- [15] O. Bikondoa, C. L. Pang, R. Ithnin, C. A. Muryn, H. Onishi, and G. Thornton, *Nat. Mater.* **5**, 189 (2006).
- [16] T. K. Sham and M.S. Lazarus, *Chem. Phys. Lett.* **68**, 426 (1979).
- [17] E. L. Bullock, L. Patthey, and S. G. Steinemann, *Surf. Sci.* **352**, 504 (1996).
- [18] G. Ketteler, S. Yamamoto, H. Bluhm, K. Andersson, D. E. Starr, D. F. Ogletree, H. Ogasawara, A. Nilsson, and M. Salmeron, *J. Phys. Chem. C* **111**, 8278 (2007).
- [19] R. Nyholm, J. N. Andersen, U. Johansson, B. N. Jensen, and I. Lindau, *Nucl. Instrum. Methods Phys. Res., Sect. A* **467**, 520 (2001).
- [20] S. Doniach and M. Šunjić, *J. Phys. C: Solid State Phys.* **3**, 285 (1970).
- [21] D. A. Shirley, *Phys. Rev. B* **5**, 4709 (1972).
- [22] J. Weissenrieder, A. Mikkelsen, J. N. Andersen, P. J. Feibelman, and G. Held, *Phys. Rev. Lett.* **93**, 196102 (2004).
- [23] L. Eierdal, F. Besenbacher, E. Lægsgaard, and I. Stensgaard, *Surf. Sci.* **312**, 31 (1994).



- [24] T. V. Ashworth, Ph.D. Thesis, University of Manchester, 2003.
- [25] T. Orzali, M. Casarin, G. Granozzi, M. Sami, and A. Vittadini, *Phys. Rev. Lett.* **97**, 156101 (2006).
- [26] J. Fink, Th. Müller-Heinzerling, B. Scheerer, W. Speier, F. U. Hillebrecht, J. C. Fuggle, J. Zaanen, and G. A. Sawatzky, *Phys. Rev. B* **32**, 4899 (1985).
- [27] V. S. Lusvardi, M. A. Barteau, J. G. Chen, J. Eng, Jr., B. Frühberger, and A. Teplyakov, *Surf. Sci.* **397**, 237 (1998).
- [28] T. Uozumi, K. Okada, A. Kotani, Y. Tezuka, and S. Shin, *J. Phys. Soc. Jpn.* **65**, 1150 (1996).
- [29] L. Soriano, M. Abbate, A. Fernández, A. R. González-Elipe, and J. M. Sanz, *Surf. Interface Anal.* **25**, 804 (1997).
- [30] G. van der Laan, *Phys. Rev. B* **41**, 12366 (1990).
- [31] M. Yoshiya, I. Tanaka, K. Kaneko, and H. Adachi, *J. Phys.: Condens. Matter.* **11**, 3217 (1999).
- [32] K. Okada and A. Kotani, *Journal Electron Spectrosc. Relat. Phenom.* **62**, 131 (1993).
- [33] S. O. Kucheyev, T. van Buuren, T. F. Baumann, J. H.; Satcher, Jr., T. M. Willey, R. W. Meulenberg, T. E. Felner, J. F. Poco, S. A. Gammon, and L. J. Terminello, *Phys. Rev. B* **69**, 245102 (2004).
- [34] S. Hüfner, *Photoelectron Spectroscopy*; 3rd ed.; Springer: Berlin, Germany, 2003.
- [35] G. van der Laan and B. T. Thole, *J. Phys.: Condens. Matter.* **4**, 4181 (1992).

- [36] M. A. van Veenendaal and G. A. Sawatzky, *Phys. Rev. Lett.* **70**, 2459 (1993).
- [37] P. R. Norton, R. L. Tapping, and J. W. Goodale, *Surf. Sci.* **65**, 13 (1977).
- [38] D. P. Woodruff and T. A. Delchar, *Modern Techniques of Surface Science*; 2nd ed.; Cambridge University Press: Cambridge, U.K., 1994.
- [39] NIST X-ray Photoelectron Spectroscopy Database; NIST Standard Reference Database 20, Version 3.4 (Web Version); <http://srdata.nist.gov/xps/>.
- [40] S. K. Sen, J. Riga, and J. Verbist, *Chem. Phys. Lett.* **39**, 560 (1976).
- [41] M. Oku, H. Matsuta, K. Wagatsuma, Y. Waseda, and S. Kohiki, *J. Electron Spectrosc. Relat. Phenom.* **105**, 211 (1999).
- [42] L. Leung, Ph.D. Thesis, University of Manchester, 2005.
- [43] S. Bartkowski, M. Neumann, E. Z. Kurmaev, V. V. Fedorenko, S. N. Shamin, V. M. Cherkashenko, S. N. Nemnonov, A. Winiarski, and D. C. Rubie, *Phys. Rev. B* **56**, 10656 (1997).
- [44] J. T. Mayer, U. Diebold, T. E. Madey, and E. Garfunkel, *J. Electron Spectrosc. Relat. Phenom.* **73**, 1 (1995).
- [45] J. Biener, E. Farfan-Arribas, M. Biener, C. M. Friend, and R. J. Madix, *J. Chem. Phys.* **123**, 094705 (2005).
- [46] J. Cardenas and S. Sjöberg, *Surf. Sci.* **532**, 1104 (2003).
- [47] L.-Q. Wang, D. R. Baer, M. H. Engelhard, and A. N. Shultz, *Surf. Sci.* **344**, 237 (1995).

- [48] T. Kendelewicz, P. Liu, C. S. Doyle, G. E. Brown, Jr., E. J. Nelson, and S. A. Chambers, *Surf. Sci.* **453**, 32 (2000).
- [49] P. Liu, T. Kendelewicz, G. E. Brown, Jr., E. J. Nelson, and S. A. Chambers, *Surf. Sci.*, **417**, 53 (1998).
- [50] A. Vittadini, A. Selloni, F. P. Rotzinger, and M. Grätzel, *Phys. Rev. Lett.* **81**, 2954 (1998).

## Chapter 5

# Reduced phases of $\text{TiO}_2(110)$ supported on $\text{Ni}(110)$

Reduced phases of ultrathin rutile  $\text{TiO}_2(110)$  grown on  $\text{Ni}(110)$  have been characterized with STM and low energy electron diffraction. Areas of  $1 \times 2$  reconstruction are observed as well as  $\{132\}$  and  $\{121\}$  families of crystallographic shear planes. These phases are assigned by comparison with analogous phases on native rutile  $\text{TiO}_2(110)$ .

### 5.1 Introduction

Ultrathin oxides grown on metallic substrates are currently a subject of intensive study in the emerging field of nanoscience. Possible applications include utilizing the self-assembled, low dimensional nanostructures in electronic devices, nanocatalysts and gas sensors. Controlling the oxidation state and the dimensions of these nanostructures may allow the

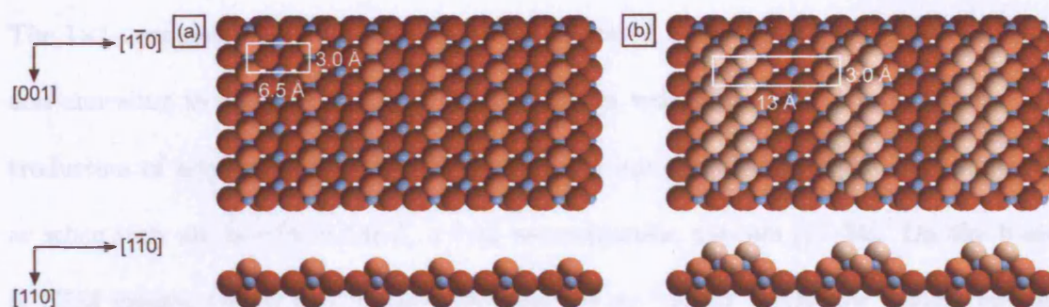


Figure 5.1: Atomic models of  $\text{TiO}_2(110)$  surfaces. The high symmetry axes and the surface unit cells are indicated. Small blue spheres represent Ti atoms and larger red spheres O atoms. O atoms nearer to the surface are shaded lighter. (a) The unreconstructed  $\text{TiO}_2(110)$   $1 \times 1$  surface. (b) The proposed added  $\text{Ti}_2\text{O}_3$ -row model for the  $\text{TiO}_2(110)$   $1 \times 2$  reconstruction [5].

production of a new range of technologically important materials.

The growth of titanium dioxide nanostructures grown on  $\text{Ni}(110)$  is discussed in the previous chapter [1–3]. It was shown that islands of rutile  $\text{TiO}_2(110)$  grow on top of a wetting layer that also has  $\text{TiO}_2$  stoichiometry. Rutile islands, with heights of up to 40 Å, typically grow on the  $\text{Ni}(110)$  single crystal with the  $\text{TiO}_2$   $[1\bar{1}0]$  azimuth parallel to the  $\text{Ni}$   $[001]$  direction. In addition, minority domains can be observed with the  $[001]$  direction of  $\text{TiO}_2(110)$  aligned parallel to the  $[001]$  direction of the substrate [4]. These islands are usually terminated by the unreconstructed  $\text{TiO}_2(110)$   $1 \times 1$  phase (figure 5.1a) and are referred to as ‘rutile islands’ in the rest of this chapter.

One of the key motivations for our current study is to establish to what extent the ultrathin titania mimics the behavior of the  $(110)$  surface of a rutile single crystal (henceforth referred to as the “native surface”). Differences might be expected because rutile  $\text{TiO}_2(110)$  is incommensurate with respect to the  $\text{Ni}(110)$  substrate.

The  $1\times 1$  terminated native surface is usually prepared by sputtering with inert gas ions and annealing to about 700-1200 K. This results in reduction of the crystal and the introduction of n-type conductivity. When samples are annealed to higher temperatures or when they are heavily reduced, a  $1\times 2$  reconstruction appears [15–24]. On the basis of STM images, Onishi and Iwasawa [5] proposed an “added  $\text{Ti}_2\text{O}_3$  row model” for the  $1\times 2$  reconstruction, shown in figure 5.1b. This model has been shown to be consistent with a range of experimental results, such as quantitative LEED, as well as theoretical calculations [5, 10].

Magnéli phases have also been observed on native surfaces, through the formation of crystallographic shear (CS) planes [7–9, 11, 13, 14, 16, 18]. A detailed review of CS plane formation in titanium oxides is given by Bursill and Hyde [20] and the energetics of this system have been studied by Catlow and James [24]. CS plane formation is caused by reduction of the crystal. As the concentration of oxygen vacancies increases, they order into specific planes, resulting in the collapse of the crystal by a slip of half a unit cell along the CS planes. Arrays of (132) CS planes terminated at the  $\text{TiO}_2(110)$  surface are shown in figure 5.2. Two different arrangements of these CS planes are illustrated.

The first arrangement consists of half-height steps where alternate CS planes slip half a unit cell up then down. We refer to these as “up-down” steps. In the second arrangement all CS planes slip in the same direction, and we refer to this as a “staircase” arrangement of steps. In the up-down steps, the CS planes can be thought of as pairs comprising the up step and the down step.

The orientations of the CS planes reported in [20] are described by the empirical formula



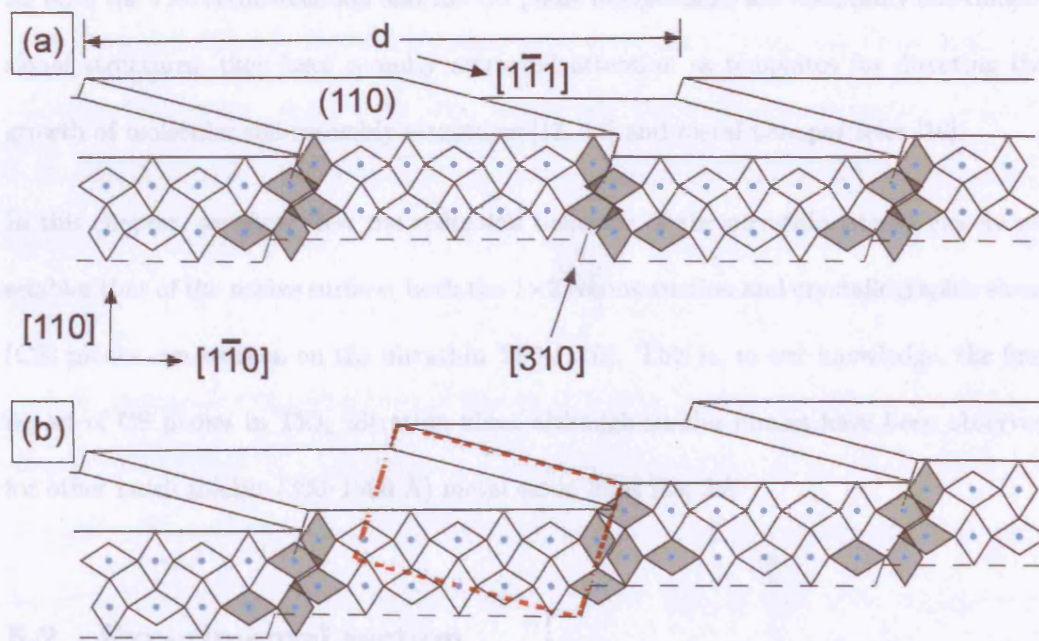


Figure 5.2: Schematic representation of crystallographic shear planes intersecting the  $\text{TiO}_2(110)$  surface. Blue circles represent Ti atoms and rhombi are the cross sections of Ti atoms in pseudo-octahedral co-ordination. Cross sections represent a cut parallel to the (001) plane. CS planes of (132) orientation are indicated by dotted lines intersecting the (001) plane along the [310] direction and by solid lines intersecting the (110) plane along the  $[1\bar{1}1]$  direction. One of these CS planes is highlighted with a red dashed perimeter. The rhombi which form the CS planes are shaded gray. The CS planes induce half-height steps at the  $\text{TiO}_2(110)$  surface resulting in (a) an “up-down” half-height step arrangement and (b) a “staircase” half-height step arrangement. The periodicity between the up-down pairs,  $d$ , is indicated.

$(hkl) = p(121) + q(011)$ , where  $p$  and  $q$  are integers. When  $p/q \geq 1$ , which is the case in the measurements reported by Bursill and Hyde [20], the solutions to the empirical formula correspond to orientations of the CS planes between (132) and (121).

As both the  $1 \times 2$  reconstruction and the CS plane intersections are essentially one-dimensional structures, they have recently attracted attention as templates for directing the growth of molecular self-assembly structures [13, 14] and metal nanoparticles [16].

In this chapter, we show that the reduction behavior of the ultrathin titania closely resembles that of the native surface; both the  $1 \times 2$  reconstruction and crystallographic shear (CS) planes can be seen on the ultrathin  $\text{TiO}_2(110)$ . This is, to our knowledge, the first report of CS planes in  $\text{TiO}_2$  ultrathin films, although similar phases have been observed for other much thicker (300–1000 Å) metal oxide films [25, 26].

## 5.2 Experimental section

STM experiments were carried out in two separate ultra-high vacuum (UHV) chambers. The  $1 \times 2$ -terminated rutile  $\text{TiO}_2(110)$  islands were imaged using the *Omicron* LT-STM operated at  $77 \pm 1$  K, with a base pressure of  $7 \times 10^{-11}$  mbar. The CS plane surfaces were characterized using the *Omicron* VT-STM operated at room temperature and a base pressure of  $2 \times 10^{-10}$  mbar.

The substrate was a single crystal of  $\text{Ni}(110)$ , prepared with cycles of  $\text{Ar}^+$  sputtering and vacuum annealing to 1100 K. The cleanliness of the  $\text{Ni}(110)$  surface was established from sharp  $(1 \times 1)$  LEED patterns and the absence of any contaminants in Auger electron



spectra (AES). The  $\text{TiO}_2(110)$  islands were grown on  $\text{Ni}(110)$  by first depositing Ti by metal vapor deposition (MVD) at room temperature and then oxidising for 30 min in a pressure of  $1 \times 10^{-7}$  mbar molecular oxygen at a temperature between 873 and 1023 K. The coverage of titanium metal was estimated from AES to be in the range of 2-4 monolayer equivalents (MLE, where 1 MLE corresponds to a coverage of one adsorbate atom per substrate surface unit cell). After oxidising, rutile  $\text{TiO}_2(110)$  islands are formed with a thickness between 1 and 4 atomic layers, as measured directly with STM. The rutile islands sit on top of an initial wetting layer that is two layers thick. More details of the rutile islands and the wetting layer can be found elsewhere [1-3].

Crystallographically sheared ultrathin films of  $\text{TiO}_2$  have been formed from these  $\text{Ni}(110)$ -supported  $\text{TiO}_2(110)$   $1 \times 1$  islands by further annealing at 1110 K for 15 min in a pressure of  $1 \times 10^{-7}$  mbar  $\text{O}_2$ . Similar CS planes could also be formed in the  $\text{TiO}_2(110)$  ultrathin films by directly annealing the as-deposited Ti to 1100 K for 30 min under a pressure of  $1 \times 10^{-7}$  mbar  $\text{O}_2$ . STM images were processed using Image SXM v1.8127. The thickness of the sheared film (4 layers on average) was evaluated from AES in combination with STM measurements of the density and heights of the initially formed rutile islands.

## 5.3 Results and discussion

### 5.3.1 The $1 \times 2$ reconstruction

Although the rutile islands are often terminated by the  $1 \times 1$  phase, more reduced islands are also found. Figure 5.3 shows STM images of some islands terminated by the  $\text{TiO}_2(110)$

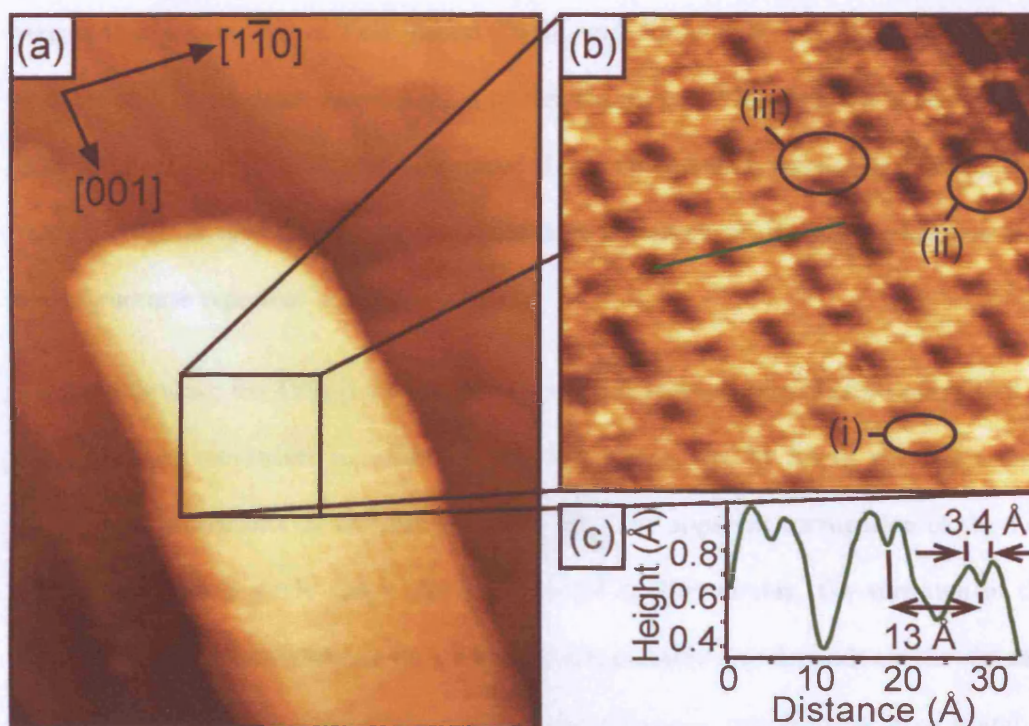


Figure 5.3: STM images of TiO<sub>2</sub> islands with a  $1 \times 2$  termination. (a) Large scale ( $350 \times 470 \text{ \AA}^2$ , 1.05 V, 3.44 nA) image. The axes mark the orientation of TiO<sub>2</sub>(110). (b) High resolution smoothed image ( $90 \times 90 \text{ \AA}^2$ , 1.00 V, 1.00 nA). A single link (i), a cross-link (ii), and a rosette-link (iii) are indicated. (c) Line profile along the line drawn in (b).

$1 \times 2$  reconstruction. The islands are typically 1-4 atomic layers thick.

The high resolution image in figure 5.3b shows a large density of links present. These links are in the form of cross-links, as well as single links and (elongated) rosette structures. For more reduced  $1 \times 2$  surfaces, STM images of the native surface show the formation of similar links between  $1 \times 2$  rows [7-9, 11, 13, 14, 16, 18]. They are known to be mobile upon annealing and to form cross and rosette shapes as well as single links.

Two feasible models have been proposed recently for these links. Bowker *et al.* [7, 9]

suggest that a new type of  $1 \times 2$  “added  $\text{Ti}_3\text{O}_6$  row” forms and that these rows contain links between them. More recently [8], a model was proposed for the links which is based on the original added- $\text{Ti}_2\text{O}_3$  model described above. At present it has not been established whether either of these interpretations of the links is correct but there is a consensus that these structures represent a reduced phase.

A line profile along the  $\text{TiO}_2$   $[\bar{1}\bar{1}0]$  direction (figure 5.3c) reveals periodic rows every 13.0 Å. These rows are themselves composed of two ridges, separated by 3.4 Å, which is a close match to measurements on the native surface [8]. The apparent corrugation of the  $1 \times 2$  rows in the present study ranges between 0.5–1.7 Å. Presumably, the variation in the corrugation arises from differing tip conditions and possibly also depends on the distance of the  $\text{TiO}_2$  surface from the conducting metallic substrate, which varies from island to island.

No areas of the  $\text{TiO}_2(110)$   $1 \times 2$  reconstruction were detected after further annealing of such surfaces to 773 K in  $1 \times 10^{-7}$  mbar  $\text{O}_2$ , suggesting that the  $\text{TiO}_2$  stoichiometry can be restored by further oxidation. This implies that the  $1 \times 2$  reconstruction is caused by incomplete oxidation of the as-deposited Ti.

### 5.3.2 The crystallographic shear planes

The LEED pattern of the supported titania following annealing to 1110 K is shown in figure 5.4 together with a schematic diagram of the pattern. Discrete spots are observed running along  $\langle 1\bar{1}2 \rangle$  and  $\langle \bar{1}12 \rangle$ . These spots will be referred to as “ $\langle 112 \rangle$ ” spots. The  $\langle 112 \rangle$  spots have a periodicity of about 1/16 of the  $[1\bar{1}2]$  (or  $[\bar{1}12]$ ) unit vector.

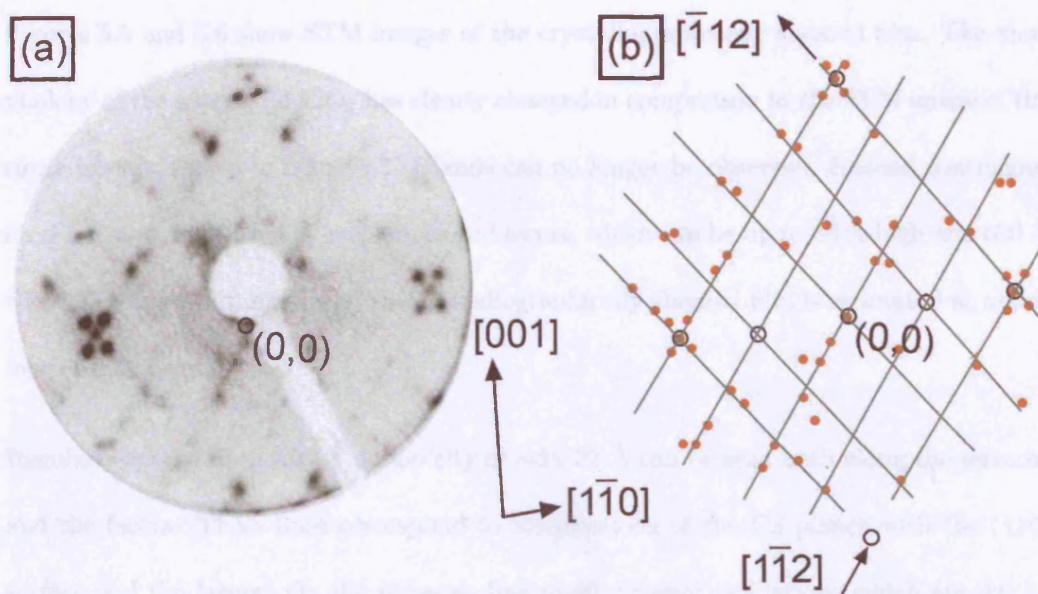


Figure 5.4: (a) LEED pattern (32 eV; negative image) of the crystallographically sheared film. The orientation of TiO<sub>2</sub>(110) is indicated. (b) Schematic diagram of (a) drawn to scale. Filled red circles depict the spots present in the LEED pattern. Open circles show the positions of the LEED beams from the TiO<sub>2</sub>(110) 1×1 termination. The zero order spot is labelled. The lines indicate the principal directions of the streaking in the LEED pattern with respect to the TiO<sub>2</sub>(110) surface unit cell.

This corresponds to a real space distance of  $\sim 35$  Å, which matches the periodicity of the CS plane up-down pairs observed in our STM images (discussed later) and those taken from the crystallographically sheared native surface [15].

By considering symmetrically equivalent CS planes, Bennett *et al.* [15] deduce that a CS plane of the  $\{hkl\}$  family intersects the (110) plane along  $\langle p+q \overline{p+q} 3p+q \rangle$  and  $\langle \overline{p+q} p+q 3p+q \rangle$ . The  $\langle 112 \rangle$  LEED spots described above are therefore consistent with the  $\{132\}$  family of CS planes. In addition, all CS planes intersect the (110) plane along  $\langle 1\bar{1}1 \rangle$  and  $\langle \bar{1}11 \rangle$ , and intersection lines should therefore be observable in STM images oriented at  $\pm 65.5^\circ$  with respect to the TiO<sub>2</sub> [001] azimuth.



Figures 5.5 and 5.6 show STM images of the crystallographically sheared film. The morphology of the supported  $\text{TiO}_2$  has clearly changed in comparison to the STM image of the rutile islands, shown in figure 5.3. Islands can no longer be observed. Instead continuous films are seen, separated by step edges and facets, which can be up to 50 Å high and 600 Å wide. The average thickness of the crystallographically sheared film is estimated at about four atomic layers.

Regularly spaced lines with a periodicity of  $\sim 34\text{--}35$  Å can be seen both along the terraces and the facets. These lines correspond to intersections of the CS planes with the (110) surface and the facets. On the terraces, line profiles reveal oscillations which are due to an up-down arrangement of CS planes. The periodicity of the up-down pairs is within the range observed for the crystallographically sheared native surface [15, 21] and also consistent with the LEED pattern discussed above.

The line profile displayed in figure 5.5c shows that the corrugation of the up-down steps is  $\sim 1$  Å, which is slightly lower than expected for half-steps (1.6 Å). The discrepancy can be explained by the finite size of the tip preventing it from reaching the bottom of the “down” terraces. When this steric restriction of the tip is absent, for example when there is a half-step leading onto a flat terrace, the apparent height increases to about  $\sim 1.3$  Å. Furthermore, in higher resolution images, we measure the corrugation of the up-down steps in a range from 1.2–1.5 Å. These latter values are in good agreement with the ideal half-height step of 1.6 Å.

An interesting feature of the images in figure 5.5 and 5.6 concerns the step edges. All the step edges are incorporated into the CS shear planes. This is indicated by their alignment

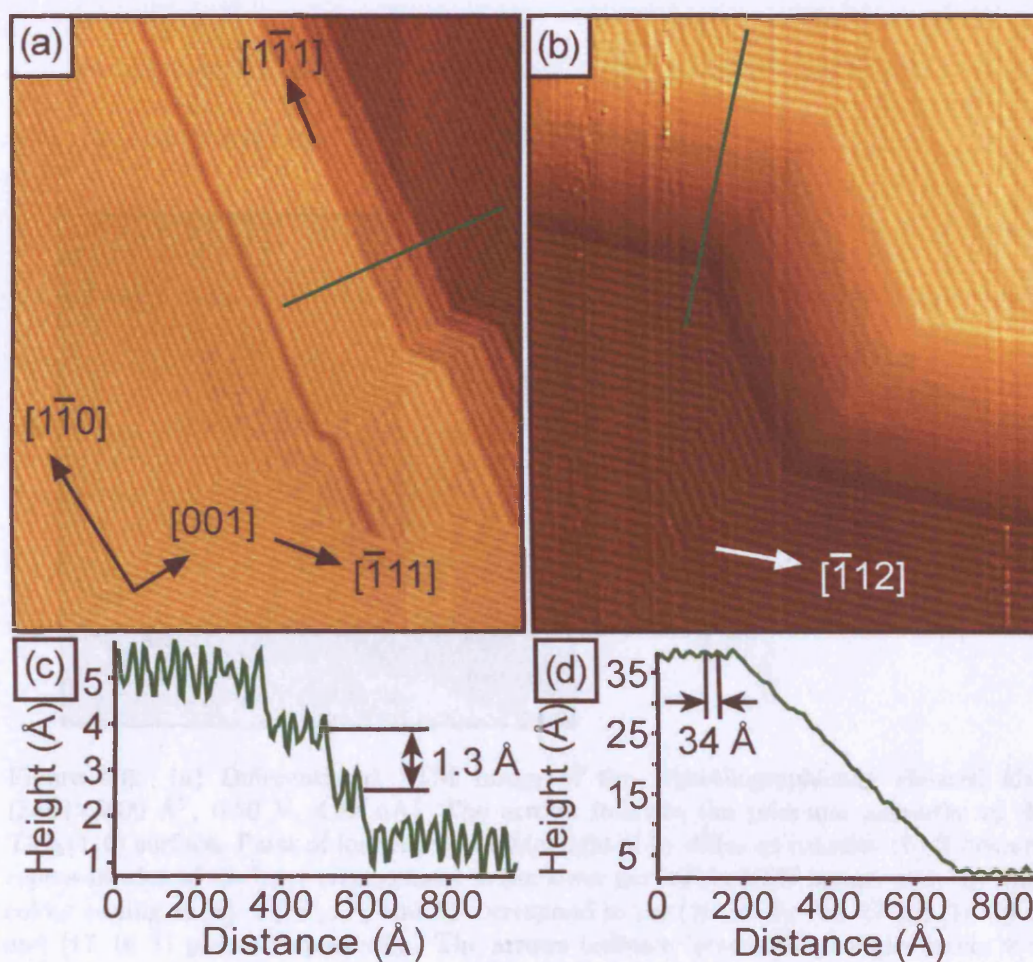


Figure 5.5: STM images of the crystallographically sheared film. (a) ( $1700 \times 2100 \text{ \AA}^2$ , 0.30 V, 0.90 nA). (b) ( $1500 \times 1800 \text{ \AA}^2$ , 0.15 V, 0.80 nA). The arrows indicate both the principal azimuths of the  $\text{TiO}_2(110)$  surface and the directions of the CS plane intersections at the (110) surface. (c) Line profile along the line indicated in (a). (d) Line profile along the line indicated in (b). The image in (b) has a shadow effect applied and the line profile in (d) is taken from an image without the shadow applied.

parallel to the CS planes and their height ( $\approx 2-3 \text{ \AA}$ ) which correspond to half steps. Bruchner et al. [15] suggest that step edges would be incorporated into CS planes so that the surface free energy can be reduced by approximately  $\sim 1.5 \text{ \AA}$  instead of the natural  $3.25 \text{ \AA}$  step. Some of the images of the native surface presented by Bruchner et al. [15] show the incorporation of step edges with the CS planes.

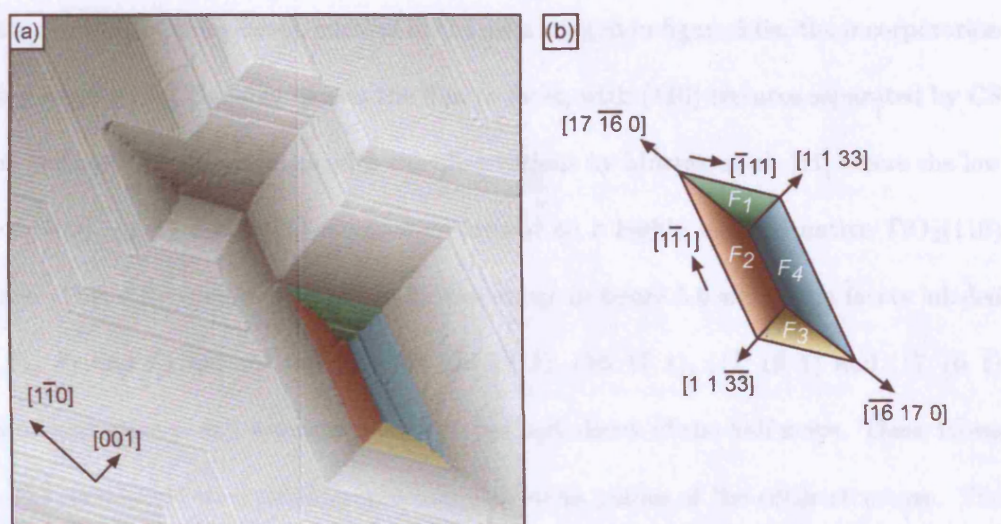


Figure 5.6: (a) Differentiated STM image of the crystallographically sheared film. ( $3600 \times 3600 \text{ \AA}^2$ ,  $0.50 \text{ V}$ ,  $4.82 \text{ nA}$ ). The arrows indicate the principal azimuths of the  $\text{TiO}_2(110)$  surface. Parts of four facets are highlighted by different colours. (b) Schematic representation of the facet arrangement in the lower part of the STM image, with the same colour coding as (a).  $F_1$ ,  $F_2$ ,  $F_3$  and  $F_4$  correspond to the  $(16\ 17\ \bar{1})$ ,  $(16\ 17\ 1)$ ,  $(17\ 16\ 1)$  and  $(17\ 16\ \bar{1})$  planes respectively. The arrows indicate intersections of the facets with each other and with the  $(110)$  plane.

parallel to the CS planes and their heights (1.2–1.5 Å) which correspond to half steps. Bennett *et al.* [15] suggest that step edges would be incorporated into CS planes so that the surface free energy can be reduced by exposing steps of  $\sim 1.6$  Å instead of the natural 3.25 Å steps. Some of the images of the native surface presented by Bennett *et al.* [15] show this incorporation of step edges with the CS planes.

Further to this, in many cases, such as in the area imaged in figure 5.6a, the incorporation of step edges with CS planes causes the film to facet, with (110) terraces separated by CS plane half steps. This contrasts with the observations by Murray *et al.* [11] where the low index {100}, {111} and {011} facets were formed on a highly reduced native TiO<sub>2</sub>(110) surface. This difference is exemplified by the image in figure 5.6 where the facets labeled  $F_1$ ,  $F_2$ ,  $F_3$  and  $F_4$  are measured as the  $(16\ 17\ \bar{1})$ ,  $(16\ 17\ 1)$ ,  $(17\ 16\ 1)$  and  $(17\ 16\ \bar{1})$  planes, respectively, and are determined by the periodicity of the half steps. These facets ( $F_1$ – $F_4$ ) correspond to crystallographically equivalent planes of the rutile structure. The dihedral angle between these facets and the (110) plane is  $3.0^\circ$ , a close match to the  $3.7^\circ$  measured directly from the STM image in figure 5.6a. The arrangement of the facets pictured in figure 5.6 gives the appearance of oblique wedge-like indentations in the (110) surface.

Such well-defined, wedge-like facets were not observed for the crystallographically sheared native surface. Instead, poorly defined, large-scale faceting was observed in STM and this was presumed to give the crystal a rippled appearance when viewed by eye [15].

A number of the CS planes identified in our STM images were not detected with LEED. This is presumably due to the LEED measurements sampling a different area to the STM.



In particular, numerous CS plane intersections are observed in STM images running along  $[\bar{1}\bar{1}1]$ ,  $[\bar{1}11]$  and  $[\bar{1}\bar{1}3]$ , the last being indicative of the formation of CS planes of the  $\{121\}$  family.

Figure 5.7a shows a high resolution image of a CS plane structure. Here, lines of the CS plane intersections run parallel to the  $[\bar{1}\bar{1}3]$  direction, caused by the  $\{121\}$  family of CS planes. The CS plane intersections lead to an up-down arrangement of half-height steps, as discussed previously. The line profile in figure 5.7d highlights these up-down steps.

Additional fine structure can be seen in the image, consisting of lines which run in the  $[001]$  direction. The separation of these lines along  $[\bar{1}\bar{1}0]$  is about 6.5 Å as shown in the line profile of figure 5.7c, indicating that they correspond to the  $1\times 1$  rows of the  $\text{TiO}_2(110)$  surface. The dashed guideline in figure 5.7a is drawn over one of these finer lines. It can be seen that the lines stay in-phase across the half steps. On the native  $\text{TiO}_2(110)$  surface, STM images reveal  $1\times 1$  rows, which are displaced laterally by half a unit cell in the  $[\bar{1}\bar{1}0]$  direction as a single step is crossed [6]. That there is no phase-shift in the  $1\times 1$  rows in figure 5.7 provides further evidence that the steps are indeed genuine CS plane derived half steps.

Figure 5.7b shows a fast Fourier transform (FFT) of the STM image in figure 5.7a. The FFT image detects the series of CS plane up-down pairs as an array of spots. The direction in which the spots align corresponds to the direction across which the half steps run and the periodicity of the spots matches the separation between pairs of up-down steps and therefore supports our assignment of the analogous LEED  $\langle 112 \rangle$  spots to periodic CS plane up-down pairs.

## 5.1 Conclusions

Figure 5.7: (a) STM image of the crystallographically sheared film. (360×180 Å<sup>2</sup>, 0.15 V, 0.85 nA). The arrows indicate both the principal azimuths of the TiO<sub>2</sub>(110) surface and the direction of the CS plane intersections. A dashed guideline shows that the TiO<sub>2</sub>(110) 1×1 rows are in-phase across the half steps. Note that the image in this figure is taken from one of the minority islands with the TiO<sub>2</sub> [001] azimuth oriented parallel to the Ni [001] direction. Similar images were observed on the majority islands where the TiO<sub>2</sub> [1 $\bar{1}$ 0] azimuth lies parallel to Ni [001]. (b) Fast Fourier transform of the STM image presented in (a). Blue arrows pointing to the right indicate discrete spots arising due to the periodicity of the CS plane up-down pairs and red arrows pointing to the left indicate the (01) and (0 $\bar{1}$ ) spots of TiO<sub>2</sub>(110). An open yellow circle highlights the (00) spot. (c)-(d) Line profiles along the lines indicated in (a).

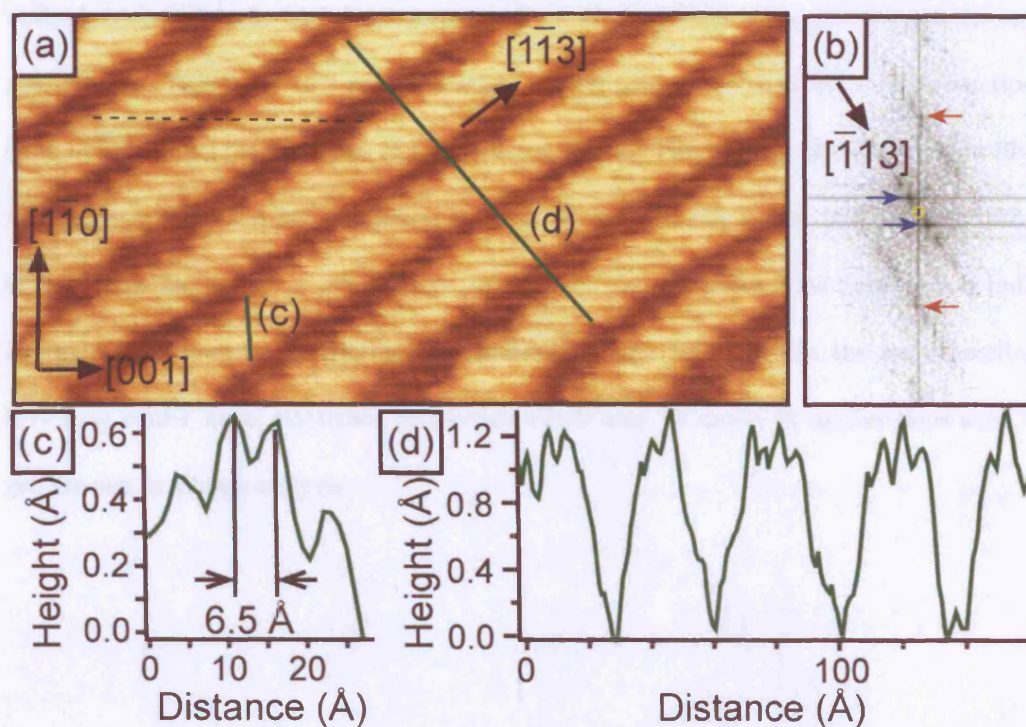


Figure 5.7: (a) STM image of the crystallographically sheared film. (360×180 Å<sup>2</sup>, 0.15 V, 0.85 nA). The arrows indicate both the principal azimuths of the TiO<sub>2</sub>(110) surface and the direction of the CS plane intersections. A dashed guideline shows that the TiO<sub>2</sub>(110) 1×1 rows are in-phase across the half steps. Note that the image in this figure is taken from one of the minority islands with the TiO<sub>2</sub> [001] azimuth oriented parallel to the Ni [001] direction. Similar images were observed on the majority islands where the TiO<sub>2</sub> [1 $\bar{1}$ 0] azimuth lies parallel to Ni [001]. (b) Fast Fourier transform of the STM image presented in (a). Blue arrows pointing to the right indicate discrete spots arising due to the periodicity of the CS plane up-down pairs and red arrows pointing to the left indicate the (01) and (0 $\bar{1}$ ) spots of TiO<sub>2</sub>(110). An open yellow circle highlights the (00) spot. (c)-(d) Line profiles along the lines indicated in (a).

## 5.4 Conclusions

In conclusion, we have reported the reduction of Ni(110)-supported TiO<sub>2</sub>(110) which form bulk-like reduced rutile TiO<sub>2</sub>(110) structures. STM images show the presence of the oxygen deficient TiO<sub>2</sub>(110) 1×2 reconstruction. Furthermore, we observed the intersections of the {132} and {121} families of CS planes with the (110) surface of the ultrathin film, as previously reported for the native surface. As the CS planes are bulk defects rather than surface defects we conclude that structurally, the ultrathin films behave in a bulk-like manner. However, restricting the thickness of the TiO<sub>2</sub>(110) in the way described here may confer novel electronic properties which may be useful in applications such as gas-sensing or photocatalysis.

# References

- [1] T. V. Ashworth and G. Thornton, *Thin Solid Films* **400**, 43 (2001).
- [2] T. V. Ashworth, C. A. Muryn, and G. Thornton, *Nanotechnology* **16**, 3041 (2005).
- [3] A. C. Papageorgiou, G. Cabailh, Q. Chen, A. Resta, E. Lundgren, J. N. Andersen, and G. Thornton, *J. Phys. Chem. C* **111**, 7704 (2007).
- [4] T. V. Ashworth, Ph.D. thesis, University of Manchester (2003).
- [5] H. Onishi and Y. Iwasawa, *Surf. Sci.* **313**, L783 (1994).
- [6] U. Diebold, *Surf. Sci. Rep.* **48**, 53 (2003).
- [7] P. Stone, R. A. Bennett, and M. Bowker, *New J. Phys.* **1**, 8 (1999).
- [8] S. Takakusagi, K. Fukui, F. Nariyuki, and Y. Iwasawa, *Surf. Sci.* **523**, L41 (2003).
- [9] R. A. Bennett, P. Stone, N. J. Price, and M. Bowker, *Phys. Rev. Lett.* **82**, 3831 (1999).
- [10] M. Blanco-Rey, J. Abad, C. Rogero, J. Mendez, M. F. Lopez, J. A. Martin-Gago, and P. L. de Andres, *Phys. Rev. Lett.* **96**, 055502 (2006).
- [11] P. W. Murray, N. G. Condon, and G. Thornton, *Phys. Rev. B* **51**, 10989 (1995).

- [12] C. L. Pang, S. A. Haycock, H. Raza, P. W. Murray, G. Thornton, O. Gülseren, R. James, and D. W. Bullett, *Phys. Rev. B* **58**, 1586 (1998).
- [13] K. Fukui and M. Sakai, *Jpn. J. Appl. Phys., Part 1* **45**, 2063 (2006).
- [14] Y. Wang, Y. Ye, and K. Wu, *J. Phys. Chem. C* **110**, 17960 (2006).
- [15] R. A. Bennett, S. Poulston, P. Stone, and M. Bowker, *Phys. Rev. B* **59**, 10341 (1999).
- [16] R. A. Bennett, M. A. Newton, R. D. Smith, J. Evans, and M. Bowker, *Mater. Sci. Technol.* **18**, 710 (2002).
- [17] A. Berkó and F. Solymosi, *Langmuir* **12**, 1257 (1996).
- [18] R. A. Bennett, *PhysChemComm* **3**, 9 (2003).
- [19] K. F. McCarty and N. C. Bartelt, *Surf. Sci.* **527**, L203 (2003).
- [20] L. A. Bursill and B. G. Hyde, *Prog. Solid State Chem.* **7**, 177 (1972).
- [21] H. Nörenberg and G. A. D. Briggs, *Surf. Sci.* **402**, 738 (1998).
- [22] H. Nörenberg, R. E. Tanner, K. D. Schierbaum, S. Fischer, and G. A. D. Briggs, *Surf. Sci.* **396**, 52 (1998).
- [23] G. S. Rohrer, V. E. Henrich, and D. A. Bonnell, *Science* **250**, 1239 (1990).
- [24] C. R. A. Catlow and R. James, *Proc. R. Soc. Lond. A* **384**, 157 (1982).
- [25] M. Li, E. I. Altman, A. Posadas, and C. H. Ahn, *Thin Solid Films* **446**, 238 (2004).
- [26] W. Gao and E. I. Altman, *Surf. Sci.* **600**, 2572 (2006).
- [27] S. Barrett, ImageSxM (2006), URL: <http://www.liv.ac.uk/sdb/ImageSXM/>.

## Chapter 6

# Tracking the reaction of O<sub>2</sub> and surface hydroxyl on TiO<sub>2</sub>(110) with STM

In this chapter, the reaction of molecular oxygen with the hydroxylated TiO<sub>2</sub>(110) surface is addressed. TiO<sub>2</sub>(110) surfaces before and after reaction with molecular oxygen at room temperature are directly visualised. After the reaction with oxygen, mobile reaction products with different apparent heights can be found on the surface, at the expense of the surface hydroxyl.

## 6.1 Introduction

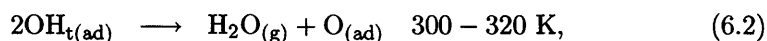
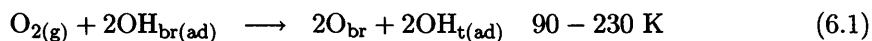
Titanium dioxide is a versatile material of particular interest due to its photocatalytic properties and its role in heterogeneous catalysis [1]. Oxygen plays an important role in such TiO<sub>2</sub>-based photocatalysts because it is known to act as an electron scavenger [2, 3]. As the TiO<sub>2</sub> will nearly always be exposed to water in any technological applications, it is important to consider the reaction of oxygen with water on TiO<sub>2</sub>. This mechanism is not yet fully elucidated and it is therefore of current interest to determine and understand it [4, 5]. Here we model this reaction in UHV by studying the interaction of molecular oxygen with hydroxyl groups on the rutile TiO<sub>2</sub>(110) surface. Using STM, oxygen is shown to react with the surface hydroxyl, leaving adsorbed O adatoms at the surface.

Such a relatively complex reaction can be addressed because of recent advances in the understanding of STM images of TiO<sub>2</sub>(110) surfaces. Crucially, oxygen vacancies ( $O_{vac}$ ) and bridging hydroxyl groups ( $OH_{br}$ ) have been unambiguously identified [6–9].  $O_{vac}$  are created during the sputter/anneal preparation of the surface and hydroxyl groups result from the dissociation of water in these  $O_{vac}$  [6–9]. The source of water is the residual vacuum and each molecule that dissociates gives two  $OH_{br}$ .

The interaction of O<sub>2</sub> with a TiO<sub>2</sub>(110) surface containing  $O_{vac}$  is also fairly well understood [6, 10–15]. Temperature programmed desorption (TPD) and electron energy loss spectroscopy (EELS) [10, 11] experiments suggest that O<sub>2</sub> adsorption at low temperature on the surface results in three O<sub>2</sub>-adsorbates per oxygen vacancy site. Two of these three O<sub>2</sub>-adsorbates are stable on the surface up to 410 K, at which point they desorb as O<sub>2</sub>, in general agreement with the stability of O<sub>2</sub> observed via electron paramagnetic resonance

(EPR) [16]. The formation of these adsorbates on  $\text{TiO}_2(110)$  has also been modelled using periodic *ab initio* Hartree-Fock calculations [12, 13]. The remaining adsorbed  $\text{O}_2$  dissociates irreversibly in the  $\text{O}_{\text{vac}}$  of the surface as the temperature rises towards 150–200 K [10]. This results in the vacancy being filled, together with the adsorption of an oxygen adatom on an adjacent  $\text{Ti}_{5c}$  [10, 14, 15]. The irreversible dissociation is the only adsorption pathway for  $\text{O}_2$  on  $\text{TiO}_2(110)$  at temperatures greater than 150–200 K [10]. Recently, this dissociation mechanism has been directly observed with STM [6].

The reaction of  $\text{O}_2$  with hydroxylated  $\text{TiO}_2(110)$  has previously been studied with high resolution electron energy loss spectroscopy (HREELS) and TPD [2]. The TPD results show  $\text{H}_2\text{O}$  desorption peaks at 300 K due to the interaction of molecular oxygen with the surface hydroxyl. A mechanism was proposed for this reaction which is summarised below:

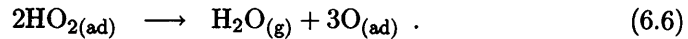
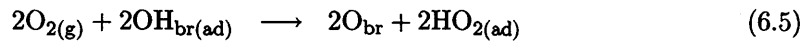
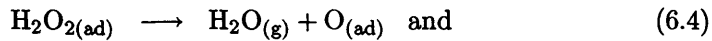
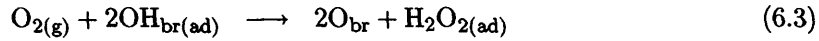


where the subscripts ‘ad’ and ‘g’ refer to ‘adsorbate’ and ‘gas phase’, respectively.  $\text{OH}_{\text{t}}$  indicates a terminal hydroxyl, co-ordinated to a  $\text{Ti}_{5c}$  atom via its O atom, and  $\text{O}_{\text{br}}$  is the bridging oxygen atom left on the surface where the reacting  $\text{OH}_{\text{br}(\text{ad})}$  previously resided.

Further insight into this reaction mechanism is given by *ab initio* and molecular dynamics calculations of the  $\text{OH}/\text{TiO}_2(110)$  system [3, 17, 18]. Liu *et al.* have made predictions of the interaction of  $\text{OH}_{\text{br}}$  with molecular  $\text{O}_2$  on  $\text{Ti}_{5c}$  [3]. Their first principles calculations suggest that  $\text{OH}_{\text{br}}$  groups can facilitate  $\text{O}_2$  adsorption on  $\text{TiO}_2$  by donating electrons to the  $\text{O}_2$  via  $\text{Ti}_{5c}$ . They also predict that  $\text{O}_2$  can diffuse along the channels of  $\text{Ti}_{5c}$  atoms



on  $\text{TiO}_2(110)$ . In other work, Tilocca *et al.* employed both DFT and molecular dynamics calculations, showing that metastable peroxy and superoxy species could form following exposure of  $\text{O}_2$  to hydroxylated  $\text{TiO}_2(110)$ . For the 8 ps molecular dynamics trajectory simulated, both peroxy and superoxy were found to be stable. Hence it was suggested that the metastable species could decompose directly to form gas phase water and adsorbed oxygen adatoms without going through a  $\text{Ti-OH}_t$  phase [17]. These alternative reaction mechanisms are summarised below:



The calculations described above face limitations associated with the use of the Perdew-Burke-Ernzerhof (PBE) functional [19], which underestimates the band gap of  $\text{TiO}_2$  in electronic structure calculations. More recent calculations by Di Valentin *et al.* [18], which employ hybrid DFT, have a better agreement with experimental observations, giving a band gap closer to the experimental value. Localised band gap defect states associated with  $\text{O}_{\text{vac}}$  are predicted, as expected from photoelectron spectroscopy results [20]. These

latter calculations also show that band gap states remain even following H<sub>2</sub>O dissociation, indicating that OH<sub>br(ad)</sub> act as e<sup>-</sup> traps.

## 6.2 Experimental section

The measurements were performed using the VT-STM described in section 2.1, operating at a base pressure of  $2 \times 10^{-10}$  mbar. The TiO<sub>2</sub>(110) surface of a single crystal was prepared using cycles of Ar<sup>+</sup> ion bombardment and UHV annealing. This procedure leads to well-ordered and contaminant-free (1×1) surfaces as judged by LEED, AES and STM. Such surfaces typically contain 4–10% ML of O<sub>vac</sub>, where 1 ML corresponds to the density of primitive surface unit cells. All STM images in this chapter were recorded at room temperature with a positive sample bias, which corresponds to tunnelling into empty sample states. The bias ranges from 0.7–1.5 V and the tunnelling current from 0.2–1.0 nA.

As detailed in [6], hydroxylation of the surface was achieved either by allowing the sample to cool down in distilled water vapour ( $3 \times 10^{-9}$  mbar) or by dosing water from the residual vacuum. The most prevalent gases in the residual vacuum are H<sub>2</sub>O, CO, CO<sub>2</sub> and H<sub>2</sub>. Of these gases, according to STM tests, only water reacts with the surface at room temperature [21]. No difference was observed in the experimental data between the two dosing methods. Exposure to oxygen was achieved by leaking pure O<sub>2</sub> gas into the vacuum chamber. The purity of the dosed gases and vapours were checked with mass spectrometry.

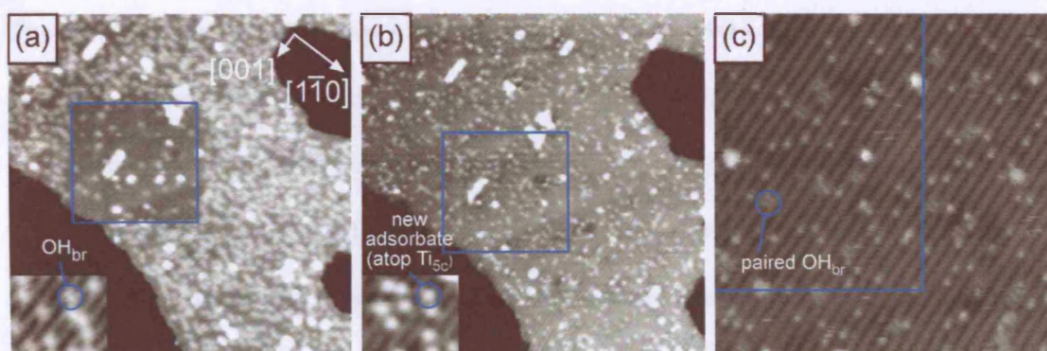


Figure 6.1: STM images (tunnelling voltage: 1.50 V; tunnelling current: 0.50 nA) of  $\text{TiO}_2(110)$ . (a) ( $400 \times 400 \text{ \AA}^2$ , inset  $50 \times 42 \text{ \AA}^2$ ) After dosing 30 L of  $\text{H}_2\text{O}$  which resulted in 11% ML  $\text{OH}_{\text{br}}$  as indicated in the inset. The blue square highlights an area scanned at 3 V to create a  $\text{OH}_{\text{br}}$ -free area. (b) ( $400 \times 400 \text{ \AA}^2$ , inset  $50 \times 42 \text{ \AA}^2$ ) and (c) ( $187 \times 187 \text{ \AA}^2$ ) the same area after exposure to 90 L of  $\text{O}_2$ , containing a new type of adsorbate as indicated in the inset of (b). The blue square marks the previously  $\text{OH}_{\text{br}}$ -free area in (b) and part of the blue square is marked in (c).

## 6.3 Results and discussion

### 6.3.1 Exposure to $>90 \text{ L O}_2$

#### 6.3.1.1 $\text{TiO}_2(110)$ surface with $\text{OH}_{\text{br}}$

The hydroxylated  $\text{TiO}_2(110)$  surface was prepared by exposure of the clean surface to 30 L of  $\text{H}_2\text{O}$  at 300 K. A representative image from the resulting surface is shown in figure 6.1a. The surface contains an  $\text{OH}_{\text{br}}$  coverage of 11% ML together with a low density of short strands of the  $1 \times 2$  reconstruction. These strands of  $1 \times 2$  were used as registration marks in order to relocate specific areas of the surface after dosing with  $\text{O}_2$ . A  $240 \times 240 \text{ \AA}^2$  part of the surface was scanned at 3 V, resulting in dissociation of  $\text{OH}_{\text{br}}$  (removal of H adatoms) within the scanned area [6, 22].

The surface in figure 6.1(a) was subsequently exposed to  $\sim 90$  L of  $O_2$ . The STM images after  $O_2$  exposure (figure 6.1b) reveal a new type of adsorbate atop  $Ti_{5c}$  sites, with a corresponding reduction in the  $OH_{br}$  coverage. We label this new type of adsorbate as type C, as in the previous STM study of Diebold *et al.* [23]. The ratio of the coverage of type C adsorbates after  $O_2$  exposure with respect to the coverage of  $OH_{br}$  before  $O_2$  exposure is about 1:2. This ratio can be used to assign the type C adsorbates. As can be seen from equations 6.2 and 6.4, a ratio of 1:2 is consistent with the type C adsorbates being  $O_{(ad)}$  or  $H_2O_{2(ad)}$ . In contrast, equations 6.5 and 6.6 show that a ratio of 1:1 would be expected if the type C adsorbates were  $HO_{2(ad)}$  and a ratio of 3:2 would be expected if they were  $O_{(ad)}$  formed directly from decomposition of  $HO_{2(ad)}$ .

The image in figure 6.1b, which was recorded after  $O_2$  exposure, shows the same density of type C adsorbates both within the previously  $OH_{br}$ -free area and outside it. Because the type C adsorbates appear with a concomitant decrease in the  $OH_{br}$  density, this indicates that they arise from the reaction of  $O_2$  with the surface  $OH_{br}$ . Since  $O_2$  does not react with the perfect surface [10, 24], the observation of the same density of type C adsorbates inside and outside the previously  $OH_{br}$ -free area means that the reactants, intermediates or the type C adsorbates must be highly mobile. For instance, molecularly adsorbed  $O_2$  may mediate  $OH_{br}$  diffusion in a similar fashion to  $H_2O$  [7, 9].

The high resolution image in figure 6.1c also shows that about  $\sim 90\%$  of the residual  $\sim 2\%$  ML  $OH_{br}$  are paired after exposure to  $O_2$ . As the  $OH_{br}$  are known to repel each other [9], this is a somewhat surprising observation, but preliminary calculations suggest that such paired  $OH_{br}$  can be stabilised by adjacent  $O_{(ad)}$  [25]. Moreover, the associated



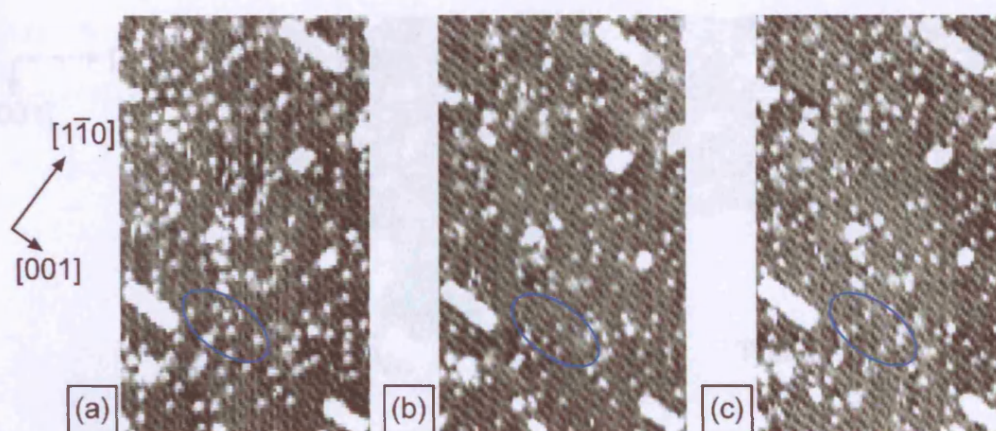


Figure 6.2: (a)-(c) Sequential STM images ( $120 \times 200 \text{ \AA}^2$ ; tunnelling voltage: 1.50 V; tunnelling current: 0.20 nA) of the hydroxylated  $\text{TiO}_2(110)$  surface after dosing 90 L of  $\text{O}_2$ . The images were recorded less than 1 min apart. The blue ellipses are drawn over the same area in each image to guide the eye. In each image, the number and the positions of the type C adsorbates clearly change dramatically within these ellipses.

STM simulations show that such stabilising adatoms may not be visible in STM.

The mobility of the type C adsorbates was investigated by recording sequential STM images from the same area of the surface. A series of such images recorded less than 1 min apart are presented in figure 6.2. It can be seen that the type C adsorbates are indeed mobile. This mobility will be discussed later.

### 6.3.1.2 $\text{TiO}_2(110)$ surface with $\text{OH}_{\text{br}}$ and $\text{O}_{\text{vac}}$

In order to determine whether the type C adsorbates are  $\text{O}_{(\text{ad})}$  or  $\text{H}_2\text{O}_{2(\text{ad})}$ , a  $\text{TiO}_2(110)$  surface was prepared which contains both  $\text{OH}_{\text{br}}$  and  $\text{O}_{\text{vac}}$ . As the product of the reaction of  $\text{O}_2$  with  $\text{O}_{\text{vac}}$  is well-established to be  $\text{O}_{(\text{ad})}$  [6, 10, 14, 15], exposure of this surface to  $\text{O}_2$  allows the appearance of the type C adsorbates to be directly compared with  $\text{O}_{(\text{ad})}$  within the same STM image. Since the apparent height of an adsorbate in STM images can vary

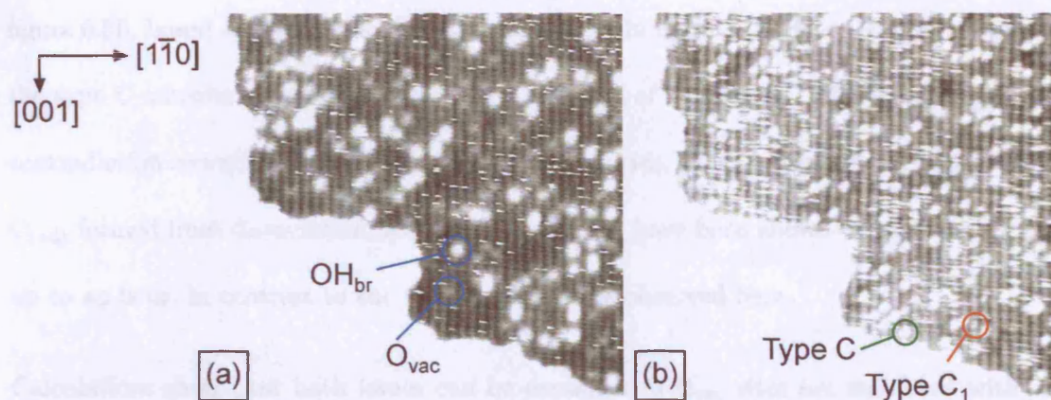


Figure 6.3: STM topography images ( $260 \times 246 \text{ \AA}^2$ ; tunnelling voltage: 1.50 V; tunnelling current: 0.20 nA) of (a) a  $\text{TiO}_2(110)$  surface containing  $\text{O}_{\text{vac}}$  and  $\text{OH}_{\text{br}}$  which formed from dissociation of  $\text{H}_2\text{O}$  from the UHV residual gases and (b) the same area after exposure to 90 L of  $\text{O}_2$ , containing mainly type C adsorbates as indicated.

by at least  $\sim 0.5 \text{ \AA}$ , depending on STM tip conditions, identification of adsorbates is most reliable in the same image or series of images.

In this experiment, the freshly prepared  $\text{TiO}_2(110)$  surface was left for 30 min in UHV to allow time for  $\text{H}_2\text{O}$  dissociation at  $\text{O}_{\text{vac}}$  to occur (figure 6.3a). This surface contained about 5% ML  $\text{OH}_{\text{br}}$  and 2.7% ML  $\text{O}_{\text{vac}}$ . Subsequently, the surface was dosed with  $\sim 90$  L of  $\text{O}_2$ . Figure 6.3b shows an STM image of the same area as in figure 6.3a after exposure to  $\text{O}_2$ . Figure 6.3b reveals type C adsorbates with a coverage of  $\sim 6.8\%$  ML,  $\leq 0.5\%$  ML residual  $\text{OH}_{\text{br}}$  and a small coverage ( $\leq 0.5\%$  ML) of a different adsorbate ( $\text{C}_1$ ) atop  $\text{Ti}_{5c}$  with a lower apparent height than the type C adsorbates. Type C adsorbates dominate the surface, supporting the assignment of type C adsorbates to  $\text{O}_{(\text{ad})}$ .

The assignment of type C adsorbates to  $\text{O}_{(\text{ad})}$  carries two apparent contradictions, which are detailed below. For each  $\text{O}_{\text{vac}}$  filled, one  $\text{O}_{(\text{ad})}$  is expected and for each pair of reacting  $\text{OH}_{(\text{br})}$  species, another  $\text{O}_{(\text{ad})}$  is expected. Therefore the number of  $\text{O}_{(\text{ad})}$  expected in

figure 6.3b, based on the density of  $O_{\text{vac}}$  and  $\text{OH}_{(\text{br})}$  in figure 6.3a, is  $\sim 4.7\%$  ML, whereas the type C adsorbates in figure 6.3b have a coverage of  $\sim 6.8\%$  ML. The second apparent contradiction concerns the mobility of the type C species, which is highlighted in figure 6.2.  $O_{(\text{ad})}$  formed from dissociation of  $\text{O}_2$  in  $O_{(\text{vac})}$  [6, 22] have been shown to be immobile for up to an hour, in contrast to the type C adsorbates observed here.

Calculations show that both issues can be explained if  $O_{\text{vac}}$  sites are stabilised with an additional charge of two electrons each [25]. Such a stabilisation mechanism for  $O_{\text{vac}}$  has recently been reported for other high dielectric constant metal oxides such as  $\text{HfO}_2$  [26]. Assuming that the extra electrons are taken from interstitial Ti species, such charge redistribution would also lower the global surface free energy both at the  $O_{\text{vac}}$  site and at Ti interstitial sites [25]. This is in line with the results of a recent computational study where the stability of Ti interstitials is found to be higher for those with a larger positive charge [27].

According to the theoretical calculations, in the presence of two extra electrons the  $O_{\text{ad}}$  arising from dissociation of  $\text{O}_2$  at  $O_{\text{vac}}$  scavenges the excess electronic charge forming  $O_{(\text{ad})}^{2-}$  [25]. This species is found to be strongly bound to the underlying  $\text{Ti}_{5c}$ , and is therefore immobile [25], which is in line with the experimental observation [6, 22]. These  $O_{(\text{ad})}^{2-}$  species are themselves active sites for the dissociation of  $\text{O}_2$ . This latter  $\text{O}_2$  dissociation pathway leads to two  $O_{(\text{ad})}^-$  and an  $O_{(\text{ad})}^0$  atom for each reacting  $\text{O}_2$  molecule [25], which accounts for the appearance of more than a single  $O_{(\text{ad})}$  per  $O_{\text{vac}}$  or per  $2\text{OH}_{\text{br}}$  in figure 6.3.

Preliminary STM simulations [25] of  $O_{(\text{ad})}^0$ ,  $O_{(\text{ad})}^-$ ,  $O_{(\text{ad})}^{2-}$  suggest that  $O_{(\text{ad})}^0$  and  $O_{(\text{ad})}^-$  are almost indistinguishable and consistent with type C adsorbates, whereas the apparent



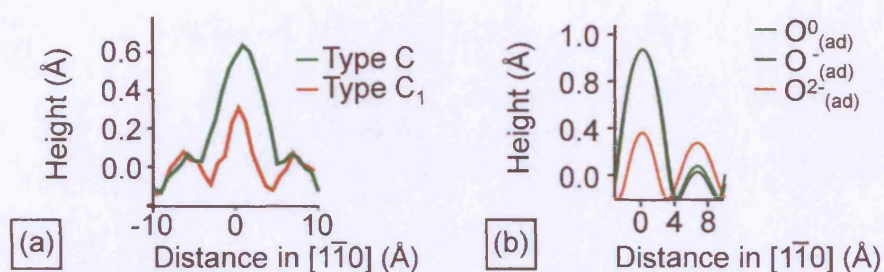


Figure 6.4: (a) The apparent heights of type C and type C<sub>1</sub> adsorbates indicated in figure 6.3. (b) Simulated scanlines for O<sub>(ad)</sub><sup>0</sup>, O<sub>(ad)</sub><sup>-</sup> and O<sub>(ad)</sub><sup>2-</sup> [25].

height of O<sub>(ad)</sub><sup>2-</sup> is much lower (figure 6.4). As for the mobility of O<sub>(ad)</sub><sup>2-</sup>, O<sub>(ad)</sub><sup>-</sup> and O<sub>(ad)</sub><sup>0</sup>, the calculated diffusion barrier for O<sub>(ad)</sub><sup>2-</sup> is 0.89 eV and 1.25 eV higher than that found for O<sub>(ad)</sub><sup>-</sup> and O<sub>(ad)</sub><sup>0</sup>, respectively. This would explain the much higher mobility of type C adsorbates observed in the current experiments compared to the final O adatoms which result from O<sub>2</sub> dissociation at O<sub>vac</sub> sites. Therefore the type C adsorbates in figure 6.3b can now be assigned to O<sub>(ad)</sub><sup>0</sup> and/or O<sub>(ad)</sub><sup>-</sup> species and the type C<sub>1</sub> adsorbates to O<sub>(ad)</sub><sup>2-</sup> species [25].

### 6.3.2 Exposure to 0–2 L O<sub>2</sub>

In order to investigate the intermediate stages of this reaction, a hydroxylated TiO<sub>2</sub> surface was exposed to incremental doses of O<sub>2</sub> from 0 to 2 L. The TiO<sub>2</sub> surface was initially exposed to 30 L of H<sub>2</sub>O (figure 6.5a) then dosed with up to a total 2 L of O<sub>2</sub>.

Figure 6.5b shows an image of the same area as in figure 6.5a after exposure to 0.5 L O<sub>2</sub>. Here, three different types of adsorbates can be distinguished atop Ti<sub>5c</sub> sites. Some representative examples are circled. The line profile of the most common adsorbate matches line profiles taken from type C adsorbates assigned to either O<sub>(ad)</sub><sup>0</sup> and/or O<sub>(ad)</sub><sup>-</sup>, above.



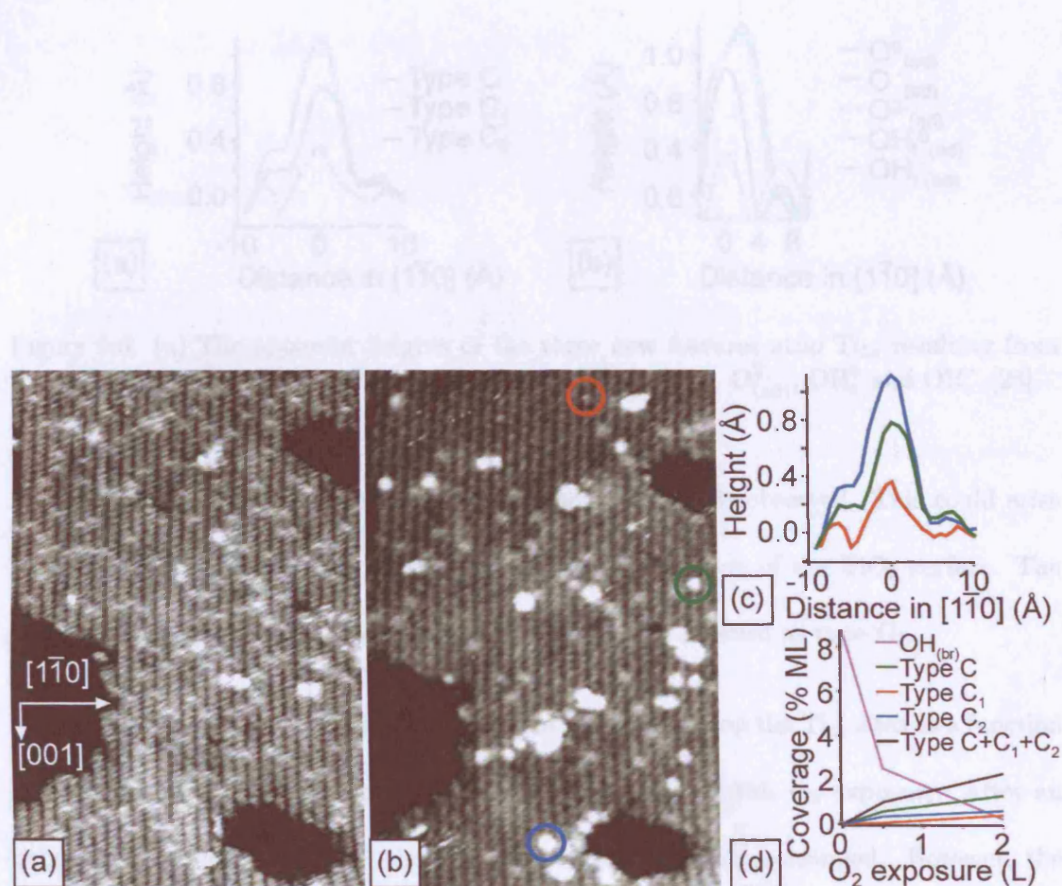


Figure 6.5: STM images ( $176 \times 260 \text{ \AA}^2$ ; tunnelling voltage: 1.50 V; tunnelling current: 0.34–0.19 nA) of (a) a  $\text{TiO}_2(110)$  surface after dosing 30 L of  $\text{H}_2\text{O}$  and therefore containing  $\text{OH}_{\text{br}}$  and (b) the same area as (a) after exposure to 0.5 L of  $\text{O}_2$ . This surface contains adsorbates atop  $\text{Ti}_{5c}$  with three different apparent heights, as indicated by circles. (c) The apparent heights of the three new features atop  $\text{Ti}_{5c}$  resulting from the exposure to  $\text{O}_2$ , as indicated in (b). (d) The coverage of these features as a function of  $\text{O}_2$  exposure. The lines corresponding to the different types of adsorbates have the same colour coding in (b)–(d).

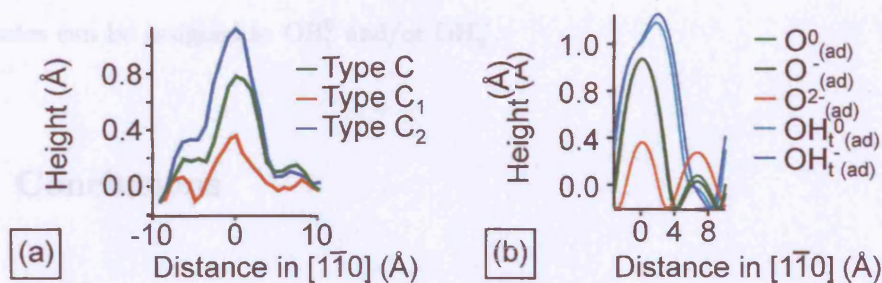


Figure 6.6: (a) The apparent heights of the three new features atop  $\text{Ti}_{5c}$  resulting from the exposure to  $\text{O}_2$ . (b) Simulated scanlines for  $\text{O}_{(\text{ad})}^0$ ,  $\text{O}_{(\text{ad})}^-$ ,  $\text{O}_{(\text{ad})}^{2-}$ ,  $\text{OH}_t^0$  and  $\text{OH}_t^-$  [25].

A small coverage of type  $\text{C}_1$  adsorbates, assigned to  $\text{O}_{(\text{ad})}^{2-}$ , is observed. This could arise from a few residual  $\text{O}_{\text{vac}}$  sites existing after the hydroxylation of the  $\text{TiO}_2$  surface. The additional adsorbates which have higher corrugation are labelled as type  $\text{C}_2$ .

Figure 6.5d shows the coverages of the different adsorbates atop the  $\text{Ti}_{5c}$  sites as a function of  $\text{O}_2$  exposure. The  $\text{OH}_{\text{br}}$  coverage is also plotted against this  $\text{O}_2$  exposure. After an exposure to about 2 L of  $\text{O}_2$ , the  $\text{OH}_{\text{br}}$  are almost entirely consumed. However, the total number of new adsorbates atop  $\text{Ti}_{5c}$  is less than half of the consumed  $\text{OH}_{\text{br}}$ . This discrepancy could arise from clustering of the new adsorbates at the step edges and/or on terraces.

The assignment of type  $\text{C}_2$  adsorbates could be attributed to either clustering of individual adsorbates or to  $\text{H}_2\text{O}_2/\text{HO}_2/\text{OH}_t$ , all of which were proposed as intermediates in previous work [2, 17]. However, by taking into account the vibrational energies and entropies of  $\text{H}_2\text{O}_2$  and  $\text{HO}_2$ , together with their affinity to electron scavenging,  $\text{H}_2\text{O}_2$  and  $\text{HO}_2$  are found to be less stable than either  $\text{OH}_t$  or  $\text{O}_{(\text{ad})}$  [25], which is consistent with the original model proposed by Henderson *et al.* [2]. Hence, by considering the simulated heights of only the most stable species,  $\text{OH}_t$  and the various  $\text{O}_{(\text{ad})}$  species (figure 6.6), type  $\text{C}_2$

adsorbates can be assigned to  $\text{OH}_t^0$  and/or  $\text{OH}_t^-$ .

## 6.4 Conclusions

The reaction of surface  $\text{OH}_{\text{br}}$  on  $\text{TiO}_2$  with  $\text{O}_2$  was investigated using STM coupled with *ab initio* calculations [25]. For higher  $\text{O}_2$  exposures (90 L), this leads to the removal of  $\text{OH}_{\text{br}}$  and the formation of  $\text{O}_{(\text{ad})}^-$  and  $\text{O}_{(\text{ad})}^0$ , consistent with the mechanism proposed by Henderson *et al.* [2]. For low  $\text{O}_2$  exposures (2 L),  $\text{OH}_{\text{br}}$  is still consumed but a range of new adsorbates are found, which are assigned to  $\text{OH}_t$ ,  $\text{O}_{(\text{ad})}^0$  and/or  $\text{O}_{(\text{ad})}^-$  and  $\text{O}_{(\text{ad})}^{2-}$ .

# References

- [1] A. Fujishima and K. Honda, *Nature* **238**, 37 (1972).
- [2] M. A. Henderson, W. S. Epling, C. H. F. Peden, and C. L. Perkins *J. Phys. Chem. B* **107**, 534 (2003).
- [3] L. M. Liu, B. McAllister, H. Q. Ye, and P. Hu *J. Am. Chem. Soc.* **128** 4017 (2006).
- [4] R. Nakamura, A. Imanishi, K. Murakoshi, and Y. Nakato *J. Am. Chem. Soc.* **125**, 7443 (2003).
- [5] G. Mattioli, F. Filippone, and A. Amore Bonapasta, *J. Am. Chem. Soc.* **128**, 13772 (2006).
- [6] O. Bikondoa, C. L. Pang, R. Ithnin, C. A. Muryn, H. Onishi, and G. Thornton, *Nat. Mater.* **5**, 189 (2006).
- [7] S. Wendt, J. Matthiesen, R. Schaub, E. K. Vestergaard, E. Lægsgaard, F. Besenbacher, and B. Hammer *Phys. Rev. Lett.* **96**, (2006) 066107.

- [8] S. Wendt, R. Schaub, J. Matthiesen, E. K. Vestergaard, E. Wahlström, M. D. Rasmussen, P. Thosttrup, L. M. Molina, E. Lægsgaard, I. Stensgaard, B. Hammer, and F. Besenbacher *Surf. Sci.* **598**, (2005) 226.
- [9] Z. Zhang, O. Bondarchuk, B. D. Kay, J. M. White, and Z. Dohnalek, *J. Phys. Chem. B* **110**, 21840 (2006).
- [10] W. S. Epling, C. H. F. Peden, M. A. Henderson, and U. Diebold, *Surf. Sci.* **412**, 333 (1998).
- [11] C. L. Perkins and M. A. Henderson, *J. Phys. Chem. B* **105**, 3856 (2001).
- [12] M.P. de Lara-Castells and Jeffrey L. Krause, *Chem. Phys. Lett.* **354**, 483 (2002).
- [13] M.P. de Lara-Castells and Jeffrey L. Krause, *J. Chem. Phys.* **115**, 4798 (2001).
- [14] M. D. Rasmussen, L. M. Molina, and B. Hammer, *J. Chem. Phys.* **120**, 988 (2004).
- [15] X. Wu, A. Selloni, M. Lazzeri, and S. K. Nayak, *Phys. Rev. B* **68**, 241402 (2003).
- [16] M. Anpo, N. Aikawa, Y. Kubokawa, M. Che, C. Louis, and E. Giamello, *J. Chem. Phys.* **89**, 5689 (1985).
- [17] A. Tilocca, C. Di Valentin, and A. Selloni, *J. Phys. Chem. B* **109**, 20963 (2005).
- [18] C. Di Valentin, G. Pacchioni, and A. Selloni, *Phys. Rev. Lett.* **97**, 166803 (2006).
- [19] J.P. Perdew, K. Burke, and M. Ernzerhof, *Phys. Rev. Lett.* **77** 3865 (1996).
- [20] A. G. Thomas, W. R. Flavell, A. K. Mallick, A. R. Kumarasinghe, D. Tsoutsou, N. Khan, C. Chatwin, S. Rayner, and G. C. Smith, *Phys. Rev. B* **75**, 35105 (2007).

- [21] C.L. Pang, A. Sasahara, H. Onishi, Q. Chen, and G. Thornton, *Phys. Rev. B* **74**, 73411 (2006).
- [22] C. L. Pang, O. Bikondoa, D. S. Humphrey, A. C. Papageorgiou, G. Cabailh, R. Ithnin, Q. Chen, C. A. Muryn, H. Onishi, G. Thornton, *Nanotechnology* **17**, 5397 (2006).
- [23] U. Diebold, J. Lehman, T. Mahmoud, M. Kuhn, G. Leonardelli, W. Hebenstreit, M. Schmid, and P. Varga, *Surf. Sci.* **411**, 137 (1998).
- [24] M. Batzill and U. Diebold, *Phys. Chem. Chem. Phys.* **9**, 2307 (2007).
- [25] N. Beglitis, G. Teobaldi, W. A. Hofer, and A. J. Fisher (personal communication)
- [26] D. Muñoz Ramo, J. L. Gavartin, A. L. Shluger, and G. Bersuker, *Phys. Rev. B* **75**, 205336 (2007).
- [27] H. Iddir, S. Ögüt, P. Zapol, and N. D. Browning, *Phys. Rev. B* **75**, 73203 (2007).



## Chapter 7

# Atomically resolved scanning tunnelling spectroscopy of $\text{TiO}_2(110)$

In this chapter, scanning tunnelling spectroscopy (STS) is used to measure the local density of states (LDOS) of rutile  $\text{TiO}_2(110)$  with atomic resolution. From this, it is determined that titanium five-fold coordinated ( $\text{Ti}_{5c}$ ) atoms provide a higher tunnelling current than bridging oxygen ( $\text{O}_{br}$ ) atoms at both positive and negative bias. The data evidences three surface states, which are present for all tunnelling sites and located within the band gap of the reduced crystal. These states appear at sample biases of  $-0.7$  eV,  $0.2$  eV and  $1.0$  eV. Another filled state appears only at some  $\text{Ti}_{5c}$  sites that are second-to-third nearest  $\text{Ti}_{5c}$  neighbours of oxygen vacancies ( $\text{O}_{vac}$ ).

## 7.1 Introduction

Considerable research effort has been invested recently in order to provide chemical information alongside the spatial resolution of STM [1–3]. The work described in this chapter employs atomically resolved scanning tunnelling spectra in order to correlate the electronic structure of  $\text{TiO}_2(110)$  with specific atomic sites (such as  $\text{Ti}_{5c}$  atoms,  $\text{O}_{br}$  atoms,  $\text{O}_{vac}$  and  $\text{OH}_{br}$ ).

The electronic structure of titanium dioxide surfaces has been the subject of intense study. Of these  $\text{TiO}_2$  surfaces, the most extensively characterised is rutile (110). However, despite a number of theoretical and experimental investigations, no consensus has been reached regarding the relationship between electronic surface states and specific surface sites.

Photoelectron spectroscopy data give evidence of a “defect state” for  $\text{TiO}_2(110)$  between the valence band and the Fermi level [4–6]. Hebenstreit *et al.* [4] detect this state with UV photoelectron spectroscopy (UPS) at a binding energy of about 1.0 eV. This state has been attributed to surface oxygen vacancies that form after annealing the surface in UHV and disappears after exposure of the surface to oxygen at room temperature [4]. More recently, Thomas *et al.* [5] have recorded resonant photoemission spectra of this state, placing it at a binding energy of 0.9 eV. The defect state exhibits resonances at photon energies of 46 and 53 eV which were assigned to  $\text{Ti } 3p \rightarrow \text{Ti } 3d/\text{O } 2p$  and  $\text{Ti } 3p \rightarrow \text{Ti } 4sp/\text{O } 2p$  interatomic resonance processes, respectively. Henderson [6] detects the same state with electron energy loss spectroscopy (EELS) at 0.75 eV, assigning it to the  $\text{Ti}^{3+}$  sites adjacent to or in oxygen vacancies.



Given that most experimental studies of the electronic structure cannot be correlated with specific sites, comparison of the spatially resolved STS with theoretical data becomes crucial. A recent review [7] summarises the advances in the theoretical description of oxygen vacancies in  $\text{TiO}_2$ . For the current work, the most relevant calculations are summarised below. Work from Di Valentin *et al.* [8] employ *ab initio* calculations with hybrid exchange and correlation (xc) energy functionals as described in section 6.1. Electronic states in the band gap associated with surface oxygen vacancies and hydroxyl groups ( $\text{OH}_{\text{br}}$ ) were found. Interestingly, they show that the electronic structure does not change significantly between a surface containing an oxygen vacancy and one containing two bridging hydroxyls. An electron corresponding to an occupied Ti 3d state is localised on a titanium atom under the vacancy or hydroxyl pair in a  $d_{xz}$  state, 1–1.6 eV below the conduction band minimum (CBM), and another electron associated with the same 3d state is located at the first nearest  $\text{Ti}_{5c}$  neighbour in a  $d_{xy}$  state, 1.2 eV below the CBM. The graphs in figure 7.1 show the calculated density of states for a surface containing two adjacent  $\text{OH}_{\text{br}}$  (top) and a surface containing an  $\text{O}_{\text{vac}}$  (bottom).

“Defect states” of the oxygen deficient rutile  $\text{TiO}_2$  do not appear in the band gap when “pure” DFT calculations are employed. Instead, they are detected within the valence band. However, by using the local spin density approximation with on-site Coulomb repulsion  $U$ , LSDA+ $U$ , Anisimov *et al.* [9] show the presence of band gap states due to an oxygen vacancy. Therefore, both hybrid xc energy functionals and LSDA+ $U$  may be able to provide accurate descriptions of  $\text{TiO}_2$ .

Atomically resolved STS measurements have been made previously on  $\text{TiO}_2(110)$  [10].

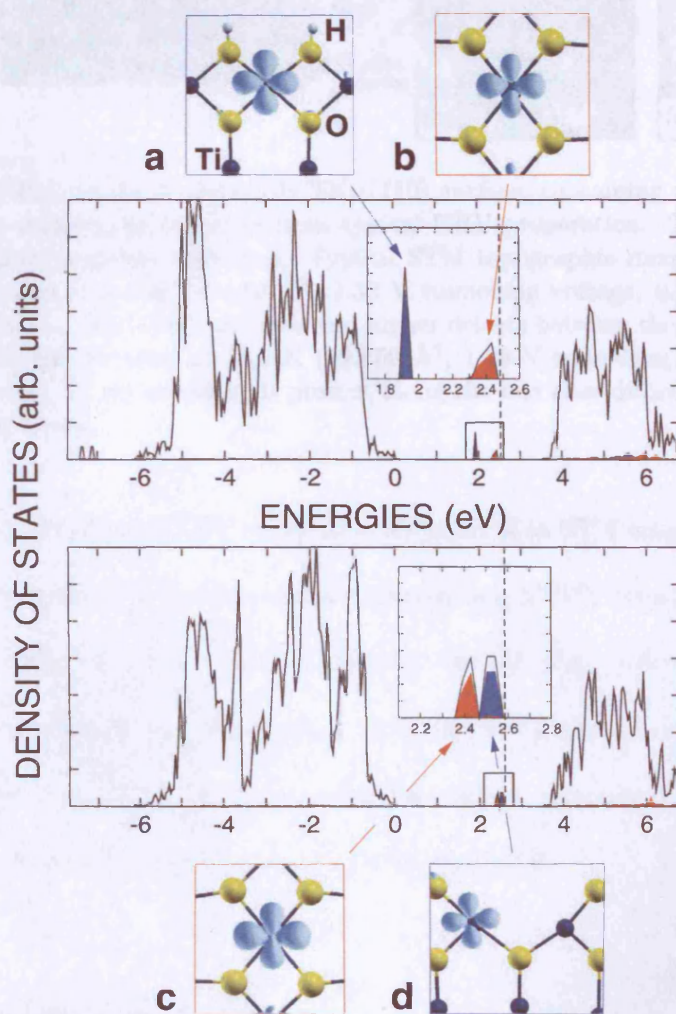


Figure 7.1: Calculated density of states for the surface containing two adjacent  $\text{OH}_{\text{br}}$  (top spectrum) and the surface containing an  $\text{O}_{\text{vac}}$  (bottom spectrum). The states localised in the titanium atom under the vacancy (d) and hydroxyl pair (a) are highlighted in blue, whereas the states localised in a  $\text{Ti}_{5\text{c}}$  titanium, first nearest  $\text{Ti}_{5\text{c}}$  neighbour to the vacancy (c) and hydroxyl pair (b), are highlighted in red. (Figure reproduced from Di Valentin *et al.* [8])

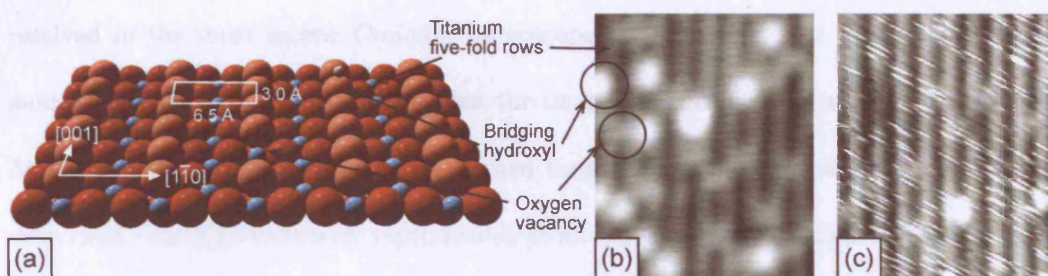


Figure 7.2: (a) Ball model of the rutile  $\text{TiO}_2(110)$  surface, containing a hydroxyl group and an oxygen vacancy, as expected from typical UHV preparation. The unit cell and the high symmetry axes are displayed. Typical STM topographic images of  $\text{TiO}_2(110)$ . (b) Image recorded at 4.5 K ( $72 \times 59 \text{ \AA}^2$ ; 2.30 V tunnelling voltage; 0.05 nA tunnelling current) showing  $\text{O}_{\text{vac}}$  and  $\text{OH}_{\text{br}}$  as lower and higher defects between the bright  $\text{Ti}_{5c}$  rows, respectively. (c) Image taken at 78.0 K ( $72 \times 59 \text{ \AA}^2$ ; 1.26 V tunnelling voltage; 0.02 nA tunnelling current). In (c) streaking is present along the fast scan direction over the  $\text{Ti}_{5c}$  rows after a few hours.

This is achieved by taking STS I-V curves at every point of an STM image. The technique has been named current imaging tunnelling spectroscopy (CITS) because, current maps are effectively produced at a number of voltages. Batzill *et al.* [10] report CITS data obtained at room temperature. The present work provides better spectral signal-to-noise ratios, higher bias resolution, and higher spatial resolution. Crucially,  $\text{O}_{\text{vac}}$  and  $\text{OH}_{\text{br}}$  are distinguished, as are individual  $\text{Ti}_{5c}$  and  $\text{O}_{\text{br}}$  sites (figure 7.2).

## 7.2 Experimental section

STS experiments used both the *Omicron* VT-STM and LT-STM instruments described in section 3.1. The VT was used at room temperature and the LT for measurements at  $78 \pm 2 \text{ K}$  and  $4.5 \pm 0.5 \text{ K}$ . The STS spectra consist of tunnelling current versus sample bias (I/V) curves. A leakage current was present in the STM tip-sample junction, which is a known issue for *Omicron* STM equipment (although this technical fault has been

resolved in the most recent *Omicron* microscopes). To account for this, a constant is numerically added to the spectra, so that the tunnelling current is set to zero at zero bias. At  $4.5 \pm 0.5$  K, both electrochemically etched tungsten and mechanically cut iridium tips were used. The STS data were reproducible at all temperatures and with all working tips. However, the resolution obtained for a particular set of experimental data which employed a W tip at liquid helium temperature is of much higher quality with respect to spatial resolution, signal-to-noise ratio and thermal drift. Therefore, these data form the main focus of this chapter.

Point scanning tunnelling spectra were used to determine the band gap of  $\text{TiO}_2(110) 1 \times 1$ . Regardless of surface site, sample temperature and tip material, the band gap was found to be between sample bias voltages of +0.70 and  $-2.3$  V (with an error of  $\pm 0.30$  V). As such, a positive sample bias of 0.7 V is treated as the CBM in all data.

The base pressure of the LT-STM chamber was  $1 \times 10^{-11}$  mbar. A  $\text{TiO}_2(110)$  surface was prepared in the attached preparation chamber with several cycles of  $\text{Ar}^+$  sputtering and annealing in UHV to 1100 K, as read by a pyrometer with the emissivity set to 0.5. The crystal was dark blue. After the final anneal, the sample was transferred to the STM chamber and allowed to cool down for about 30 minutes before transferring to the liquid He cooled stage.

Previous studies of this surface [11, 12], show that some water dissociation (from the residual vacuum) should occur in the  $\text{O}_{\text{vac}}$  during this cool-down time. Once the sample is in the STM stage, the low temperature restricts any further water dissociation. Instead, molecular adsorption occurs at titanium five-fold atoms. Such adsorbed molecules are



immobile at these temperatures. When the LT-STM was operated at liquid nitrogen temperatures, a persistent streaking was evident along the fast scan direction over the Ti5c rows after a few hours (see right image on figure 7.2), suggestive of some mobile species on the surface. This is reflected in an instability of the corresponding STS data.

One of the main technical difficulties of recording STS spectra at every STM pixel is the long data acquisition times. Similar measurements, reported recently by Jihno-Lee *et al.* [13] required approximately two days. Given that the  $\text{TiO}_2(110)$  surface interacts with the residual gases in the vacuum over such timescales and that thermal drifting is highly undesirable, the data acquisition time was minimised in the current work. This was achieved by reducing the number of points (and hence the resolution) of each individual spectrum together with a reduction in the number of pixels in each image to  $100 \times 100$  from the more typical  $400 \times 400$  pixels. Furthermore, collection of the data via a lock-in amplifier was avoided because the data acquisition time would have to be drastically extended in order to allow the amplifier to respond.

### 7.3 Results and discussion

A large scale image of the surface recorded shortly before the collection of CITS data is shown in figure 7.3a. The surface contains approximately 5% ML bridging oxygen vacancies ( $\text{O}_{\text{vac}}$ ), 4% bridging hydroxyls ( $\text{OH}_{\text{br}}$ ) and less than 1% molecular water, together with a low density of the  $1 \times 2$  reconstruction [14].

Figure 7.3b depicts the topographic image of the surface recorded simultaneously with

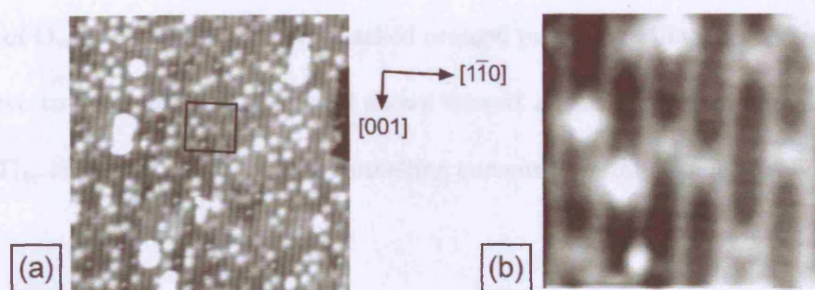


Figure 7.3: (a) STM image recorded at 4.5 K ( $250 \times 250 \text{ \AA}^2$ ; 2.30 V tunnelling voltage; 0.05 nA tunnelling current) showing an overview of the surface topography before the collection of STS. A black square indicates the area from which the image is taken in (b). The vectors indicate the high symmetry axes. (b) Smoothed topographic STM image taken at 4.5 K ( $45 \times 45 \text{ \AA}^2$ ; 2.00 V tunnelling voltage; 0.03 nA tunnelling current) recorded simultaneously with the STS data.

the CITS data. The  $\text{Ti}_{5c}$  sites are atomically resolved. An atomic-scale corrugation can also be faintly detected along the bridging oxygen ( $\text{O}_{br}$ ) rows in the [001] direction. The peaks in corrugation of the  $\text{O}_{br}$  rows are in-phase with the peaks in  $\text{Ti}_{5c}$  rows along  $[1\bar{1}0]$ . This means that the positions of the peaks in the  $\text{O}_{br}$  rows must correspond to  $\text{O}_{br}$  atoms, given that the bright spots in the Ti rows correspond to individual  $\text{Ti}_{5c}$  atoms. Hence, for the first time, it can be deduced that  $\text{O}_{br}$  can be “visible” in STM images at the same time that  $\text{Ti}_{5c}$  are imaged. After the acquisition of each pixel in the topographic image shown in figure 7.3b, the tip was immobilised with tunnelling conditions of +2.00 V and 0.03 nA. The feedback loop was then switched off and the sample bias was ramped between +2.00 and -2.00 V through 40 regularly spaced values, whilst the tunnelling current was recorded. This results in a resolution of 0.10 V in the corresponding spectra. The delay (before acquisition) and acquisition time for each individual spectrum was set at 320  $\mu\text{s}$ .

The current maps at each bias voltage are displayed in figure 7.4. A light blue grid is superimposed on some of the current maps indicating the position of  $\text{Ti}_{5c}$  rows. The

positions of  $O_{\text{vac}}$ ,  $\text{OH}_{\text{br}}$  and  $\text{H}_2\text{O}$  are marked orange, purple and blue, respectively. These marks serve to guide the eye. The grid shows that at all biases probed outside the band gap, the  $\text{Ti}_{5\text{c}}$  atoms provide a greater tunnelling current than the geometrically higher  $O_{\text{br}}$  atoms.

The current maps in figure 7.4 reveal a number of bright protrusions along  $\text{Ti}_{5\text{c}}$  [001] rows at negative sample bias, indicated with green circles. The positions of these bright spots do not correspond directly with  $O_{\text{vac}}$  or  $\text{OH}_{\text{br}}$  nearest neighbour  $\text{Ti}_{5\text{c}}$  sites. Instead, a correlation analysis, shown in figure 7.5, indicates that these bright spots usually appear at the second-to-third nearest  $\text{Ti}_{5\text{c}}$  sites.

The sample conductivity ( $dI/dV$ ) can be used to determine the band gap of semiconductors and give an overall idea of the LDOS [18]. Therefore, in order to gain insight into the surface electronic structure, numerically differentiated ( $dI/dV$ ) spectra are plotted against the sample bias in figure 7.6a. The spectra are averaged over areas which correspond to  $O_{\text{vac}}$ ,  $\text{OH}_{\text{br}}$ ,  $O_{\text{br}}$  and  $\text{Ti}_{5\text{c}}$  sites, as shown in the inset of figure 7.6a.  $\text{Ti}_{5\text{c}}(1)$  denotes the special  $\text{Ti}_{5\text{c}}$  sites with increased conductivity at negative sample bias (marked with green circles in figure 7.4), whilst  $\text{Ti}_{5\text{c}}(2)$  is used to describe the regular  $\text{Ti}_{5\text{c}}$  sites. The overall shape of these  $dI/dV$  curves compare well with those reported by Batzill *et al.* [10] for areas of  $1 \times 1 \text{ TiO}_2(110)$  at room temperature. A peak at a sample bias of  $+1.00 \pm 0.20 \text{ V}$  and the asymmetry between the empty and filled states are reproduced in both data sets. However, peaks present at  $+0.2 \text{ V}$ ,  $-0.7 \text{ V}$ , and  $-1.9 \text{ eV}$  identified in the curves of figure 7.6 are not resolved in the data of Batzill *et al.* [10], due to the poorer resolution and signal-to-noise ratio of their spectra.



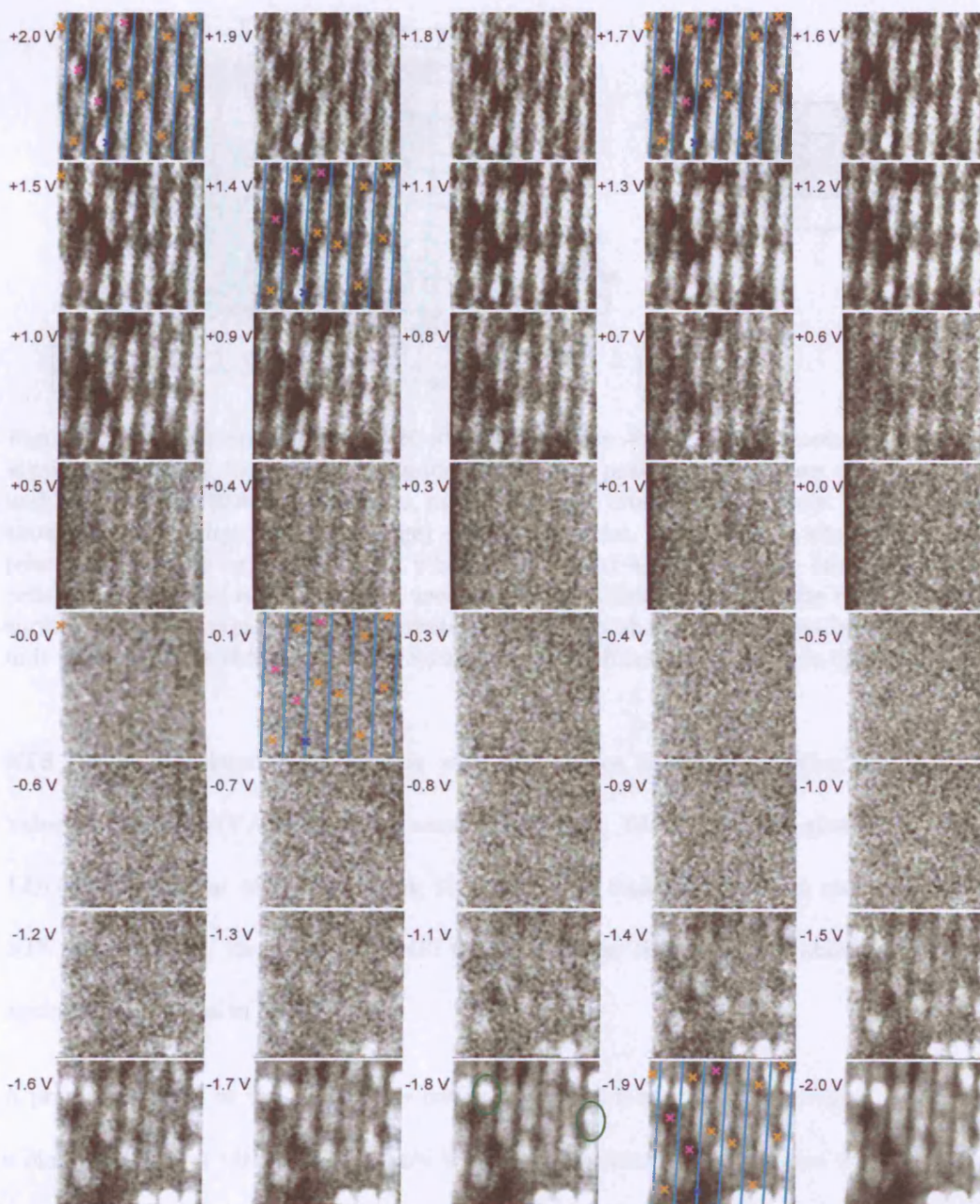


Figure 7.4: Current maps at sample bias ranging from +2.00 to  $-2.00$  V, recorded simultaneously with the topographic image displayed in figure 7.3b. The absolute value of current is plotted in grayscale with higher current corresponding to brighter areas. A light blue grid is superimposed on the current maps corresponding to +2.0, +1.6, +1.4,  $-0.1$  and  $-1.9$  V. The grid indicates  $Ti_{5c}$  rows. The positions of  $O_{vac}$ ,  $OH_{br}$  and  $H_2O$  are highlighted with orange, purple and blue crosses, respectively. Two sites with increased conductivity over  $Ti_{5c}$  atoms,  $Ti_{5c}(1)$ , are circled in green.



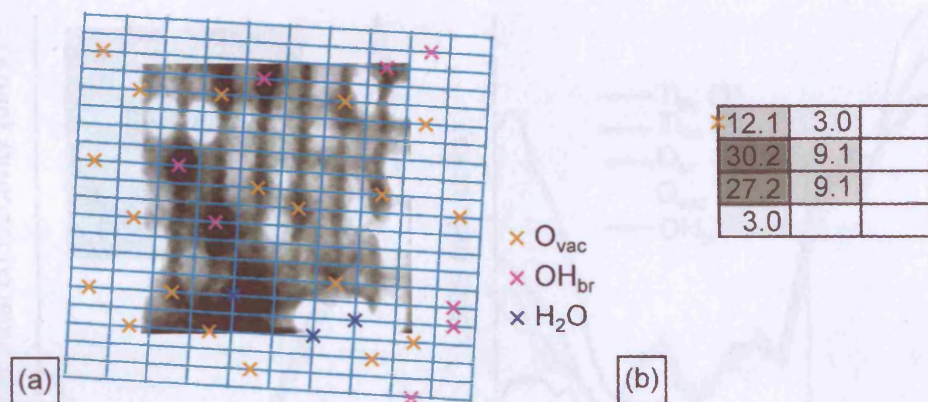


Figure 7.5: (a) Current map at 4.5 K with sample bias  $-2.00$  V. The intersections in the superimposed light blue grid correspond to the  $Ti_{5c}$  positions. Positions of  $O_{vac}$ ,  $OH_{br}$  and  $H_2O$  are highlighted with orange, purple and blue crosses, respectively. (b) The table shows the probability (as a percentage) of finding special, bright  $Ti_{5c}(1)$  sites in positions relative to the oxygen vacancy, which is indicated with an orange cross.  $8 \times 6$  unit cells centred around each  $O_{vac}$  were used to construct this table. Because the  $TiO_2(110)$  surface has 4-fold symmetry, the probabilities are only shown for one quadrant (i.e.  $4 \times 3$  unit cells) which is obtained by averaging the probabilities found for each quadrant.

STS can be correlated more directly with the surface LDOS by plotting the absolute value of  $(dI/dV) \times (V/I)$  versus the sample bias [18].  $(dI/dV) \times (V/I)$  gives the surface LDOS, independent of the set point, i.e. the initial tunnelling current and bias in the STS measurement. As such, the LDOS for the different sites described above are plotted against sample bias in figure 7.6b.

A prominent state at the edge of the conduction band is evident as a shoulder located at a bias voltage of  $+1.0$  V. This feature is also distinguished in the spectra corresponding to the  $1 \times 1$  region of  $TiO_2(110)$  in the work of Batzill *et al.* [10], but not detected in the inverse-photoemission spectrum (IPS) of  $TiO_2(110)$  [19].

Two additional, distinct surface states can be identified within the band gap; at  $-0.70$  and  $+0.20$  V. These states are present at all surface sites and may arise from  $Ti^{3+}$  interstitials,

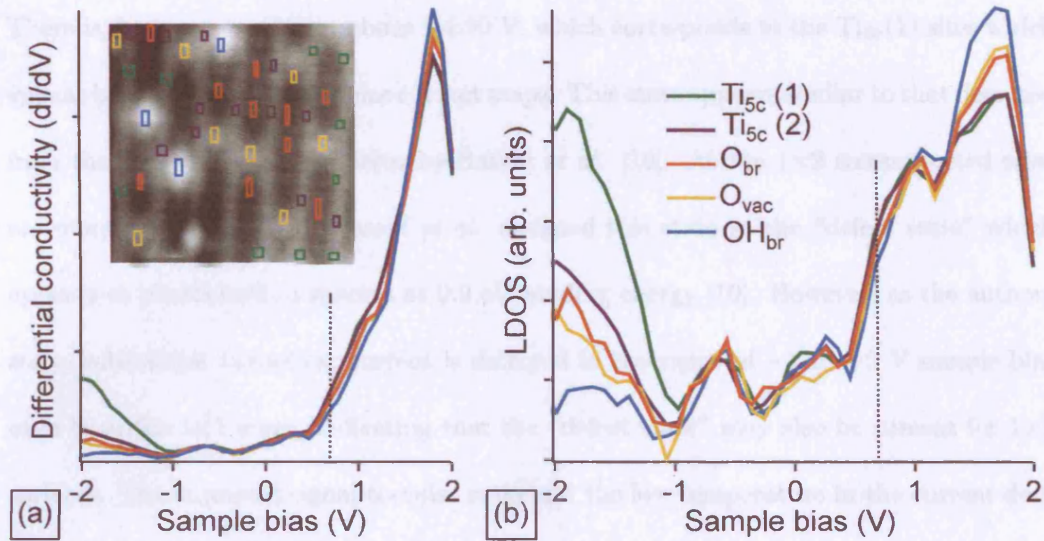


Figure 7.6: (a) The differential conductivities versus the sample bias. Different curves correspond to spectra averaged over O<sub>br</sub>, O<sub>vac</sub>, Ti<sub>5c</sub> and OH<sub>br</sub> sites. The inset shows the corresponding STM topography and indicates the areas from which the averaged spectra are taken. (b) Local density of states corresponding to the same areas as in (a) versus sample bias. Dotted lines mark the position of the conduction band minimum.

### 7.4 Conclusion

which have been deduced as the carriers for the conductivity of TiO<sub>2</sub> [16].

The spectra in figure 7.6 show no new band gap states for either the O<sub>vac</sub> or the OH<sub>br</sub>. This lack of band gap states can also be concluded from the current maps in figure 7.4. The current maps do not reveal any higher tunnelling current at any surface site for any particular bias within the band gap. Moreover, to explicitly test the calculations of Di Valentin *et al.* (discussed in the introduction) [8] electronic states were searched for at the nearest Ti<sub>5c</sub> neighbours to O<sub>vac</sub> and OH<sub>br</sub>. No special features were found either in the current maps or the LDOS curves at these Ti<sub>5c</sub> sites. This could be explained by the orientation of these  $d_{xy}$  states parallel to the surface. Such states might only be detected at very close tip-sample distances.

There is, however, a state at about  $-1.90$  V, which corresponds to the  $\text{Ti}_{5c}(1)$  sites which appear bright in the negative bias current maps. This state appears similar to that detected from the  $1 \times 2$  reconstructed areas by Batzill *et al.* [10]. As the  $1 \times 2$  reconstructed sites are more oxygen deficient, Batzill *et al.* assigned this state to the “defect state” which appears in photoelectron spectra at  $0.9$  eV binding energy [10]. However, as the authors state, substantial tunnelling current is detected in the range of  $-1$  to  $-2$  V sample bias even from the  $1 \times 1$  areas, indicating that the “defect state” may also be present for  $1 \times 1$  surfaces. The improved signal-to-noise ratio and the low temperature in the current data set may allow the current signal which was unresolved in [10] to be resolved into this state at  $-1.90$  V.

## 7.4 Conclusions

To summarise, STS measurements have revealed a rich array of delocalised surface states in the band gap of  $\text{TiO}_2(110)$ . These states are tentatively assigned to conductivity carriers of the single crystal, namely the  $\text{Ti}^{3+}$  interstitials. Furthermore, a defect state appeared over some selected  $\text{Ti}_{5c}$  atoms which is probably caused by the presence of  $\text{O}_{\text{vac}}$  (and  $\text{OH}_{\text{br}}$ ) as they correlate with their second-to-third nearest  $\text{Ti}_{5c}$  neighbours. It is anticipated that this spatially resolved electronic structure of the  $\text{TiO}_2(110)$  band gap will contribute towards the understanding of fundamental questions regarding the nature of the surface electronic structure, conductivity and STM interpretation.

Reproducing the experimental data presented in this chapter represents a significant challenge for *ab initio* calculations. Such calculation are currently in progress jointly in Prof.

Hofer's group in Liverpool and Prof Fisher's group in UCL. The aim is to obtain a full interpretation of the  $\text{TiO}_2(110)$  band gap structure. If agreement with the STS data can be successfully reached, this would represent by far the most accurate theoretical description of  $\text{TiO}_2$  to date. This, in turn, could lead to theoretical simulations anticipating reactions and behaviours yet to be discovered experimentally.

# References

- [1] W. Ho, *J. Chem. Phys.* **117**, 11033 (2002).
- [2] C. Durkan and M. E. Welland, *Appl. Phys. Lett.* **80**, 458 (2002).
- [3] N. Nilius, N. Ernst, and H.-J. Freund, *Surf. Sci.* **478**, L327 (2001).
- [4] E. L. D. Hebenstreit, W. Hebenstreit, H. Geisler, S. N. Thornburg, C. A. Ventrice, Jr., D. A. Hite, P. T. Sprunger, and U. Diebold, *Phys. Rev. B* **64**, 115418 (2001).
- [5] A. G. Thomas, W. R. Flavell, A. K. Mallick, A. R. Kumarasinghe, D. Tsoutsou, N. Khan, C. Chatwin, S. Rayner, and G. C. Smith, *Phys. Rev. B* **75**, 35105 (2007).
- [6] M. A. Henderson, *Surf. Sci.* **400**, 203 (1998).
- [7] M. V. Ganduglia-Pirovano, A. Hofmann, and J. Sauer, *Surf. Sci. Rep.* **62**, 219 (2007).
- [8] C. Di Valentin, G. Pacchioni, and A. Selloni, *Phys. Rev. Lett.* **97**, 166803 (2006).
- [9] V. I. Anisimov, M. A. Korotin, I. A. Nekrasov, A. S. Mylnikova, A. V. Lukoyanov, J. L. Wang, and Z. Zeng, *J. Phys.: Condens. Matter* **18**, 1695 (2006).
- [10] M. Batzill, K. Katsiev, D. J. Gaspar, and U. Diebold, *Phys. Rev. B* **66**, 235401 (2002).



- [11] O. Bikondoa, C. L. Pang, R. Ithnin, C. A. Muryn, H. Onishi, and G. Thornton, *Nat. Mater.* **5**, 189 (2006).
- [12] I. M. Brookes, C. A. Muryn, and G. Thornton, *Phys. Rev. Lett.* **87**, 266103 (2001).
- [13] Jinho Lee, K. Fujita, K. McElroy, J. A. Slezak, M. Wang, Y. Aiura, H. Bando, M. Ishikado, T. Masui, J.-X. Zhu, A. V. Balatsky, H. Eisaki, S. Uchida, and J. C. Davis, *Nature* **442**, 546 (2006).
- [14] U. Diebold, *Surf. Sci. Rep.* **48**, 53 (2003).
- [15] U. Diebold, J. F. Anderson, K.-O. Ng, and D. Vanderbilt, *Phys. Rev. Lett.* **77**, 1322 (1996).
- [16] M. A. Henderson, *Surf. Sci.* **343**, L1156 (1995).
- [17] J. Tersoff and D. R. Hamann, *Phys. Rev. B* **31**, 805 (1985).
- [18] O. Gurlu, H. J. W. Zandvliet, and B. Poelsema, *Phys. Rev. Lett.* **93**, 066101 (2004).
- [19] A. K. See and R. A. Bartynski, *Phys. Rev. B* **30**, 12064 (1984).
- [20] S. Munnix and M. Schmeits, *Phys. Rev. B* **50**, 12064 (1994).

## Chapter 8

# Summary and further work

Synchrotron based photoemission spectroscopy and scanning tunnelling microscopy (STM) have been employed to study titania surfaces and their interaction with small molecules, such as water and oxygen.

The growth of ultrathin films of titania supported on Ni(110) was studied by combining photoemission spectroscopy and STM. The growth conditions for stoichiometric TiO<sub>2</sub> films were explored together with the reactivity of a film with TiO<sub>2</sub>(110) present. The reactivity was found to closely resemble that of the native TiO<sub>2</sub>(110) surface, as was the electronic structure. Under certain conditions, reduced TiO<sub>2</sub>(110) phases could also be formed, namely the 1×2 reconstruction and crystallographic shear planes. Both types of reduced phase can also be formed on the native TiO<sub>2</sub>(110) surface. Particularly as shear planes are bulk defects, it is clear that at least structurally, the reduction behaviour of the ultrathin TiO<sub>2</sub> film closely resembles the native TiO<sub>2</sub>(110) surface. As TiO<sub>2</sub>(110) is the best characterised oxide surface, it is an attractive prospect to have a conducting mimic

## Chapter 8

of the surface so that techniques, such as STM-inelastic electron tunnelling spectroscopy, which require a high substrate conductivity become tractable. The Ni(110)-supported ultrathin TiO<sub>2</sub> is a promising candidate to act as such a mimic. Local density of states measurements, obtained from atomically resolved STS, would represent the most stringent test of the extent to which the electronic structure of the ultrathin TiO<sub>2</sub> resembles the native surface.

A mechanism for electron scavenging via molecular oxygen was unravelled on TiO<sub>2</sub>(110) via STM studies, coupled with theoretical calculations. By exposing oxygen to a number of specially prepared TiO<sub>2</sub>(110) surfaces (such as a hydroxylated TiO<sub>2</sub>(110)), it was deduced that O<sub>2</sub> reacts with surface hydroxyl to form adsorbed O<sub>(ad)</sub> and water vapour. Furthermore, it was shown that the resulting O<sub>(ad)</sub> are highly mobile. However, a number of discrepancies remained. For instance, the O<sub>(ad)</sub> which form from the reaction with surface hydroxyl are mobile, whereas it is known that O<sub>(ad)</sub> resulting from the splitting of O<sub>2</sub> at oxygen vacancies are immobile for at least an hour. This and other apparent inconsistencies were resolved by close collaboration with theoretical modelling groups based in UCL (Beglitis and Fisher) and the University of Liverpool (Teobaldi and Hofer). The key to their calculations was the consideration of oxygen vacancies with excess electrons. This charge is carried through to the surface hydroxyls, following water dissociation in the oxygen vacancies, and the excess electrons are scavenged by oxygen in either case. Crucially, O<sub>(ad)</sub> arising from dissociation in O<sub>vac</sub> carry a double negative charge and are therefore strongly bound to the surface and immobile. In contrast, those resulting from reaction with surface hydroxyl are neutral or have only a single negative charge and are therefore mobile. It would be of great interest to obtain direct experimental evidence



## Chapter 8

for these charged species. This could come from scanning tunnelling spectroscopy (STS) measurements of the  $O_{(ad)}$  and atomic-scale scanning Kelvin probe microscopy images, which can identify charged species.

Finally, atomically resolved STS data were recorded from the  $TiO_2(110)$  surface. Both localised and delocalised surface states were obtained. In particular, a filled state appears at  $-1.9$  V which is found on Ti sites near but not adjacent to oxygen vacancy sites. This contrasts with all published theoretical calculations of the surface density of states. In particular, a recent calculation predicts defect states localised at Ti sites adjacent to  $O_{vac}$ . This was not observed in the spectra. One reason for this discrepancy could be because the  $O_{vac}$  have excess charge, which has only just been posited in Chapter 6 of this thesis. DFT simulations of STM and STS by Beglitis, Teobaldi, Hofer and Fisher are currently in progress in order to test this idea. As for future experimental work, it would be interesting to see if the state at  $-1.9$  V is quenched, after filling  $O_{vac}$  with O, as it is for the state identified (and attributed to  $O_{vac}$ ) with various electron spectroscopies,  $\sim 1.0$  eV below the Fermi level.